HIGHWAY RESEARCH RECORD

Number 323

Landslides

1 Report

Slope Protection and Stability

3 Reports

Embankment Design and Stability

5 Reports

Subject Areas

33 Construction
61 Exploration-Classification (Soils)
62 Foundations (Soils)
63 Mechanics (Earth Mass)

HIGHWAY RESEARCH BOARD
DIVISION OF ENGINEERING NATIONAL RESEARCH COUNCIL
NATIONAL ACADEMY OF SCIENCES—NATIONAL ACADEMY OF ENGINEERING
WASHINGTON, D.C. 1970

Standard Book Number 309-01822-6

Price: $3.20

Available from

Highway Research Board
National Academy of Sciences
2101 Constitution Avenue
Washington, D.C. 20418

Department of Soils, Geology and Foundations

Eldon J. Yoder, Chairman
Purdue University, Lafayette, Indiana

Chester McDowell, Vice Chairman
Texas Highway Department, Austin

J. W. Guinnee
Highway Research Board Staff

DIVISION B

Carl L. Monismith, Chairman
University of California, Berkeley

William P. Hofmann, Vice Chairman
New York Department of Transportation, Albany

COMMITTEE ON EMBANKMENTS AND EARTH SLOPES

(As of December 31, 1969)

William P. Hofmann, Chairman
New York Department of Transportation, Albany

Philip P. Brown
Wilbur M. Haas
C. W. Heckathorn
Raymond C. Herner
Henry W. Janes
Martin S. Kapp
Philip Keene
Richard E. Landau
Ivan C. MacFarlane
Harry E. Marshall
Glen L. Martin
Lyndon H. Moore
Melvin W. Morgan
Robert L. Schuster
Rockwell Smith
Robert T. Tierney
David J. Varnes
Walter C. Waidelich
William G. Weber, Jr.

COMMITTEE ON FOUNDATIONS OF BRIDGES AND OTHER STRUCTURES

(As of December 31, 1969)

Philip Keene, Chairman
Connecticut Department of Transportation, Wethersfield

Edwin C. Beethoven
Harry M. Coyle
Melvin T. Davisson
Jacob Feld
Bedrich Fruhauf
Harry D. Gibbons
Walter W. Grimes
Wayne Henneberger
William C. Hill
William P. Hofmann
William S. Housel
Horace E. Hoy
Martin S. Kapp
Richard E. Landau
Clyde N. Laughter
G. A. Leonards
Alex Rutka
Gregory P. Tschebotarioff

DIVISION C

O. L. Lund, Chairman
Nebraska Department of Roads, Lincoln

L. F. Erickson, Vice Chairman
Idaho Department of Highways, Boise

COMMITTEE ON SOIL AND ROCK PROPERTIES

(As of December 31, 1969)

G. A. Leonards, Chairman
Purdue University, Lafayette, Indiana

Richard W. Christensen
George B. Clark
Robert W. Cunny
E. D'Appolonia
Robert C. Deen
Victor Dolmage
Wilbur I. Duvall
Austin H. Emery
Charles L. Emery
Emmericus C.W.A. Geuze
Bernard B. Gordon
James P. Gould
Stanley J. Johnson
Ernest Jonas
Robert L. Kondner
Charles C. Ladd
Thurmul F. McMahon
Victor Milligan
Roy E. Olson
William H. Perloff
Shailer S. Philbrick
Hassan A. Sultan
Gregory P. Tschebotarioff
William G. Weber, Jr.
T. H. Wu

COMMITTEE ON PHYSICO-CHEMICAL PHENOMENA IN SOILS

(As of December 31, 1969)

James K. Mitchell, Chairman
University of California, Berkeley

Kandian Arulanandan
L. G. Bromwell
Richard W. Christensen
Turgut Demirel
Sidney Diamond
Donald H. Gray
Earl B. Kinter
Joakim G. Laguros
Mo Chih Li
Calvin A. Noble
Harold W. Olsen
Robert E. Paaswell
Gilbert L. Roderick
Elmer A. Rosauer
Mehmet A. Sherif
B. P. Warkentin
Hans F. Winterkorn

COMMITTEE ON ENGINEERING GEOLOGY

(As of December 31, 1969)

Ernest Dobrovolny, Chairman
Engineering Geology Branch, Denver, Colorado

A. Carter Dodson
Spenst M. Hansen
Duncan J. McGregor
John D. McNeal
Shailer S. Philbrick
Charles S. Robinson
David L. Royster
Robert L. Schuster
Rockwell Smith
Travis W. Smith

Foreword

This RECORD will be of interest to those engineers and planners involved in the location and design of embankments in areas of questionable stability, whether it be landslides, embankments, or foundations.

Froelich, through his description of the geologic setting for the Pine Mountain, Kentucky, area, points up the care that should be taken in the planning stages when construction in such areas is unavoidable. The reactivation of the dormant potential by construction or by other disturbances such as river undercutting may prove to be extremely costly and difficult to control.

Smith, McCauley, and Mearns propose that a durability absorption ratio (DAR) be used for quality control of rock slope protection material (riprap). The DAR combines two standard test methods currently being used by California, and it correlated well with 97 percent of the visual evaluation of the material. Karafiath and Nowatzki in one paper and Fang and Hirst in another address their writings to the stability of slopes. The first authors develop two approaches: an approximate method analogous to the Prandtl solution and a numerical method based on plastic equilibrium. The second authors concentrate on a closed-form plasticity solution, and present design charts for a useful range of friction angles and slope geometries.

Sherif and Koch analyzed the results of experiments using a specially designed stress meter to establish unique relationships between the precompression ratio, the coefficient of earth pressure at rest, and the liquid limit. Chae studied the effect of embedment on the interaction between foundation and soil. He develops two newly defined dimensionless parameters, the amplitude reduction coefficient and the embedment factor, by which the dynamic response of the embedded foundation can adequately be determined. Elias and Storch describe their method of construction control for a highway embankment on a weak soil. They used control charts based on effective stress stability analysis as developed by an ICES computer program. These charts relate factor of safety to pore pressures measured during construction. Thoms and Arman used gelatin of different stiffness to represent the placement of an embankment on a soft organic soil. The gelatin was studied for displacement and stress through both an inked grid and a photoelastic fringe measurement. Among the cross sections studied was one using the trench section, parallel to the embankment, that sometimes serves as a waterway to transport bulk material to the job. The results indicated that, unless other considerations are overriding, the use of the trench section is not recommended. Elnaggar and Krizek present a statistical procedure to describe consolidation data and an approximate method to estimate consolidation settlements. The technique is presented in graphical form and is illustrated by examples.

Contents

Geologic Setting of Landslides Along South Slope of Pine Mountain, Kentucky

ALBERT J. FROELICH, U.S. Geological Survey, Middlesboro, Kentucky

Landslides along the south slope of Pine Mountain in southeastern Kentucky are integrally related to bedrock geology. Most of the slides are planar block glides of sandstone and interbedded shale and siltstone that have slid down dip slopes on floors of shale, coal, or underclay. The central portion of a ½-mile wide slide that had been stable for many years recently slid when the toe was cut into during highway construction. The old slide probably originated as a planar block glide, but it developed rotational aspects at the toe and flanks. Strata underlying the south slope of Pine Mountain are of Pennsylvanian age and include massive sandstone, interbedded siltstone and shale, and thin beds of coal and underclay. Beds dip generally southeastward but flatten abruptly at the foot of the mountain and are nearly horizontal south of it. The Cumberland River follows this flexure along much of Pine Mountain and in many places cuts laterally against the dipping beds. Landslides have repeatedly occurred and others may occur where dipping strata of Pine Mountain are undercut by rivers or by construction work. Old but presently stable slides may be reactivated when cut into by highway or other excavations.

•PINE MOUNTAIN, with about 1,500 ft of relief, trends northeasterly for 100 miles across southeastern Kentucky (Fig. 1). Roads are under construction and others are being planned around, across, or through Pine Mountain as a part of the Appalachian Highway Development Project. Recent geologic mapping under a cooperative program of the Kentucky Geological Survey and the U.S. Geological Survey has demonstrated that landslides along the south slope are related to geologic structure and stratigraphy. The following discussion is based mainly on field examinations and observations of aerial photographs in the Wallins Creek quadrangle, where the geologic setting is representative of most of Pine Mountain. The purpose of this paper is limited to setting forth the geologic framework of landslides along the south slope of Pine Mountain.

Bedrock along the south slope of Pine Mountain includes part of the Breathitt Group and Lee Formation, both of Carboniferous age (Fig. 2). The upper part of the Lee Formation and the basal sandstone of the Breathitt Group (Fig. 3) consist largely of resistance hogback-forming sandstone beds that are not disrupted by landslides. The overlying strata are largely an incompetent sequence of interbedded siltstone, impure sandstone, carbonaceous clay shale, and coal with underclay. Several hundred feet of these beds underlie the foothills south of Pine Mountain. Ancient and all recent landslides north of the Cumberland River have occurred in these strata.

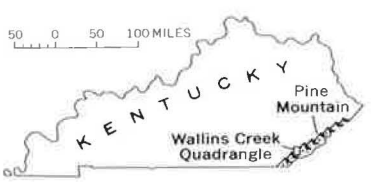

Figure 1. Index map.

The structural setting is shown by a simplified geologic map of the northern part of the Wallins Creek

Paper sponsored by Committee on Engineering Geology and presented at the 49th Annual Meeting.

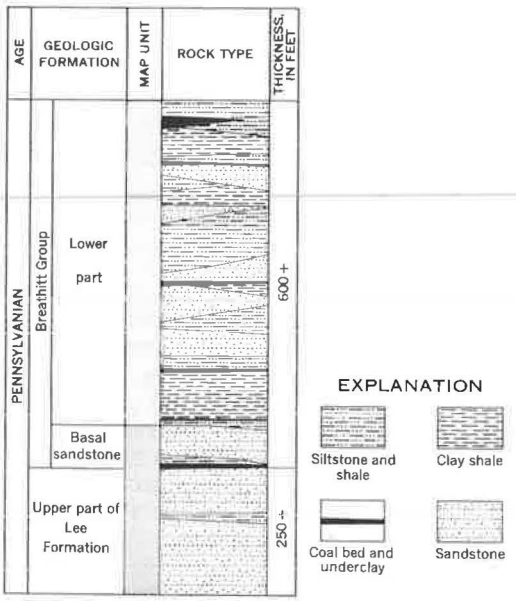

Figure 2. Generalized lithology of strata exposed along south slope of Pine Mountain in Wallins Creek quadrangle.

Figure 3. Resistant sandstone typical of upper part of Lee Formation in foreground, overlain by interbedded siltstone, shale, coal, and impure sandstone of the Breathitt Group. Strata dip southeastward. View is northeastward; Pine Mountain is to left and Cumberland River is on right.

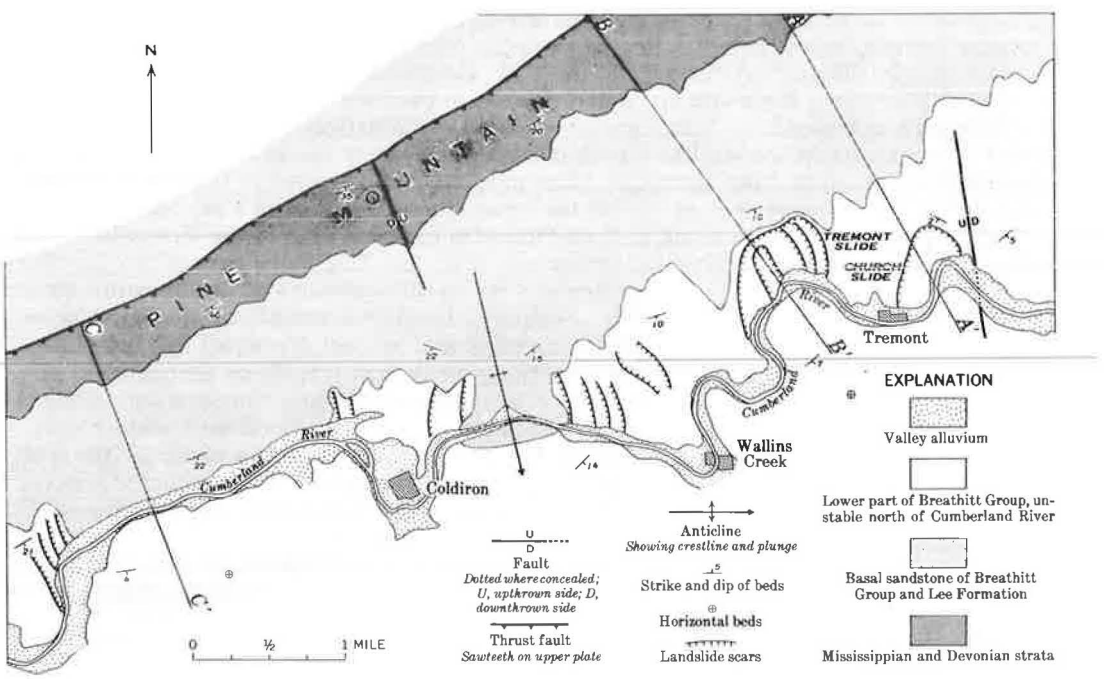

Figure 4. Generalized geologic map of northern part of Wallins Creek quadrangle, Kentucky.

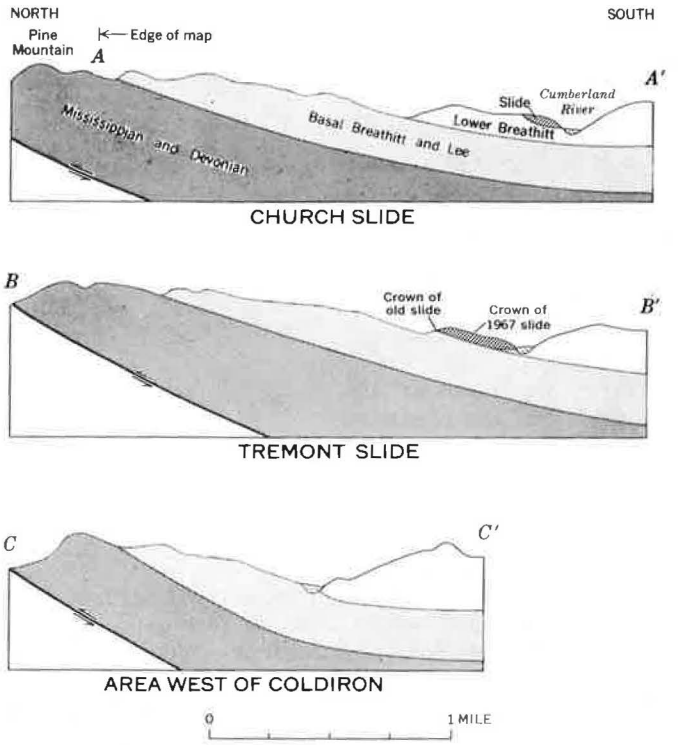

Figure 5. Cross sections showing relation of landslides to geology and position of Cumberland River.

quadrangle (Fig. 4). The regional strike of the Lee Formation is northeasterly, and beds dip generally southeastward from 10 to 40 degrees. The Breathitt strata dip generally southward from 5 to 20 degrees but are gently warped by minor transverse folds and cut by several faults and numerous joints perpendicular to the regional trend. The beds flatten abruptly near the foot of Pine Mountain and are nearly horizontal south of it. The narrow valley of the Cumberland River follows this flexure along much of the mountain, and in many places the river cuts laterally into the dipping beds.

Figure 6. Strata in lower, unstable part of Breathitt Group at Church slide. Roadbed taken out by 1969 slide, rebuilt on strata that continue intermittent down-dip movement toward observer.

Relations among geology, topography, and landslides are shown by three cross sections. The Church slide, northeast of Tremont, is shown in cross section A-A′ (Fig. 5); it is wholly within bedrock of the lower part of the Breathitt. The Church slide is on the west flank of a local transverse flexure that is cut by a small fault. Although the strata dip less than 10 degrees toward the Cumberland River, they are unstable even at that low angle. During road construction in 1968, a 50-ft thick plate of sandstone and siltstone about 800 ft wide by 500 ft long failed and slid

Figure 7. West scarp of the 1967 Tremont slide showing scar on old landslide debris. Bedrock visible in middle background along old landslide scar, dips about 10 degrees to left. View is northwestward (Deen and Havens, 2).

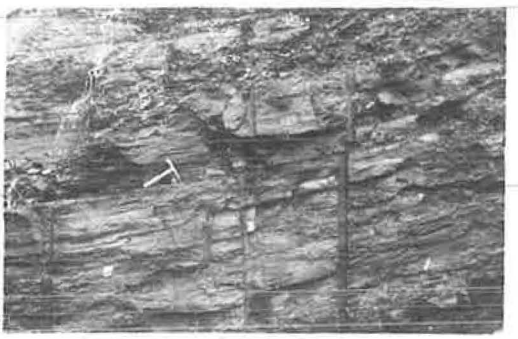

Figure 8. Offset boreholes in shale and siltstone intersected by road cut. Sliding of plates along bedding planes is toward observer in direction of dip of strata with lower plate having moved relatively more than upper.

along a floor of coal and underclay. The unstable bedrock upslope from the slide was removed by the contractors. Nevertheless, several hundred feet of highway reconstructed across the slide slipped into the river in 1969 (Fig. 6).

The slide west of Tremont is an old planar block glide of the type described by Varnes (1). The debris of the ancient slide, as much as 80 ft thick, consists of a jumble of blocks, mostly sandstone, enclosed in a gummy matrix of clay, shale, and siltstone. The old slide is 3,000 ft wide, 2,000 ft long, and drops 400 ft from crown to toe. The crown and flanks are marked by prominent scarps and the main body of the slide is characterized by irregular, hummocky topography. Large slumped and rotated sandstone blocks, most with up-slope dip, mark the toe and flanks. Cross section B-B′ (Fig. 5) shows that the Tremont slide is within, but near the base of, the lower part of the Breathitt. The river here is closer to Pine Mountain and is cutting into beds with steeper dip than at the Church slide. In July 1967, after heavy rains, the central part of the old slide gave way. It slid across the road then being constructed across the toe of the slide and into the river. That slide was 600 ft wide, 1,400 ft long, and had a 200-ft drop from crown to toe, as described by Deen and Havens (2). New scarps clearly show that the recent slide resulted from reactivation of the old (Fig. 7).

The third example, cross section C-C′ (Fig. 5), is west of Coldiron where for 2 miles no lower Breathitt is present north of the river. The lower Breathitt rocks long

Figure 9. Southwestward view of deep roadcut west of Wallins Creek quadrangle where sandstone, shale, and siltstone in lower part of Breathitt Group slid down a dip slope into the excavation.

Figure 10. Joint face, above front end of truck, at edge of landslide scarp. Joints exert control over slides by dividing dipping bedrock into segments.

ago slid into the river, leaving resistant beds of sandstone at the surface. Areas such as this are characterized by relatively straight courses of the river, which contrast with the meander pattern in the nearly flat-lying Breathitt. Dip slopes on sandstone are smooth, moderately steep (15 to 25 degrees), and are bounded by remnants of unstable lower Breathitt rocks flanked by prominent landslide scars.

Where the lower part of the Breathitt remains north of the river, much of it is slowly moving down dip, even in areas not mapped as landslides. Drill holes made just prior to recent road cut excavation are offset (Fig. 8), indicating movement along slippage or glide planes that are parallel or subparallel to bedding planes. Thick beds of sandstone have slid down dip slopes on coal beds or shale (Fig. 9) into recent road cuts. Slides are aided by joints (Fig. 10) that have broken the bedrock into discrete units, which may move coherently.

The foregoing has described the general geologic framework of the landslides along the south slope of Pine Mountain. Variations in the dip of the strata, presence of joints, small folds and faults, and the action of groundwater, all of which may play critical roles in localizing landslides, are beyond the scope of this report. In summary, landslides have taken place where the Cumberland River is cutting beds of shale, siltstone, coal, clay, and sandstone in the lower part of the Breathitt Group that are dipping toward the river, and old landslides have been reactivated where disturbed by construction work. If local geologic conditions are known in advance, potentially unstable areas may be predicted, slide-prone localities bypassed, and construction planned to avoid disturbing natural equilibrium.

REFERENCES

1. Varnes, D. J. Landslides and Engineering Practice. HRB Spec. Rept. 29, 1958, pp. 20-47.
2. Deen, R. C., and Havens, J. H. Landslides in Kentucky. Kentucky Department of Highways Research Report, 1968.

Evaluation of Rock Slope Protection Material

TRAVIS SMITH, MARVIN L. McCAULEY, and RONALD W. MEARNS,
Materials and Research Department, California Division of Highways

A study of quality control of rock slope protection material (riprap) is reported. The objectives of the study were to determine what rock properties were important for satisfactory slope protection and to develop workable specifications that would provide satisfactory quality control with minimum cost. An extensive field evaluation of rock slope protection materials was performed, and samples were obtained for physical testing. A significant finding of this visual and physical evaluation was that the 1964 California Standard Specifications were too severe and resulted in the rejection of satisfactory rock. Test methods evaluated as potential specifications are sodium sulfate soundness, Los Angeles rattler, apparent specific gravity, absorption, durability index, wet-dry, freeze-thaw, rapid abrasion, petrography, X-ray diffraction, differential thermal analysis, and durability absorption ratio (DAR). The DAR combines the results of easily performed and inexpensive tests that are relatively accurate in predicting performance and that measure complementary physical properties. The DAR correlates with visual evaluation 97 percent of the time, and the California Division of Highways is converting to this specification for quality control of rock slope protection material.

•THE NUMBER, size, and cost of highway construction projects have increased rapidly in recent years. Accompanying this increased construction activity has been an ever-increasing need for adequate rock slope protection material (known as riprap). To fill this need, the various districts of the California Division of Highways have frequently requested waiving or modifying the quality control requirements of the Standard Specifications. Apparently the quality control provided by the Standard Specifications was somewhat conservative.

The California Division of Highways first utilized Standard Specifications for controlling the quality of rock slope protection material in 1935. Modifications of the Standard Specifications to make them conform to the known performance of various materials throughout the state have not been completely successful. Table 1 gives the history of the Division's Standard Specifications.

In 1963, the California Division of Highways, with the cooperation of the U. S. Bureau of Public Roads, began a study of quality control for rock slope protection material. The objectives of this research project were (a) to determine the properties of rock that were important in satisfactory rock slope protection material and (b) to develop workable specifications based on physical tests that would provide satisfactory quality control with minimum cost.

To achieve the objectives of this project, two avenues of investigation were followed. The first consisted of an extensive field evaluation of rock slope protection installations throughout the state. The second was a thorough study of common physical test methods that were believed to have potential for evaluating the quality of rock slope protection material. This report describes the methods that were used in conducting this investigation and discusses the results.

Paper sponsored by Committee on Soil and Rock Properties and presented at the 49th Annual Meeting.

TABLE 1

HISTORY OF STANDARD SPECIFICATIONS FOR ROCK SLOPE PROTECTION MATERIAL IN CALIFORNIA

Test Specifications	1935	1940	1960	1964	1969
Apparent specific gravity, minimum	2.5	2.5	2.5	2.5	2.5
Absorption, maximum (percent)	—	—	2	2	2
Sodium sulfate soundness, maximum loss (percent)	—	—	5	5	10
Los Angeles rattler, maximum loss (percent)	37	40	45	45	—
Wet shot rattler, maximum loss (percent)	37	37	40	—	—

EVALUATION OF INSTALLATIONS

A total of 65 installations were inspected, and the field performance of the material was determined. These installations are located throughout the state and in climatic environments that vary from marine shoreline to high mountains to desert. The rocks on each of these installations were classified as igneous intrusive, igneous extrusive, metamorphic, or sedimentary. The selection of installations evaluated was based on the desire to include a wide range of both environment and rock types.

The performance of rock on each of the installations was categorized as either "good" or "unsatisfactory" by visually studying such factors as hardness, shape, fractures, weathering, resistance to abrasion, and mineral decomposition. All classifications of rock were found in each performance category, except that no igneous intrusive rocks were categorized as unsatisfactory. To eliminate the human variable as much as possible, the same two engineering geologists conducted the inspection of all installations included in this study.

Two factors (age of the installation and environment) that were not used in evaluating the performance of rock on an installation should be mentioned at this point. The age of an installation is not considered a critical factor in the performance of an initially sound rock. Rocks found to be disintegrating on an installation were also found to be of poorer quality and their condition of failure cannot be attributed to the relatively short period of exposure on the installations. Although the environment itself was not considered in evaluating the performance of a material, the properties of the material affected by environment were considered. The presence of fractures or voids that could be opened by freezing water and the presence of minerals that expand when wet or hot are examples of properties considered that may become significant in a given environment.

A very important part of the inspection procedure was the obtaining of representative samples for use in the testing phase of this research project. Photographs of the installation and of the material were also taken as part of the inspection (Figs. 1, 2, 3, 4, 5, and 6).

During this phase of the investigation, the field performance of the rock was correlated with the individual Standard Specification tests, with visual evaluation of a sample of the rock by an experienced engineer or geologist, and with the entire Standard Specifications. The method having the highest percentage of agreement (94 percent) with field performance was visual evaluation. The absorption test was a close second (91 percent agreement). The entire Standard Specifications had the lowest percentage of agreement (71 percent).

Visual evaluation, although extremely reliable, is difficult to use as a specification. In this project, the accuracy of the various methods of determining rock quality was calculated using field performance or visual evaluation as references. This provided a ready value for comparison between tests, although the absolute accuracy of any given method may vary by as much as 6 percent from the comparative value. Table 2 gives a summary of the percentage of correlation of various quality determination

Figure 1. Good installation of sedimentary and igneous rocks. Severe rounding caused by wave action.

Figure 2. Good installation of sedimentary rock in place for 23 years. This material does not comply with the Standard Specifications.

Figure 3. Unsatisfactory installation of good igneous rock.

Figure 4. Good metamorphic rock in place for 8 years.

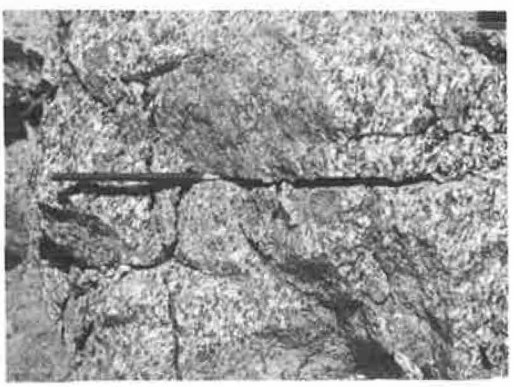

Figure 5. Unsatisfactory igneous rock.

Figure 6. Unsatisfactory sedimentary rock.

TABLE 2

CORRELATION OF VARIOUS METHODS OF EVALUATING THE QUALITY OF ROCK SLOPE PROTECTION MATERIAL

Test Method	Specification	Number of Samples	Correlation (percent)
Apparent specific gravity	2.5 minimum	65	86[a]
Absorption	2 percent maximum	65	91[a]
Los Angeles rattler	45 percent maximum loss	65	83[a]
Sodium sulfate soundness	5 percent maximum loss	65	77[a]
1964 Standard Specifications		65	71[a]
Durability index	52 minimum	264	94[b]
Rapid abrasion	24 percent maximum loss	112	88[b]
Durability absorption ratio	>23, acceptable <10, unacceptable 10-23, acceptable if durability index >51	261	97[b]
Visual evaluation		65	94[a]

[a]Correlation with field performance only.

[b]Correlation with field performance or visual evaluation.

methods with field performance or visual evaluation. Visual evaluation is given in the same table and is compared to known field performance.

The most significant finding of this evaluation of installations was the fact that 29 percent of the rocks that had performed satisfactorily in the field failed to comply with the Division's 1964 Standard Specifications. Obviously, the Standard Specifications were too severe, resulting in the rejection of satisfactory material and in the numerous requests for waiving or modification to permit the use of materials with known performance records.

Another weakness of these specifications was the apparent discrimination against different types of rock by some of the test methods. The term "discrimination" as used in this report refers to the rejection by a given specification of a disproportionate number of samples of satisfactory material of a given rock type. Igneous intrusive rocks exhibit unusually high losses in the Los Angeles rattler test. Igneous extrusive rocks have unusually high percentages of absorption. Sedimentary rocks have unusually high losses in both the Los Angeles rattler test and the sodium sulfate soundness test.

Because of the severity of the Standard Specifications, the discrimination against rock type, and the relative inaccuracy of the tests in predicting rock performance at an installation, a thorough study of the specification test methods was undertaken.

TEST METHODS—STANDARD SPECIFICATIONS

In order to efficiently and effectively evaluate the factors being studied, a data retrieval system was necessary. After some study, a 5- by 8-in. card file incorporating an edge-punched data retrieval system was developed.

This card file contains data on all samples of rock slope protection material submitted for use by the California Division of Highways between January 1, 1957, and June 30, 1968. The categories of data that are retrievable from this card file include whether the sample passed or failed the 1964 Standard Specifications, test results, rock classification, location and age of the installation, and type of environment. The rock classification and installation location were number-coded to reduce the number of edge-punched spaces required. This system has been satisfactory and provides a means for efficient data analysis, as well as serving as a permanent record of data on rock slope protection materials.

Sodium Sulfate Soundness Test (Test Method No. Calif. 214-D)

The 1964 Standard Specifications of the California Division of Highways permitted a 5 percent maximum loss in the sodium sulfate soundness test. Analysis of data from

the card file showed that this specification correlates with visual evaluations 83 percent of the time. Further study showed that a specification limit of 10 percent maximum loss would raise this percentage of correct predictions to approximately 88 percent. The California Division of Highways adopted this specification limit of 10 percent in June 1967.

As previously noted, the soundness specification discriminates against sandstone. Sandstone makes up only 25 percent of all samples tested but is nearly 50 percent of all samples that failed the soundness test. Another inherent disadvantage of the soundness test is that a minimum of 10 days is required to obtain results. The period of time is too long for efficient quality control of construction materials. These two facts have created doubts as to the effectiveness of the soundness test as a specification for rock slope protection material.

Los Angeles Rattler Test (Test Method No. Calif. 211-C)

The 1964 Standard Specifications of the California Division of Highways permitted a maximum loss of 45 percent in the Los Angeles rattler test. Analysis of data indicated that the Los Angeles rattler test correlated with visual evaluations 83 percent of the time. Approximately 10 percent of all samples tested failed the Los Angeles rattler test. Most of the samples failing the Los Angeles rattler test also failed one of the other Standard Specification tests. Of those samples that failed the Los Angeles rattler specification without also failing one of the other specification tests, approximately 25 percent have satisfactory performance records.

Because only a small percentage of samples failed to comply with the Los Angeles rattler specifications without also failing to comply with one of the other specifications, because even this small number of samples showed a significant percentage of incorrect predictions of performance, and because the Los Angeles rattler test has been demonstrated to discriminate against igneous intrusive rocks and sedimentary rocks, it was felt that the Los Angeles rattler test was not a satisfactory specification test. The California Division of Highways deleted the Los Angeles rattler specification in June 1967.

Apparent Specific Gravity (Test Method No. Calif. 206-D)

The 1964 Standard Specifications of the California Division of Highways specified a minimum apparent specific gravity of 2.5. Approximately 91 percent of all samples tested complied with this specification. The apparent specific gravity test correlated with visual evaluation approximately 86 percent of the time. The specification for apparent specific gravity assured the use of rock of sufficient density to remain in place, an important consideration in designing adequate slope protection installations. For this reason, the apparent specific gravity is still used as a specification test for rock slope protection material.

Absorption (Test Method No. Calif. 206-D)

The 1964 Standard Specifications of the California Division of Highways allow a maximum absorption of 2 percent. Using this specification, the absorption test correctly predicted performance approximately 91 percent of the time. Although this test method obviously discriminates against igneous extrusive rocks, it was kept in the 1969 Standard Specifications because it has one of the highest percentages of correct performance predictions.

Summary of Tests Used

In concluding the discussion on these four 1964 Standard Specification tests, it should be pointed out that even though the tests individually have relatively good correlations with visual evaluations, collectively they are only accurate approximately 71 percent of the time. If the 10 percent soundness specification revision is applied on the same set of data, the accuracy increases to 77 percent.

TEST METHODS—MISCELLANEOUS

The test methods described in the following are by no means a complete set of tests for evaluating the quality of rock. They are tests that have been recommended for use in determining the quality of rock slope protection material, or they are tests that other agencies use with varying degrees of success in determining rock quality. Because our objective was to determine a specification based on physical test results that would be inexpensive and quick to perform and that would correlate well with performance, the study was terminated when such a test method was found. Brief descriptions of our findings on the test methods that were investigated in this study are included in the remainder of this report.

Durability Index (Text Method No. Calif. 229-E)

The durability index is, to some extent, a measure of the quality and quantity of fine material washed or abraded from the surface of the material being tested. Analysis of data indicates that a minimum durability index of 52 would correctly correlate with visual evaluation 94 percent of the time. Although this is substantially better than the existing Standard Specifications, this test method was not recommended as a specification for an individual test because of its tendency to discriminate slightly against igneous intrusive rocks and to favor igneous extrusive rocks.

Wet-Dry Test

The wet-dry test method used in this study was as follows: A 2,500-gram sample of crushed rock fragments was placed in a stainless steel basket and alternately submerged in water and oven-dried. Wet-dry testing was normally terminated after 15 cycles. The sample was then shaken for 2 minutes in a mechanical sieve shaker to shake off any loose or small-sized particles. The sample was then reweighed and the percentage loss was calculated. Our investigation of this test method indicated that it lacked severity, small fragments had more loss than large fragments, tap water was more severe than seawater, wetting agents did not appreciably increase the severity of the test, and increasing soaking and drying time or increasing the number of cycles did not necessarily increase the percentage loss.

The extremely small losses with this test method made it difficult to correlate with visual evaluation or known performance. The inability to obtain correlation with visual evaluation or performance and the relatively long time required to perform the test indicated that this test method was not satisfactory for quality control purposes.

Freeze-Thaw Test

The freeze-thaw test method was designed to determine the effect of alternate freezing and thawing of samples of rock slope protection material. The temperature range used in this test was -16 F to +65 F. The thawing of the samples was accomplished by circulating ordinary tap water around the samples. All of the tests were terminated at 200 cycles. It is believed that the conditions existing in this test procedure closely simulate actual field conditions on an installation at which alternate freezing and thawing occur. The freeze-thaw test method was found to be unsatisfactory as a quality control test for rock because of the time required to perform the test and because of the small percentage loss by this test method. As in the case of the wet-dry test, the losses in the freeze-thaw test were so small that no correlation between them and the performance of the material could be determined. The test does have value in evaluating the degree to which such features as foliation, fractures, and veins affect the performance of a rock under freeze-thaw conditions.

Rapid Abrasion Test

The rapid abrasion test method used in this study was developed by the California Division of Highways. The study of this method was based on the assumption that there is some correlation between the resistance of rock to water-borne abrasives and the ability to provide adequate protection on rock slope protection installations.

The test method was adapted from the tumbling technique used by "rock hounds" for polishing small rocks. It consisted of tumbling, for a given period of time, a sample of crushed rock together with water and commercial abrasives. After tumbling the sample, it was washed and oven-dried, and the percentage of weight loss was calculated. Using a specification of 24 percent maximum loss, this test method correlated with visual evaluation for 88 percent of the samples. Although this test method was somewhat more accurate than the 1964 California Standard Specification tests for determining the quality of rock slope protection material, it was not recommended as a specification test because the property of abrasion resistance is not necessarily the most significant property on a given installation. The test method also discriminates significantly against igneous intrusive and metamorphic rocks and favors igneous extrusive rocks.

Petrologic Methods

Petrography, X-ray diffraction, and differential thermal analysis are three methods of classification and mineral identification available at the Materials and Research Laboratory. Petrography is the only method regularly used for evaluating rock slope protection at this time. However, there are no specifications for this method and, although it has been shown to be more accurate in predicting performance than any of the specification tests, no specification is anticipated. The X-ray diffraction and differential thermal analysis methods are used when detailed information on mineral composition is desired for a sample of special interest. The combined results from these three methods yield information that (a) can be used for predicting the performance of rock slope protection material and (b) cannot be obtained or inferred from the specification test results.

It is believed that greater used should be made of these methods to determine the probable performance of rock slope protection material. However, to obtain meaningful results from these specialized techniques they must be performed by qualified personnel experienced in their use.

Durability Absorption Ratio

The combining of test results in a formula was considered desirable as a specification for rock slope protection material because it would allow the use of material that is weak in one property but is strong enough in some other property to compensate for the weakness. Another advantage in combining test results in a formula is that a test method that discriminates against a material may be compensated for by a test method favoring that same material.

A desirable formula should combine the results of easily performed and inexpensive tests that are relatively accurate in predicting performance and that measure complementary physical properties. The 1964 California Standard Specification tests required 3 to 4 weeks between the time of obtaining the sample and the time of receiving complete test results. It was believed that this time lag was too long for an effective construction material quality control test. For this reason, a decision was made to work with tests that could be performed at the district materials laboratory or, in some cases, on the job. Test results could then be available within a few days of the sampling.

It was also decided that a simple formula was desirable and so only two tests, the durability index and absorption, were selected. These tests were complementary in that the durability index favors igneous extrusive rocks whereas the absorption discriminates against the igneous extrusive rocks. The results of this study were so encouraging that formulas using other tests were not tried.

The formula used was

$$\text{Durability Absorption Ratio (DAR)} = \frac{\text{Durability Index}}{\text{Percent Absorption} + 1}$$

The plus one term in the denominator was necessary to avoid complications on those samples with zero percent absorption. Analysis of data indicates that the DAR corre-

lates with visual evaluation 97 percent of the time and the results are less strongly influenced by rock type than any other test method studied. To achieve this percentage of correct predictions, the following specifications were used:

1. Durability absorption ratio greater than 23, material passes;
2. Durability absorption ratio less than 10, material fails;
3. Durability absorption ratio 10 through 23 and (a) durability index 52 or greater, material passes, and (b) durability index 51 or less, material fails.

These specification limits were obtained by determining the values that resulted in the highest percentage of correlation.

The California Division of Highways is currently converting to this durability absorption ratio specification for quality control. Its adoption will reduce the amount and cost of shipping and testing samples, will reduce from weeks to days the time required to evaluate the material, and will increase substantially the correlation with field performance in comparison to the present Standard Specifications. Of additional benefit to the state is the fact that the durability absorption ratio is a more lenient specification permitting greater use of local material and should result in lower material costs and shorter hauls. This study shows that these benefits can be realized without lowering installation performance.

REFERENCE

1. Smith, T., McCauley, M. L., and Mearns, R. W. Investigation of Rock Slope Protection Material. California Division of Highways, Res. Rept. No. 632561, interim report, April 1967; final report, June 1969.

Stability of Slopes Loaded Over a Finite Area

LESLIE L. KARAFIATH and EDWARD A. NOWATZKI,
Grumman Aerospace Corporation, Bethpage, New York

In frictional soils, when pore pressures are negligible, failure occurs in shear zones. In such cases the stability of slopes loaded over a finite area can be analyzed by bearing capacity methods. Two methods of analysis are presented: an approximate method, based on the assumption that a slip-line field analogous to the Prandtl solution for horizontal ground applies, and a numerical method, based on the numerical integration of the governing differential equations of plastic equilibrium. A formula for the N_q value is given for the slope angle, friction angle, and the angle of the inclination of load and surcharge as principal variables. The concept of stress gradient, which expresses the rate of increase of the bearing stress from the edge of the loaded area, is used to account for the effect of the weight of the soil. The stress gradients obtained by the approximate method are compared with those determined from bearing stresses obtained by numerical integration methods. Results of small-scale experiments are presented showing that the decrease of bearing capacity with slope angle can be reasonably estimated by the approximate method. The methods apply to the stability analyses of highway embankments as well as to problems in land locomotion theory.

•TYPICAL EXAMPLES of slopes loaded over a finite area are shown in Figure 1. These problems of slope stability differ from that of the stability of foundations embedded in a slope investigated by Meyerhof (1) in that the loading is at the surface.

METHODS OF ANALYSIS

The stability of slopes is usually analyzed by assuming various potential sliding surfaces and determining the most critical one by trial and error. For clays and silts the transfer of pore water from the less stressed zones to the most stressed locations results in the development of a single failure surface. Consequently, the trial and error approach to the analysis of the stability of silt and clay slopes is reasonable.

In unsaturated frictional soils, failure is generally not restricted to a single failure surface but occurs in zones of plastic failure. It is for such conditions that the method of analysis presented in this paper applies. The equilibrium of granular masses, in which no significant pore pressures develop upon loading, is governed by the differential equations of plastic equilibrium. The solution of these differential equations is a slip-line field, a classic example of which is the Prandtl slip-line field for loading on a horizontal surface of a weightless soil.

All analyses presented herein assume that failure upon loading occurs in shear zones, with plastic equilibrium conditions prevailing at every point within these zones. Two methods are applied in the analysis: an approximate method that assumes stress fields analogous to the Prandtl solution in the slopes, and a numerical method based on the

Paper sponsored by Committee on Embankments and Earth Slopes and presented at the 49th Annual Meeting.

numerical integration of the governing partial differential equations. Notation used in the analyses is defined in the Appendix.

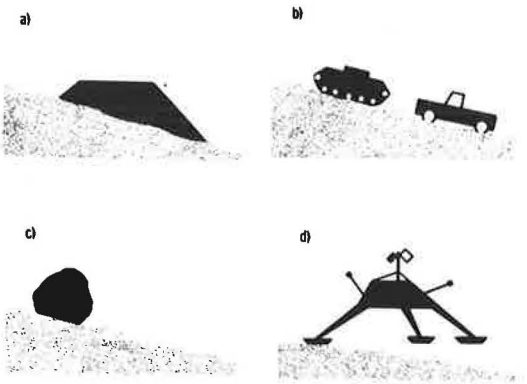

Figure 1. Examples of slopes loaded over a finite area at their surface: (a) highway embankment, (b) off-the-road vehicles, (c) lunar boulder, and (d) landing space vehicle.

ANALYSIS THAT ASSUMES FAILURE ZONES ANALOGOUS TO PRANDTL'S SOLUTION

The failure zones assumed in this analysis consist of a wedge in the active Rankine state (I, Fig. 2), a radial shear zone (II, Fig. 2) bounded by a logarithmic spiral, and a wedge in the passive Rankine state (III, Fig. 2). Both the active and passive wedges correspond to the state of stresses in an infinite slope. The pole of the logarithmic spiral that bounds the radial shear zone is assumed at the outer edge of the loaded area (point A, Fig. 2), thereby ensuring continuity of the slip lines and their tangents throughout the shear zones.

The angles of the active and passive wedges, θ_1 and θ_2 in Figure 2, can be determined (2) from the following:

$$\theta_1 = \tfrac{1}{2}\left[\frac{\pi}{2} + \varphi - (\delta + \epsilon) - \arcsin\frac{\sin(\delta + \epsilon)}{\sin\varphi}\right] \quad \text{when} \quad (\delta + \epsilon) \leq \varphi \tag{1}$$

$$\theta_2 = \tfrac{1}{2}\left[\frac{\pi}{2} - \varphi - (\lambda + \epsilon) + \arcsin\frac{\sin(\lambda + \epsilon)}{\sin\varphi}\right] \quad \text{when} \quad (\lambda + \epsilon) \leq \varphi \tag{2}$$

(For vertical surcharge only, as in Figure 2, $\lambda = 0$.) The central angles of the radial shear zone are

$$\beta_1 = \theta_1 + \epsilon - \varphi$$

and (3)

$$\beta_2 = \frac{\pi}{2} - \theta_2 - \epsilon$$

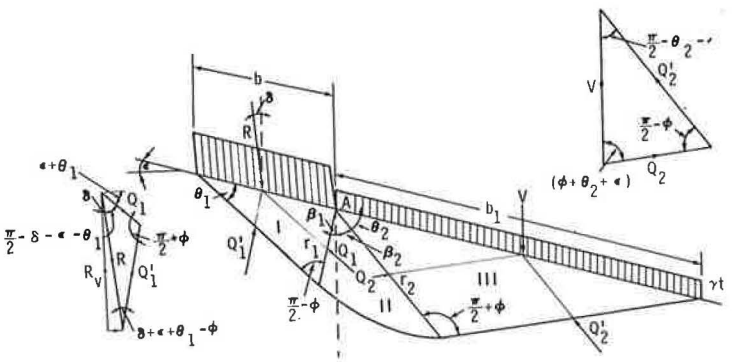

Figure 2. Shear zone geometry for sloping surface analogous to Prandtl's solution.

If the weight of the soil is disregarded and cohesion is zero, the bearing capacity can be expressed as

$$q_{uv} = pN_q \tag{4}$$

The N_q factor is determined from the equilibrium of moments about point A. For a uniform surcharge, the distribution of stresses at the sides of the active and passive wedges is uniform, and the resultants of these stresses, Q_1 and Q_2, act at the middle of these sides. All forces can be determined from the vector diagrams of Figure 2. Because the resultant of the stresses acting on the logarithmic spiral passes through the pole, $Q_1 \cos \varphi(r_1/2) = Q_2 \cos \varphi(r_2/2)$. After substitutions and rearrangements,

$$N_q = \frac{\cos(\lambda + \epsilon + \theta_2) \cos \delta \sin \theta_1}{\sin(\delta + \epsilon + \theta_1 - \varphi) \cos(\varphi + \theta_2) \cos \lambda} e^{2(\beta_1 + \beta_2) \tan \varphi} \tag{5}$$

Figure 3 shows the N_q values for vertical loading and slopes varying from $\epsilon = 0$ to $\epsilon = 30$ deg.

For the determination of the effect of cohesion, the relationship $N_c = (N_q - 1) \cot \varphi$ used by Terzaghi and others in bearing capacity formulas for level ground is only approximately valid. For the case of sloping ground, cohesion can be taken into account by using reduced stresses, which are the vectorial sum of ψ and the surcharge or bearing stresses. The reduced stresses are indicated by primes in Figure 4. Equation 4 is valid for the primed stresses and the N_q value can be calculated for any inclination of the reduced bearing stress from Eq. 5. The inclination of the reduced surcharge and bearing stresses can be determined from the vector diagrams in Figure 4.

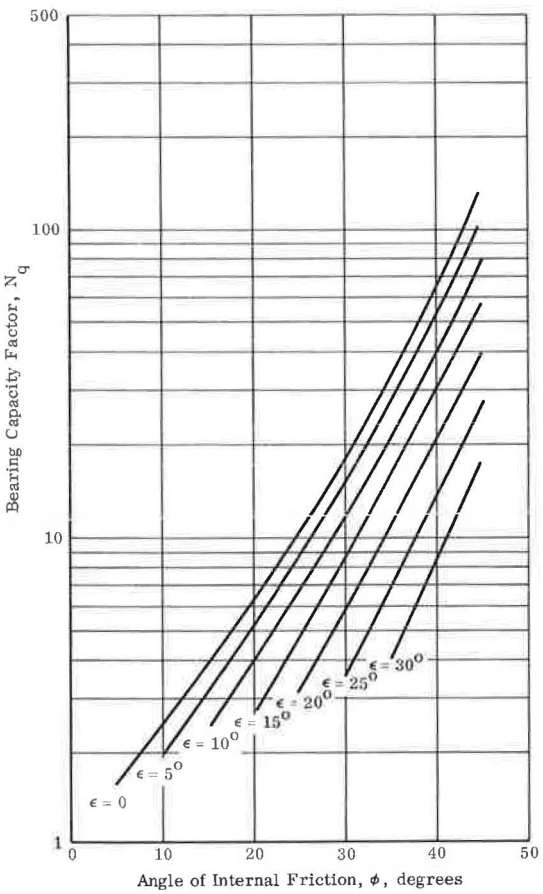

Figure 3. Bearing capacity factor, Nq, for sloping ground and vertical strip-loading ($\lambda = \delta = 0$).

Equation 5, derived on the basis of a slip-line field for weightless soil, is also valid if the soil possesses weight. This follows from the numerical solution of the governing differential equations presented in the next section where the stresses at the singular point A are computed as if that point were a degenerated logarithmic spiral, the same as in the Prandtl solution. The part of the bearing stress that is uniformly distributed is due to the surcharge, whereas the part that increases with the distance from the edge of the loading is due to the weight of the soil. The stress at point A is equal to the uniformly distributed part; therefore, it is the same in both solutions.

To consider the effect of the weight of the soil, it is assumed that it acts on the slip-line field used for the determination of the N_q value without changing the directions of the slip lines. This assumption is necessary in order to arrive at a closed form solution; the change of

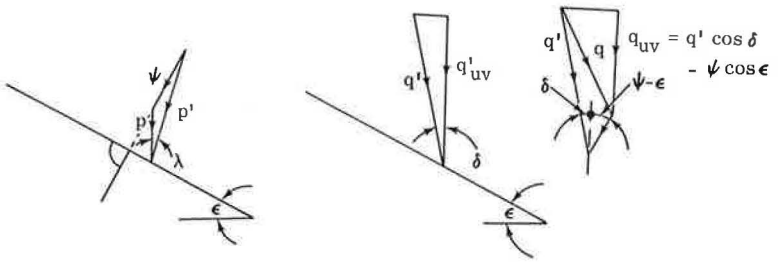

Figure 4. Force diagrams for the determination of reduced stresses.

the slip-line field resulting from the weight of soil is investigated in the next section by numerical integration methods. In a previous study (3), N_γ factors were determined on the basis that the point of attack of the resultant bearing force is such that it meets the equilibrium requirements of the active wedge on which the weight forces act (Fig. 5a). Further studies showed that it is possible to meet the equilibrium requirements for other locations of the resultant bearing force if splitting of the active wedge along the slip lines into two wedges is permitted (Fig. 5b) and the forces resulting from the weight of soil are balanced by triangular bearing stresses. This leads to the concept of stress gradient, i.e., the rate of increase of normal bearing stresses resulting from the effect of weight of the soil (Fig. 6).

In the case of a loaded slope, the stress gradient at the downslope part of the loaded area is different from that at the upslope part. The two stress gradients determine the triangular loading that the soil can ultimately carry due to its own weight. These stress gradients are determined as follows.

The active wedge of the slip-line field used for the determination of the N_q value (Fig. 2) is divided into two smaller wedges along the slip lines (Fig. 5b). The common point of the two wedges (point C in Fig. 5b) is determined by the condition that the bearing stress at this point computed from either wedge be equal. The location of this point is not known beforehand; it is determined from the stress gradients, which are independent of the width of the wedges.

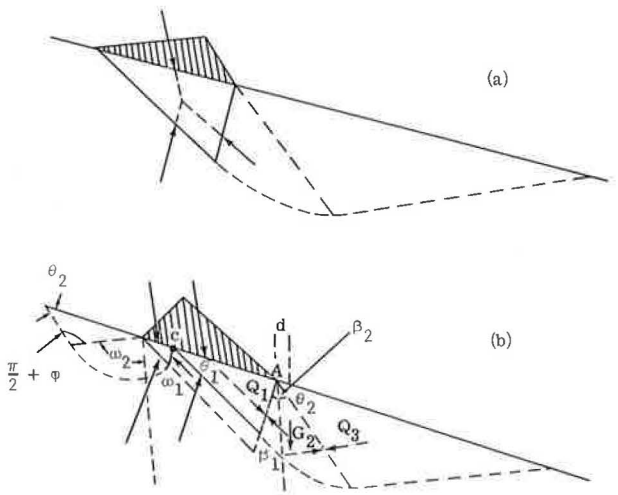

Figure 5. Effect of weight of soil: (a) stress distribution compatible with weight forces acting on the whole active wedge; (b) stress distribution assuming two active wedges corresponding to downslope and upslope failure.

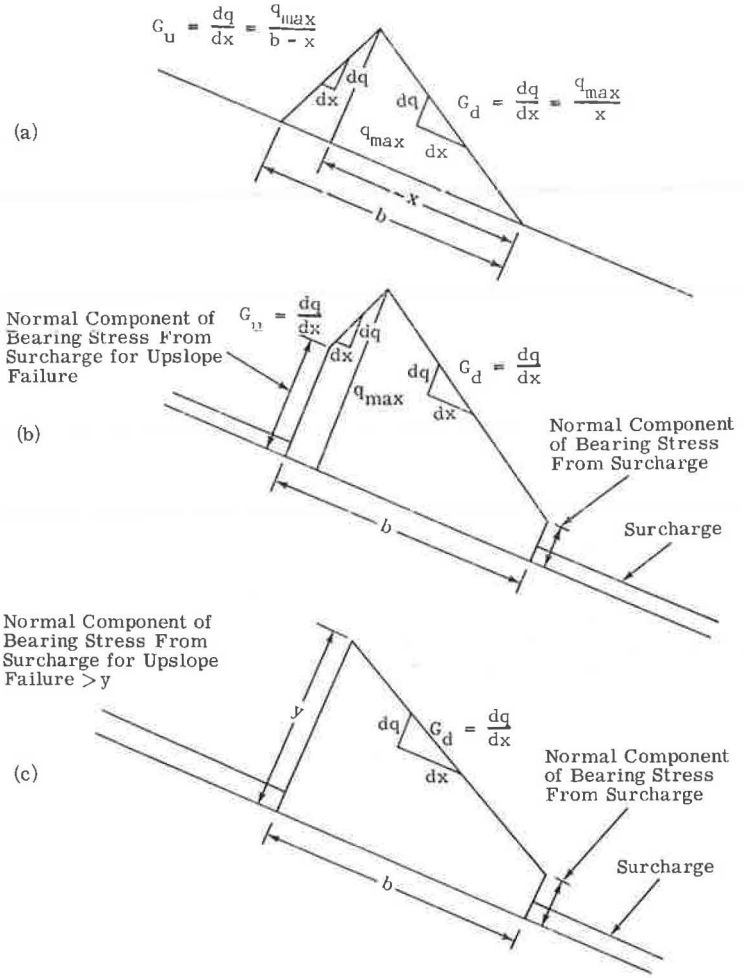

Figure 6. Distribution of bearing stresses: (a) no surcharge; (b) surcharge–upslope and downslope failure; and (c) surcharge–downslope failure only.

For the computation of the upslope gradient, however, the θ_1 and θ_2 angles are replaced by angles ψ_1 and ψ_2, and the β_1 and β_2 angles are replaced by angles ω_1 and ω_2. The values of these angles are

$$\psi_1 = \theta_1 \qquad \psi_2 = \frac{\pi}{2} - \varphi - \theta_2 \tag{6}$$

$$\omega_1 = \frac{\pi}{2} - \psi_1 - \epsilon \qquad \omega_2 = \frac{\pi}{2} + \epsilon - \psi_2 \tag{7}$$

The resultant bearing force R is determined on the basis of equilibrium considerations similar to those used in the determination of N_q. The stresses at the sides of the passive wedge and the radial shear zone increase linearly, and the point of attack of the resultant of these stresses is at the lower third of the sides. The resultant of the stresses acting on the logarithmic spiral portion passes through point A; therefore, it need not be considered. Other acting forces are Q_1, Q_3, and the weight of the radial shear zone G_2. The moment equilibrium about point A for the forces acting on the radial shear zone is expressed as

$$-(Q_1)\cos\varphi\,\frac{2}{3}\,r_1 + dG_2 + Q_3\cos\varphi\,\frac{2}{3}\,r_2 = 0 \tag{8}$$

From the vector diagram in Figure 2, the resultant bearing force is

$$R = Q_1\,\frac{\sin(\pi/2 + \varphi)}{\sin(\delta + \theta_1 + \epsilon - \varphi)} \tag{9}$$

After substitutions and rearrangements, the downslope stress gradient can be expressed as

$$G_d = \gamma\,\frac{\dfrac{\sin^2\theta_1}{\cos^2\varphi}\cdot A + \dfrac{\sin^2\theta_1\sin\theta_2\cos(\theta_2 + \epsilon)\,e^{3(\beta_1 + \beta_2)\tan\varphi}}{\cos\varphi\cos(\varphi + \theta_2)}}{\sin(\delta + \theta_1 + \epsilon - \varphi)\sec(\delta + \epsilon)} \tag{10}$$

where

$$A = \frac{1}{9\tan^2\varphi + 1}\,(3\tan\varphi\sin\beta_2 - \cos\beta_2)\cdot e^{3(\beta_1 + \beta_2)\tan\varphi} + (3\tan\varphi\sin\beta_1 + \cos\beta_1) \tag{11}$$

The upslope stress gradient, computed similarly, is

$$G_u = \gamma\,\frac{\dfrac{\cos^2(\varphi - \psi_1)}{\cos^2\varphi}\cdot A' + \dfrac{\cos^2(\varphi - \psi_1)\sin\varphi_2\cos(\epsilon - \psi_2)}{\cos\varphi\sin\theta_2}\,e^{3(\omega_1 + \omega_2)\tan\varphi}}{\cos(\delta + \epsilon + \psi_1)\sec(\delta + \epsilon)} \tag{12}$$

where A' is computed by replacing β_1 and β_2 by ω_1 and ω_2 in Eq. 11. Figure 7 shows G_d/γ and G_u/γ for vertical loadings and slopes ranging from $\epsilon = 0$ to $\epsilon = 30$ deg.

The equations for the stress gradients can also be conveniently used to determine the effect of the weight of soil on the bearing capacity in the case of level ground and inclined loading. In this case $\epsilon = 0$, and downslope and upslope mean in and opposite to the direction of loading respectively. If there is no surcharge, the maximum bearing stress is at a distance (Fig. 6a)

$$x = \frac{G_u}{G_d + G_u}\,b \tag{13}$$

from the downslope edge of the loading. Its normal component is

$$q_{max} = \frac{G_u G_d}{G_u + G_d}\,b \tag{14}$$

The average of the normal component of the bearing stress in the two-dimensional case is $q_{av} = \frac{1}{2}\,q_{max}$; for the axially symmetric case, it is $q_{av} = \frac{1}{3}\,q_{max}$. Note that the ratio of the average bearing stress in the axially symmetric case to that in the two-dimensional case is 0.66, which approximately corresponds to the 0.6 shape factor for average bearing stresses suggested by Terzaghi. Thus, if the method of stress gradients is used, it is not necessary to consider shape factors for the various types of three-dimensional loadings. This is particularly advantageous when the loading of slopes is considered, because shape factors for this case have not yet been experimentally established.

In the case of a surcharge, the stress gradients expressing the effect of the weight of the soil on the load-bearing capacity have to be used in conjunction with the uniformly

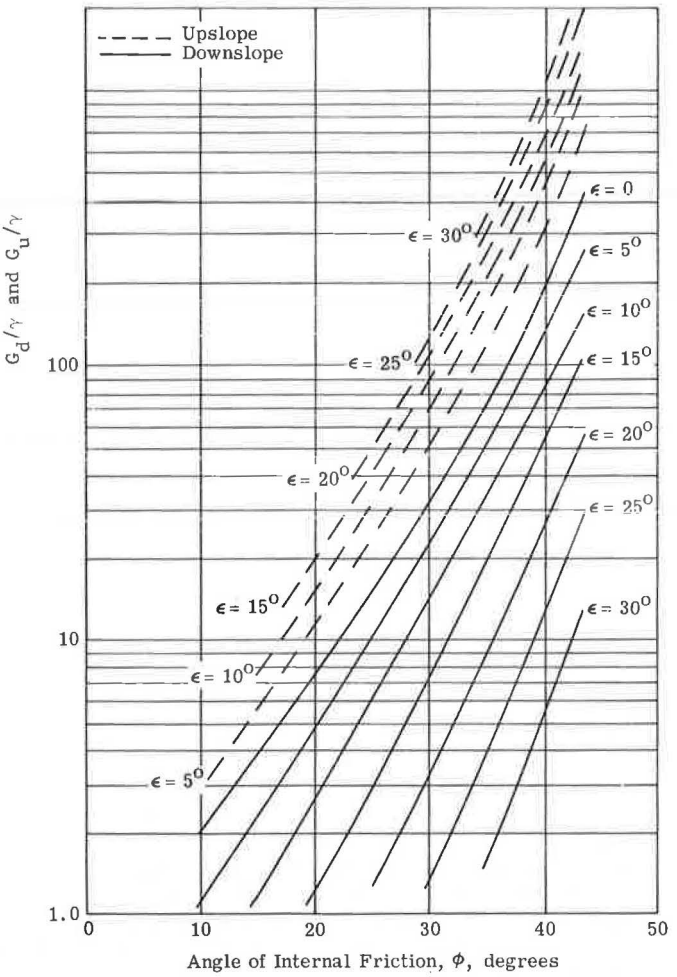

Figure 7. Stress gradients for vertical loading and for slopes varying from $\epsilon = 0$ to $\epsilon = 30$ deg.

distributed bearing stress resulting from the surcharge. Figure 6 shows the distribution of bearing stresses for such cases.

ANALYSIS BY NUMERICAL INTEGRATION METHODS

For the analysis of plastic equilibrium in slopes, the x-axis of the coordinate system is chosen to coincide with the surface of the slope, and the positive z-axis is set perpendicular and downward from it. The differential equations of the slip lines in this coordinate system (4) are

$$dz = dx \tan(\theta \pm \mu)$$
$$d\sigma \pm 2\sigma \tan\varphi d\theta = \frac{\gamma}{\cos\varphi}\left[\sin(\epsilon \pm \varphi)\, dx + \cos(\epsilon \pm \varphi)\, dr\right] \quad (15)$$

The upper sign refers to the family of the slip lines corresponding to the first, and the lower sign corresponds to the second characteristics of the differential equations.

For numerical computations, these differential equations are replaced by the following finite difference equations:

$$x_{i,j} = \frac{z_{i-1,j} - z_{i,j-1} + \alpha_1 x_{i,j-1} - \alpha_2 x_{i-1,j}}{\alpha_1 - \alpha_2}$$

$$z_{i,j} = z_{i-1,j} + \alpha_2 (x_{i,j} - x_{i-1,j})$$

$$\sigma_{i,j} = \frac{\gamma(C\sigma_{i,j-1} + D\sigma_{i-1,j}) + 2\sigma_{i,j-1}\sigma_{i-1,j}\left[1 + (\theta_{i,j-1} - \theta_{i-1,j}) \tan\varphi\right]}{\sigma_{i,j-1} + \sigma_{i-1,j}} \quad (16)$$

$$\theta_{i,j} = \frac{\sigma_{i,j-1} - \sigma_{i-1,j} + 2 \tan\varphi(\sigma_{i,j-1}\theta_{i,j-1} + \sigma_{i-1,j}\theta_{i-1,j}) + \gamma(D - C)}{2 \tan\varphi(\sigma_{i,j-1} + \sigma_{i-1,j})}$$

where

$x_{i,j}$, $z_{i,j}$ = coordinates of the subscripted modal point (Fig. 8),

$\alpha_1 = \tan(\theta_{i,j-1} + \mu)$,

$\alpha_2 = \tan(\theta_{i-1,j} - \mu)$,

$$C = \frac{\sin(\epsilon - \varphi)}{\cos\varphi}(x_{i,j} - x_{i-1,j}) + \frac{\cos(\epsilon - \varphi)}{\cos\varphi}(z_{i,j} - z_{i-1,j}), \text{ and}$$

$$D = \frac{\sin(\epsilon + \varphi)}{\cos\varphi}(x_{i,j} - x_{i-1,j}) + \frac{\cos(\epsilon + \varphi)}{\cos\varphi}(z_{i,j} - z_{i-1,j}).$$

These difference equations permit the computation of the coordinates of a nodal point (intersection of slip lines), as well as the values of σ and θ at that point, from the known values at neighboring nodal points having lesser subscripts.

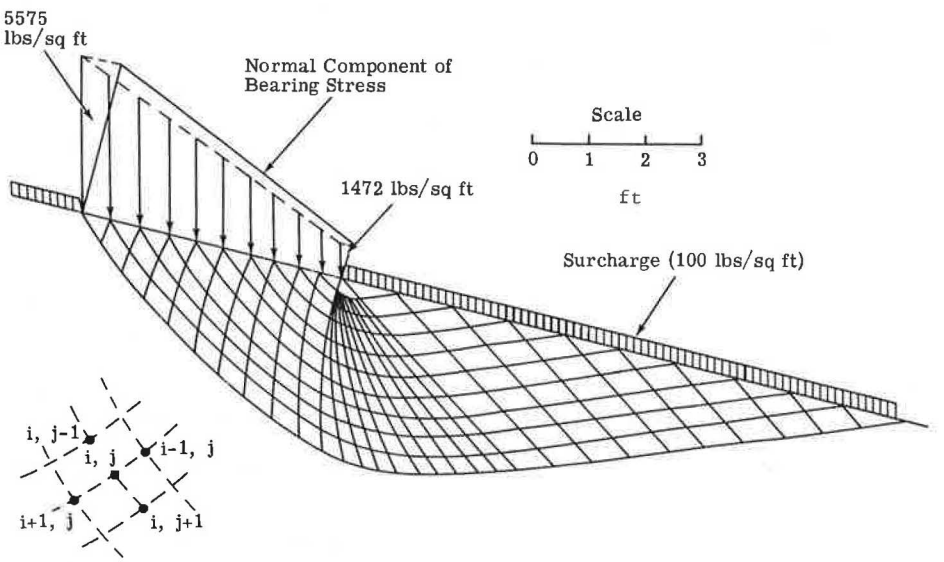

Figure 8. Slip-line field for φ = 35 deg, γ = 100 lb/cu ft, ϵ = 15 deg, p = 100 lb/sq ft determined by numerical integration.

The slip-line field in the passive zone can be computed by equations starting with the boundary values given at the surface of the slope. In the radial shear zone, the same equations are used, but special consideration is given to the central point where the second family of slip lines converge. This point is a degenerated slip line, where θ changes from the value at the passive zone boundary to that specified at the active zone boundary. The total change in θ is divided by the number of slip lines converging at this point to result in an equal $\Delta\theta$ increment between two adjacent slip lines. The σ values for each increment are computed from the equation $\sigma = \sigma_o e^{2(\theta-\theta_o)\tan\varphi}$, which is the solution of the differential equations of Eqs. 15 if both dx and dz vanish. With these θ and σ values assigned to each slip line at this point, the coordinates as well as the σ and θ values for all other points in the radial shear zone can be computed by Eqs. 16. In the active zone the same equations are used except for the points at the loaded surface where z = 0 and θ is given. Here x and σ are computed from

$$x_{i,j} = \left(z_{i,j} - z_{i-1,j}\right) \cot\left(\theta_{i-1,j} - \mu\right) + x_{i-1,j}$$

$$\sigma_{i,j} = 2\sigma_{i-1,j}\left(\theta_{i,j} - \theta_{i-1,j}\right) \tan\varphi + \gamma C + \sigma_{i-1,j}$$

The numerical computations were programmed for a GE Mark II computer. An example of the computed slip-line field is shown in Figure 8 for γ = 100 lb/cu ft, φ = 35 deg, ϵ = 15 deg, and p_o = 100 lb/sq ft. The stress at the upslope edge of the loading is less than the bearing stress at this point for upslope failure resulting from the surcharge; therefore, no upslope slip-line field develops.

Note that the slip-line fields representing the solution of the differential Eqs. 15 are geometrically similar only if the ratio

$$R = \frac{P}{\gamma \ell} \tag{17}$$

is the same (where ℓ = any length characteristic of the field, e.g., width of loaded area). Therefore, if the width of the loaded area is given, the slip-line field will change with the magnitude of the surcharge. For weightless soil, R = ∞ and the slip-line field assumed in the preceding section is valid; for no surcharge, R = 0. The stress gradients determined from the bearing stresses obtained with the numerical solution will also vary with the surcharge. Therefore, the stress gradients computed by the approximate method are not immediately comparable with those computed by the numerical method.

For the case of no surcharge, the numerical method described does not apply because of the nature of the singularity at point A. To obtain a stress gradient closely approximating the surface loading, computer runs were made for a small p of 100 lb/sq ft surcharge. A comparison of stress gradients obtained by the approximate and numerical methods is given in Table 1. Further investigations are planned to determine whether improvements in the numerical procedure (such as using an average value of θ between point i, j and either i-1, j or i, j-1) or other iteration procedures would appreciably affect the value of the computed stress gradients.

TABLE 1

COMPARISON OF STRESS GRADIENTS DETERMINED BY THE APPROXIMATE AND NUMERICAL METHOD

φ (deg)	ϵ = 0		Downslope Gradient (ϵ = 15 deg)	
	Approximate Method (R = ∞)	Numerical Method (R = 0.1)	Approximate Method (R = ∞)	Numerical Method (R = 0.2)
20	7.6	3.4	1.1	0.5
25	15.1	6.8	3.1	1.5
30	31.2	14.8	7.3	3.9
35	68.7	36.0	16.8	9.1
40	164.5	71.0	40.6	20.5
45	443.6	166.0	106.0	50.1

RESULTS OF EXPERIMENTS

A series of load tests was performed with circular plates on sand from Jones Beach. The grain size distribution of this sand is shown in Figure 9, and Figure 10 shows the results of triaxial tests run in

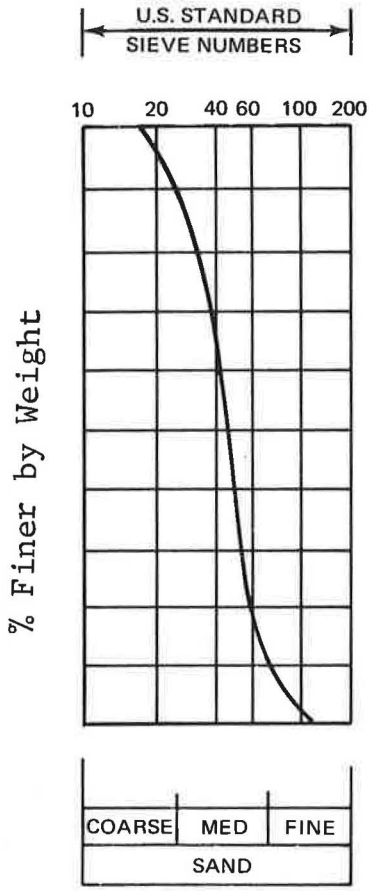

Figure 9. Grain size distribution of Jones Beach sand.

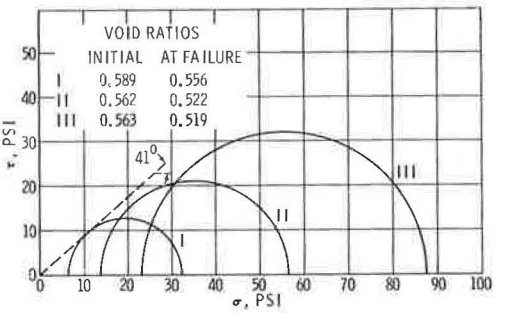

Figure 10. Results of triaxial tests on Jones Beach sand.

an air-dry condition. The volume changes were determined from vertical and circumferential deformation. The sand bed was prepared by using a movable hopper with a rotating distributor cylinder that deposited the sand at densities from 102.5 to 104 lb/cu ft; higher densities were obtained by vibrating the individual layers.

Preliminary tests showed that slanting an originally horizontal box did not result in the stress conditions desired, even if the side walls were lubricated. It was found satisfactory, however, to deposit the material in sloping layers, and this method was adopted for the tests. The vertical load was transmitted to the circular disk through a steel ball seated in an indented seat located so that the vertical load passed through the center of the bottom surface of the disk. With this arrangement little vertical rotation of the disk occurred during penetration.

Typical load-penetration curves of a 2-in. diameter disk for both level and sloping ground are shown in Figure 11. The results of a series of tests performed with 1-, 1½-, and 2-in. disks on both level and 15-deg sloping beds of Jones Beach sand are given in Table 2. The ultimate loads (q_{ua}) were determined from the test results on the basis of tangency with $dq/dz = \gamma N_q$. The theoretical ultimate loads (q_{ut}) were determined using the stress gradient method described previously for the N_γ contribution and the actual depth of penetration at q_{ua} for the N_q fraction. The range of friction angle φ in Table 2 corresponds to those q_{ut} that bracket the experimentally obtained q_{ua}.

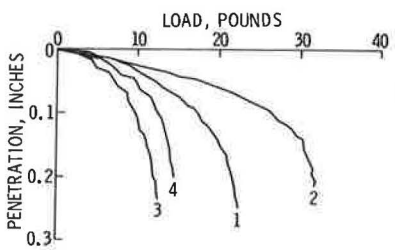

PLATE DIAMETER: 2 INCH

NO.	DENSITY (PCF)	SLOPE (DEGREES)
1	104.6	0
2	107.8	0
3	103.2	15
4	107.2	15

Figure 11. Results of small-scale tests.

TABLE 2

SUMMARY OF EXPERIMENTAL AND THEORETICAL RESULTS FOR ULTIMATE LOADS UNDER VARIOUS SIZED DISKS ON LEVEL AND SLOPING GROUND

Disk Diameter (in.)	ϵ = 0 deg				ϵ = 15 deg			
	γ (lb/cu ft)	q_{ua} (lb/sq in.)	q_{ut} (lb/sq in.)	φ (deg)	γ (lb/cu ft)	q_{ua} (lb/sq in.)	q_{ut} (lb/sq in.)	φ (deg)
1	104	3.38	3.08-3.71	42-43	103.6	1.43	1.27-1.52	42-43
	106.5	4.7	4.34-5.44	44-45	106.5	2.36	2.38	45
1½	102.5	4.7	4.33-5.22	42-43	102.5	3.32	3.31	45
	108.0	9.7	7.84-9.72	45-46	107.6	5.16	4.24-5.19	46-47
2	104.6	6.62	5.84-7.04	42-43	103.2	3.47	2.99-3.61	43-44
	107.8	10.0	8.92-10.96	44-45	107.2	4.14	3.66-4.47	44-45

A comparison of the back-computed friction angles φ for both the level (ϵ = 0) and sloped (ϵ = 15 deg) case indicates close correspondence. The fact that both computed values are slightly ($\approx$ 10 percent) larger than the value obtained from the triaxial data suggests a dependence of φ on strain conditions. The implications of using modified φ angles in bearing capacity formulas have been considered by others (5). The important point here is that the consistency in the back-computed friction angle φ between the level and sloped cases ensures the validity of the relative values of bearing strength between the two cases. As given in Table 2, with increase in slope there is in every case a substantial decrease in both the measured (q_{ua}) and predicted (q_{ut}) values for the ultimate bearing capacity.

CONCLUSIONS

In frictional soils where pore pressures are negligible, failure occurs in shear zones. For such soils the stability of slopes loaded over a finite area can be analyzed by bearing capacity methods. An approximate method has been developed assuming slip-line fields analogous to the Prandtl solution for horizontal ground. A formula for N_q for various slope angles and inclination of loads is given. In the case of slopes it is more convenient to express the effect of weight in terms of stress gradients, representing the rate of increase of bearing stresses from the edge of the loaded area, than by the N_q factor. Results of experiments performed on sand with small-diameter disks show that the bearing capacity on slopes can be reasonably well predicted by the approximate method.

REFERENCES

1. Meyerhof, G. G. The Ultimate Bearing Capacity of Foundations on Slopes. Proc. Fourth Internat. Conf. on Soil Mech. and Found. Engineering, Vol. 1, London, 1957.
2. Sokolovski, V. V. Statics of Soil Media. Butterworth and Co. Ltd., London, 1960.
3. Karafiath, L. L., and Nowatzki, E. A. A Study of the Effect of Sloping Ground on Bearing Strength and the Landing Performance of Space Vehicles. Grumman Aerospace Corp., Research Dept. Memo. RM-407, March 1968.
4. Harr, M. E. Foundations of Theoretical Soil Mechanics. McGraw-Hill, New York, 1966.
5. De Beer, E. E. Bearing Capacity and Settlement of Shallow Foundations on Sand. Proc. Symposium on Bearing Capacity and Settlement of Foundations, Duke Univ., Durham, N.C., 1967.

Appendix

NOTATION

The following symbols are used in this paper:

b = width of loading;
c = cohesion;
N_q, N_γ, N_c = bearing capacity factors;
p = surcharge;
q_u = ultimate unit load;
γ = unit weight;
σ = inclination of load measured from the vertical;
ϵ = slope angle;
θ = angle between x-axis and major principal stress;
λ = inclination of reduced surcharge measured from the vertical;
$\mu = \pi/4 - \varphi/2$;
$\sigma = (\sigma_z + \sigma_x)/2 + \psi$
φ = friction angle; and
$\psi = c \cot \varphi$.

Application of Plasticity Theory to Slope Stability Problems

H. Y. FANG and T. J. HIRST, Fritz Engineering Laboratory, Lehigh University

The purpose of this paper is to present a closed-form plasticity solution to slope stability problems in homogeneous soils. The paper discusses the basic concepts and limitations of the plasticity solution by comparing it to existing limit equilibrium solutions. Stability factors computed by the plasticity technique assuming straight-line, circular, and logarithmic-spiral failure surfaces are presented. These are compared with stability factors computed from existing limit equilibrium solutions including the Culmann method, the friction circle method, and the Rendulic logarithmic-spiral method. Design charts developed from the plasticity solution are presented for a useful range of friction angles and slope geometries.

•THERE ARE numerous methods currently available for performing slope stability analyses. The majority of these may be categorized as limit equilibrium methods. The basic assumption of the limit equilibrium approach is that Coulomb's failure criterion is satisfied along the failure surface. The failure surface may be assumed to be a straight line, circular arc, logarithmic spiral, or other irregular surface. Analytical, graphical, semigraphical, and numerical procedures for solving limit equilibrium problems are available.

A weakness of the limit equilibrium approach is that it neglects the soil's stress-strain relationship. From the mechanics of solids point of view, a valid solution is obtained if equilibrium, compatibility, and the material's stress-strain relationship are simultaneously satisfied. The limit equilibrium method considers only equilibrium.

In an attempt to take account of the stress-strain relationship in analyzing the stability of slopes, it has been suggested that the theory of plasticity be applied to the problem (8). The purpose of this paper is to utilize plasticity theory to solve homogeneous earth slope stability problems, and to compare the results with conventional limit equilibrium solutions. The results are presented in the form of a design chart of stability factors computed for a useful range of friction angles and slope geometries.

LIMIT EQUILIBRIUM METHOD

The Culmann method (7) represents a typical limit equilbrium solution and is briefly reviewed here for purposes of illustration and comparison. The method assumes that failure occurs on a plane (straight line) passing through the toe of the earth slope. The Culmann failure mechanism is shown in Figure 1, where W is the weight of soil in the wedge ABD, C is the total cohesion along the failure plane AB, and α, β, and θ are the slope angles. P is the resultant force necessary to hold wedge ABD in equilibrium, H is the height of the earth slope, and ϕ is the friction angle for the soil. From the geometrical relationships shown in Figure 1, the weight of soil in the wedge ABD is

$$W = \frac{1}{2} \gamma l H \csc \beta \sin (\beta - \theta) \qquad (1)$$

where γ is the unit weight of the soil and l is the length of the failure plane AB. If c

Paper sponsored by Committee on Embankments and Earth Slopes.

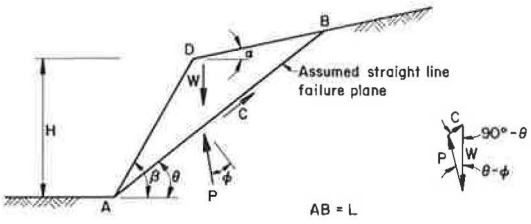

Figure 1. Straight-line limit equilibrium failure plane (Culmann method).

is the unit cohesion, then

$$C = cl \tag{2}$$

Substitution of Eqs. 1 and 2 into the law of sines expressed for the force diagram in Figure 1 yields

$$\frac{\gamma H}{c} = \frac{2 \sin \beta \cos \phi}{\sin (\beta - \theta) \sin (\theta - \phi)} \tag{3}$$

The term $\gamma H/c$ is a dimensionless expression called the stability factor, N_s. The critical stability factor (most dangerous plane) may be obtained by minimizing the first derivative of the stability factor with respect to θ. This yields

$$N_{s_{crit.}} = \frac{4 \sin \beta \cos \phi}{1 - \cos (\beta - \phi)} \tag{4}$$

For a vertical cut where $\beta = 90 \text{ deg} = \frac{\pi}{2}$, Eq. 4 becomes

$$N_{s_{crit.}} = 4 \tan \left(\frac{\pi}{4} + \frac{\phi}{2} \right) \tag{5}$$

The critical height of the slope, H_c, is

$$H_c = N_{s_{crit.}} \frac{c}{\gamma} = \frac{4c}{\gamma} \tan \left(\frac{\pi}{4} + \frac{\phi}{2} \right) \tag{6}$$

The Culmann method has been widely used for slope stability analyses because of its simplicity, even though the assumptions on which the method is based are of questionable validity.

Extensive refinements of the limit equilibrium method have been undertaken by many investigators. These refinements have generally been concerned with defining a more acceptable failure surface or with modifying the method by which the forces acting on the failure surface are handled. A summary of the various limit equilibrium methods currently in use is given in Table 1.

The foregoing description of limit equilibrium methods is intended to provide a background for, and to distinguish these methods from, the plasticity method. Thus only the basic features of the methods have been introduced. The results obtained by the various methods will be compared with plasticity solutions later in the paper.

PLASTICITY ANALYSES

Plasticity analyses are based on two main theorems for any body or assemblage of bodies of elastic-perfectly plastic material:

1. Lower Bound Theorem—If an equilibrium distribution of stress can be found that balances the applied load and nowhere violates the yield criterion that includes c, the cohesion, and ϕ, the angle of internal friction, the soil mass will not fail or will be just at the point of failure.
2. Upper Bound Theorem—The soil mass will collapse if there is any compatible pattern of plastic deformation for which the rate of work of the external loads exceeds the rate of internal energy dissipation.

According to the upper bound theorem, it is necessary to find a compatible failure mechanism (velocity field) in order to obtain an upper bound solution. A stress field satisfying all conditions of the lower bound theorem is required for a lower bound

TABLE 1

CLASSIFICATION OF SLOPE STABILITY ANALYSIS BY LIMIT EQUILIBRIUM METHOD

Type of Failure Plane	Name of Method	Type of Solution	Basic Assumptions	References
Straight line	Culmann method	Analytical	Failure occurs on a plane through the toe of the slope	Culmann (7)
	Method of infinite slope[a]	Analytical	The slope is constant with unlimited extent A vertical column is typical of the entire mass No cohesion may be depended on within the depth to which tension occurs	Résal (20) Frontard (11)
	Wedge method	Semigraphical, analytical	Sliding block mechanism is assumed with lateral earth forces	Culmann (7), Terzaghi and Peck (23)
Circular arc[a]	Slices method[b]	Semigraphical, numerical	The lateral forces are equal on two sides of each slice	Statens Jarnvagars Geotekniska Commission, Fellenius (10)
	Bishop's method[b]	Analytical, numerical	Oblique side forces on each slice are considered	Bishop (2)
	Simplified Bishop's method[b]	Analytical, numerical	Vertical component of lateral earth forces are considered to be equal and opposite	Bishop (2), Little and Price (14)
	ϕ-circle method[b]	Analytical, graphical	Resultant acting on rupture arc is tangential to a concentric circle with radius = R sin ϕ_d	Gilboy (12), Taylor (22), Casagrande (3)
	Modified ϕ-circle[b]	Analytical, graphical	The resultant misses tangency to the ϕ_d circle by a small amount; radius of ϕ_d circle = KR sin ϕ_d	Taylor (22)
Logarithmic spiral	Log-spiral method	Analytical	No assumptions required to make the problem statically determinate	Rendulic (19), Taylor (22), Spencer (21)
Irregular	Irregular	Analytical, numerical	General slip surface Forces between slices are considered	Morgenstern and Price (15)

[a]Circular arc failure plane, suggested by Petterson and Hultin (16).

[b]Long-term stability analysis (seepage considered).

solution. If the upper bound and lower bound provided by the velocity field and stress field coincide, the exact value of the collapse load is determined (for an elastic-perfectly plastic material). The following section gives examples demonstrating the application of plasticity theorems to problems of earth slope stability.

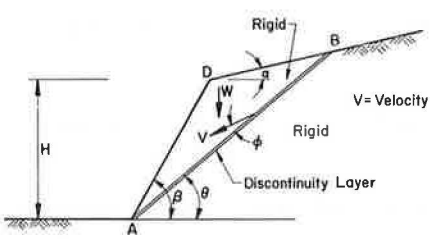

Figure 2. Straight-line plasticity failure mechanism—velocity field (upper bound solution).

Straight-Line Failure Plane

A plasticity analysis of the slope stability problem was first performed by Drucker and Prager (8). They assumed a straight-line failure plane and suggested the upper bound failure mechanism shown in Figure 2. The symbols are as previously defined. As the wedge formed by the shear plane slides downward along the discontinuity surface, the rate of work done by the external forces is equal to the vertical component of the velocity multiplied by the weight of the soil wedge. For a vertical cut (β = 90 deg) and horizontal backfill (α = 0 deg), the rate of external work is

$$\text{Rate of Work}_{\text{ext.}} = \frac{1}{2}\gamma H^2 V \cot\theta \sin(\theta - \phi) \tag{7}$$

where V equals the velocity of the wedge and is inclined at angle ϕ to the discontinuity surface. The rate of internal energy dissipation along the discontinuity surface is

$$\text{Rate of Work}_{\text{int.}} = \frac{cH}{\sin\theta} V \cos\phi \tag{8}$$

Equating the rate of external work (Eq. 7) to the rate of internal energy dissipation (Eq. 8) gives

$$H \leq \frac{2c}{\gamma} \frac{\cos\phi}{\sin(\theta - \phi)\cos\theta} \tag{9}$$

Minimizing the right side of Eq. 9 gives

$$\theta = \frac{\pi}{4} + \frac{\phi}{2} \tag{10}$$

and

$$H_c \leq \frac{4c}{\gamma} \tan\left(\frac{\pi}{4} + \frac{\phi}{2}\right) \tag{11}$$

Thus it may be seen that the upper bound plasticity solution for the critical height, H_c, of a vertical cut yields the same value as the Culmann limit equilibrium solution.

A lower bound solution for a vertical cut was also developed by Drucker and Prager (8) and later refined by Chen and Scawthorn (4). The suggested stress field is composed of three regions, as shown in Figure 3a. Region I, in the bank itself, is subjected to uniaxial compression that increases with depth. Region II is under biaxial compression and region III is under hydrostatic pressure ($\sigma_x = \sigma_y$). Figure 3b shows the corresponding Mohr circles for each region. Failure occurs when the circle representing region I meets the yield curve. Therefore,

$$\frac{1}{2}\gamma H = c\cos\phi + \frac{1}{2}\gamma H \sin\phi \tag{12}$$

and

$$H_c \geq \frac{2c}{\gamma} \tan\left(\frac{\pi}{4} + \frac{\phi}{2}\right) \tag{13}$$

Hence, the lower bound solution is only half the value given by the upper bound solution.

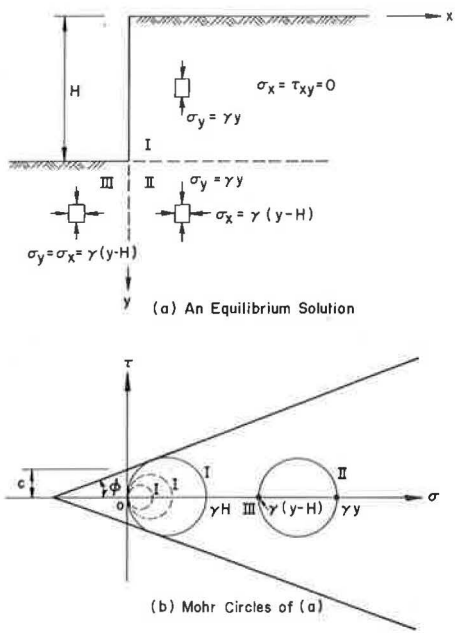

Figure 3. Plasticity stress field for a vertical cut (lower bound solution): (a) an equilibrium condition, and (b) Mohr circles of the equilibrium condition.

Logarithmic-Spiral Failure Plane

Model studies have indicated that the shape of the failure plane for earth slopes is frequently close to a logarithmic spiral (13). Drucker and Prager (8) have suggested that the upper bound solution could be improved by choosing a logarithmic spiral as the discontinuity surface rather than a straight line. Recently, a closed-form mathematical solution of the upper bound problem has been

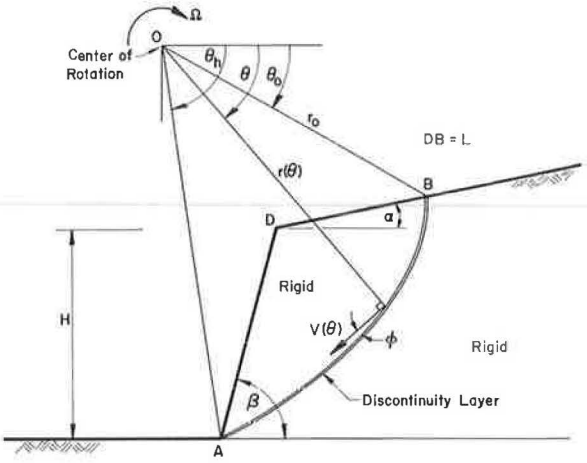

Figure 4. Logarithmic-spiral plasticity failure mechanism—velocity field (upper bound solution).

developed by Chen, Giger, and Fang (6). The assumed failure mechanism is shown in Figure 4. The triangular-shaped region ABD rotates as a rigid body about the center of rotation O, with the materials below the logarithmic surface AB remaining at rest. Thus, the surface AB is a surface of velocity discontinuity. The mechanism can be specified by three variables, θ_o, θ_h, and H, which are the slope angles of the chords OB and OA and the height of the embankment respectively. From the geometrical relations it may be shown that the ratios H/r_o and L/r_o can be expressed in terms of the angles θ_o and θ_h in the forms

$$\frac{H}{r_o} = \frac{\sin \beta}{\sin (\beta - \alpha)} \left\{ \sin (\theta_h + \alpha) \exp \left[(\theta_h - \theta_o) \tan \phi \right] - \sin (\theta_o + \alpha) \right\} \tag{14}$$

where r_o = radius of logarithmic spiral at $\theta = \theta_o$. Also, if L = length of the slope DB (Fig. 4), then

$$\frac{L}{r_o} = \frac{\sin (\theta_h - \theta_o)}{\sin (\theta_h + \alpha)} - \frac{\sin (\theta_h + \beta)}{\sin (\theta_h + \alpha) \sin (\beta - \alpha)} \left\{ \exp \left[(\theta_h - \theta_o) \tan \phi \right] \sin (\theta_h + \alpha) - \sin (\theta_o + \alpha) \right\} \tag{15}$$

The rate of external work may be obtained by the simple algebraic summation of the rates of work resulting from rotation of the soil weight in the regions OAB, OAD, and ODB:

$$\text{Rate of Work}_{ext.} = \gamma r_o^3 \, \Omega \, (f_1 - f_2 - f_3) \tag{16}$$

where Ω is the angular velocity of the region ABD and f_1, f_2, and f_3 are defined as

$$f_1 (\theta_h, \theta_o) = \frac{1}{3 (1 + 9 \tan^2 \phi)} \left\{ (3 \tan \phi \cos \theta_h + \sin \theta_h) \exp \left[3 (\theta_h - \theta_o) \tan \phi \right] - (3 \tan \phi \cos \theta_o + \sin \theta_o) \right\} \tag{17}$$

$$f_2(\theta_h, \theta_o) = \frac{1}{6}\frac{L}{r_o}\left(2\cos\theta_o - \frac{L}{r_o}\cos\alpha\right)\sin(\theta_o + \alpha) \tag{18}$$

$$f_3(\theta_h, \theta_o) = \frac{1}{6}\exp\left[(\theta_h - \theta_o)\tan\phi\right]\left[\sin(\theta_h - \theta_o) - \frac{L}{r_o}\sin(\theta_h + \alpha)\right]$$

$$\left\{\cos\theta_o - \frac{L}{r_o}\cos\alpha + \cos\theta_h \exp\left[(\theta_h - \theta_o)\tan\phi\right]\right\} \tag{19}$$

The rate of internal dissipation of energy occurs along the discontinuity surface AB and may be found by integration of the differential rate of dissipation of energy along the surface, over the whole surface. This is obtained by multiplying the differential area, rd $\theta/\cos\phi$, by the cohesion, c, times the tangential discontinuity in velocity, V cos ϕ, and integrating from θ_o to θ_h:

$$\text{Rate of Work}_{\text{int.}} = \int_{\theta_o}^{\theta_h} c(V\cos\phi)\frac{rd\,\theta}{\cos\phi}$$

$$= \frac{cr_o^2\,\Omega}{2\tan\phi}\left\{\exp\left[2(\theta_h - \theta_o)\tan\phi\right] - 1\right\} \tag{20}$$

Equating the external rate of work (Eq. 16) to the rate of internal energy dissipation (Eq. 20) yields

$$H = \frac{c}{\gamma} f(\theta_h, \theta_o) \tag{21}$$

where $f(\theta_h, \theta_o)$ is defined as

$$f(\theta_h, \theta_o) = \frac{\sin\beta\left\{\exp\left[2(\theta_h - \theta_o)\tan\phi\right] - 1\right\}}{2\sin(\beta - \alpha)\tan\phi\,(f_1 - f_2 - f_3)}$$

$$\left\{\sin(\theta_h + \alpha)\exp\left[(\theta_h - \theta_o)\tan\phi\right] - \sin(\theta_o + \alpha)\right\} \tag{22}$$

By the upper bound theorem, Eq. 21 gives a least upper bound solution for H when $f(\theta_h, \theta_o)$ is a minimum. Such a condition is attained when

$$\frac{\delta f}{\delta\theta_h} = 0 \text{ and } \frac{\delta f}{\delta\theta_o} = 0 \tag{23}$$

Solving these equations and substituting the resulting values of θ_h and θ_o into Eq. 21 yields the critical height, H_c, of an earth slope

$$H_c \leq \frac{c}{\gamma} N_s \tag{24}$$

where

$$N_s = \text{min. } f(\theta_h, \theta_o) \tag{25}$$

The value N_s depends on the slope angles, α and β, and the angle of internal friction, ϕ.

The results of this analysis are shown in Figures 5 and 6 for the special cases $\alpha = 0$ or $\beta = 90$ deg and are tabulated numerically in Table 2 for the more general cases.

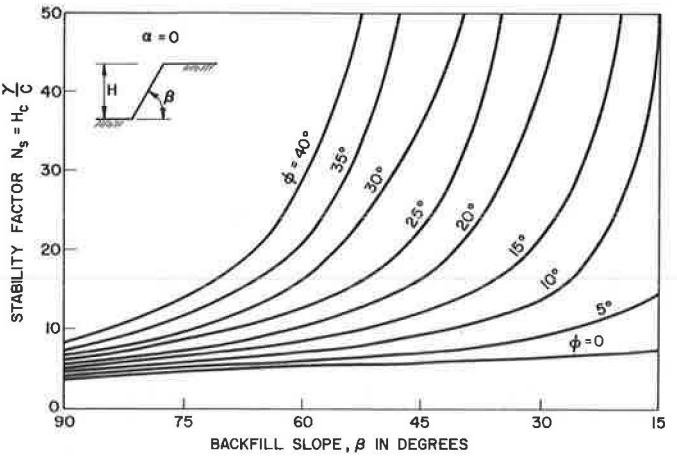

Figure 5. Stability factor versus slope angle, β, for various friction angles.

TABLE 2

SUMMARY OF STABILITY FACTORS, N_S, COMPUTED BY PLASTICITY THEORY (UPPER BOUND)

Friction Angle, ϕ (deg)	Slope Angle, α (deg)	Slope Angle, β (deg)					
		90	75	60	45	30	15
0	0	3.83	4.57	5.25	5.86	6.51	7.35
5	0	4.19	5.14	6.17	7.33	9.17	14.80
	5	4.14	5.05	6.03	7.18	8.93	14.62
10	0	4.59	5.80	7.26	9.32	13.53	45.53
	5	4.53	5.72	7.14	9.14	13.26	45.15
	10	4.47	5.61	6.98	8.93	12.97	44.56
15	0	5.02	6.57	8.64	12.05	21.71	
	5	4.97	6.49	8.52	11.91	21.50	
	10	4.90	6.39	8.38	11.73	21.14	
	15	4.83	6.28	8.18	11.42	20.59	
20	0	5.51	7.48	10.39	16.18	41.27	
	5	5.46	7.40	10.30	16.04	41.06	
	10	5.40	7.31	10.15	15.87	40.73	
	15	5.33	7.20	9.98	15.59	40.16	
	20	5.24	7.04	9.78	15.17	39.19	
25	0	6.06	8.59	12.75	22.92	120.0	
	5	6.01	8.52	12.65	22.78	119.8	
	10	5.96	8.41	12.54	22.60	119.5	
	15	5.89	8.30	12.40	22.37	118.7	
	20	5.81	8.16	12.17	21.98	117.4	
	25	5.71	7.97	11.80	21.35	115.5	
30	0	6.69	9.96	16.11	35.63		
	5	6.63	9.87	16.00	35.44		
	10	6.58	9.79	15.87	35.25		
	15	6.53	9.67	15.69	34.99		
	20	6.44	9.54	15.48	34.64		
	25	6.34	9.37	15.21	34.12		
	30	6.22	9.15	14.81	33.08		
35	0	7.43	11.68	20.94	65.53		
	5	7.38	11.60	20.84	65.39		
	10	7.32	11.51	20.71	65.22		
	15	7.26	11.41	20.55	65.03		
	20	7.18	11.28	20.36	64.74		
	25	7.11	11.12	20.07	64.18		
	30	6.99	10.93	19.73	63.00		
	35	6.84	10.66	19.21	60.80		
40	0	8.30	14.00	28.99	185.6		
	5	8.26	13.94	28.84	185.5		
	10	8.21	13.85	28.69	185.3		
	15	8.15	13.72	28.54	185.0		
	20	8.06	13.57	28.39	184.6		
	25	7.98	13.42	28.16	184.0		
	30	7.87	13.21	27.88	183.2		
	35	7.76	12.95	27.49	182.3		
	40	7.61	12.63	26.91	181.1		

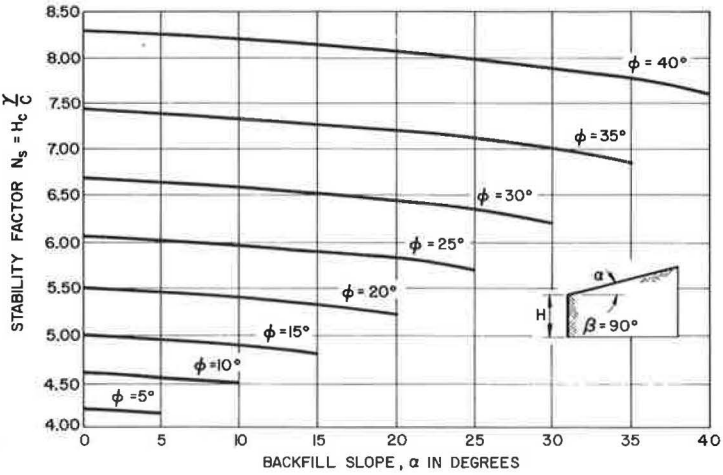

Figure 6. Stability factor versus slope angle, α, for various friction angles.

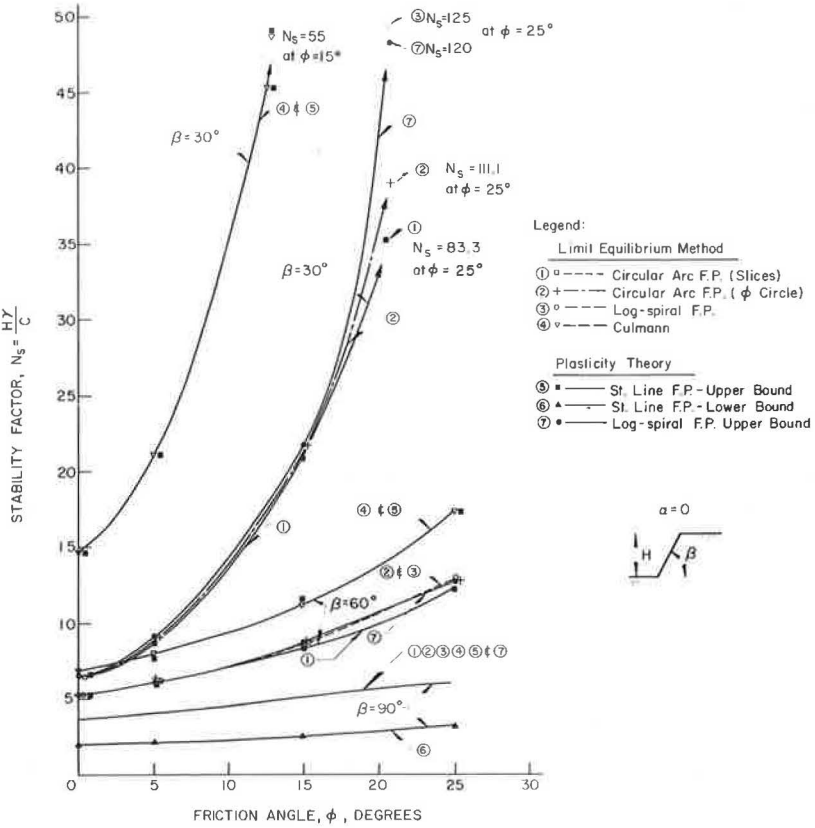

Figure 7. Comparison of stability factor values computed by various methods for β of 30, 60, and 90 deg.

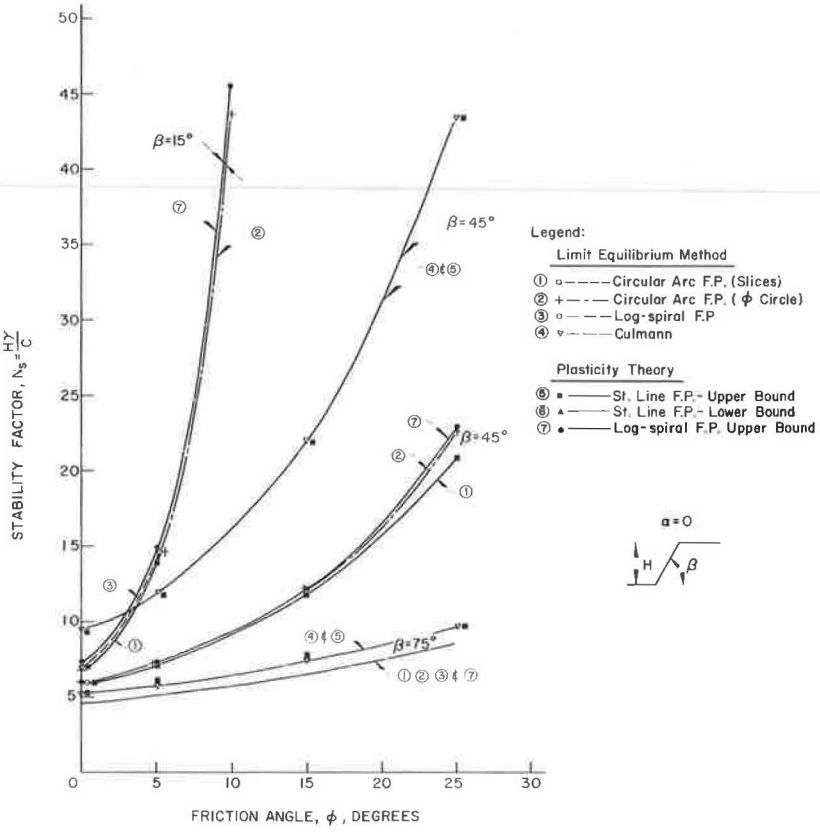

Figure 8. Comparison of stability factor values computed by various methods for β of 15, 45, and 75 deg.

COMPARISON OF LIMIT EQUILIBRIUM AND PLASTICITY RESULTS

Figures 7 and 8 show the stability factor, N_S, versus friction angle, ϕ, for various angles, β, with angle α constant and equal to zero. Both limit equilibrium and plasticity solutions are shown.

It may be noted that in the case of steep embankments, limit equilibrium methods and upper bound plasticity methods yield similar results. The discrepancies between the various methods increase with increasing friction angle and with decreasing slope angle, β.

SUMMARY AND CONCLUSIONS

Additional insight into many soil mechanics problems such as bearing capacity (17), earth pressure (1, 18), and slope stability (8) may be obtained by considering soil as a perfectly plastic material. The limitations of plasticity theory applied to soil mechanics problems have been discussed by Drucker (9) and more recently by Chen (5).

In applying plasticity theory to problems of earth slope stability, the following conclusions may be considered applicable within the limitations of the assumptions used:

1. For a straight-line failure plane, both limit equilibrium and upper bound plasticity methods yield the same results, suggesting that the conventional limit equilibrium method provides an upper bound solution.

2. For a logarithmic-spiral failure plane, the upper bound plasticity method provides a closed-form mathematical solution. Currently, only numerical procedures are available for solving the limit equilibrium equations. The results of the upper bound plasticity solution are presented in the form of a design chart giving stability factors for a wide range of soil properties and slope geometries (Table 2).

3. The most significant advantage to using the plasticity method in analyzing the stability of earth slopes is that the upper and lower bound theorems provide a mechanism for bounding the solution. On the other hand, limit equilibrium methods do not provide any indication of their own validity. This is not meant to imply that stability analyses should be performed solely by plasticity methods. Soil is not a perfectly plastic material although it does exhibit certain plastic characteristics. What the upper and lower bound theorems do provide are additional guidelines to aid the designer in establishing a rational factor of safety for the problem under consideration.

ACKNOWLEDGMENTS

The work described in this paper was conducted in the Geotechnical Engineering Division, Fritz Engineering Laboratory, Lehigh University, as part of the research program on soil plasticity. This particular study is sponsored by the Envirotronics Corporation.

The authors express their appreciation to Professor W. F. Chen for his constructive criticism and review of the manuscript.

REFERENCES

1. Bell, A. L. The Lateral Pressure and Resistance of Clay, and the Supporting Power of Clay Foundations. Minutes of Proc. of Institution of Civil Engineers, Paper No. 4131, London, 1915.
2. Bishop, A. W. The Use of the Slip Circle in the Stability Analysis of Slopes. Geotechnique, Vol. 5, 1955, pp. 7-17.
3. Casagrande, A. The Shearing Resistance of Soils. Jour. Boston Society of Civil Engineers, Vol. 21, No. 3, 1934.
4. Chen, W. F., and Scawthorn, C. R. Limit Analysis and Limit Equilibrium Solutions in Soil Mechanics. Lehigh Univ., Bethlehem, Penn., Fritz Engineering Lab. Rept. 355.3, 1968.
5. Chen, W. F. Soil Mechanics and the Theorems of Limit Analysis. Jour. Soil Mech. and Found. Div., ASCE, Vol. 95, No. SM2, 1969.
6. Chen, W. F., Giger, M. W., and Fang, H. Y. On the Limit Analysis of Stability of Slopes. Soils and Foundations, Vol. 9, No. 4, Dec. 1969.
7. Culmann, K. Die Graphische Stalik. Berlin, 1866.
8. Drucker, D. C., and Prager, W. Soil Mechanics and Plastic or Limit Design. Quarterly of Applied Mathematics, Vol. 10, 1952, pp. 157-165.
9. Drucker, D. C. Limit Analysis of Two and Three Dimensional Soil Mechanics Problems. Jour. Mechanics and Physics of Solids, Vol. 1, No. 4, 1953, pp. 217-226.
10. Fellenius, W. Erdstatische Berechnungen (Calculation of Stability of Slopes), Revised Edition. W. Ernst und Sohn, Berlin, 1939.
11. Frontard, M. Cycloides de Glissement des Terres. Comptes Rendues, Paris, 1922.
12. Gilboy, G. Soil Mechanics Research. Trans. ASCE, Vol. 98, 1933.
13. Jumikis, A. R. Stability Analysis of Soil-Foundation Systems: A Design Manual. Rutgers, The State University, Engineering Research Publ. No. 44, 1965.
14. Little, A. L., and Price, V. E. The Use of an Electronic Computer for Slope Stability Analysis. Geotechnique, Vol. 8, 1958, pp. 113-120.
15. Morgenstern, N. R., and Price, V. E. The Analysis of the Stability of General Slip Surfaces. Geotechnique, Vol. 15, 1965, pp. 79-93.
16. Petterson, K. E., and Hultin, S. Kajraseti Göteborg des 5 re Mars 1916. Teknisk Tidskrift, Vol. 46, 1916, pp. 281-294.

17. Prandtl, L. Ueber die Harte plastischer Körper. Nachrichten von der Königlichen Gesellschaft der Wissenschaften zu Göttingen, Berlin, 1920, pp. 74-85.
18. Rankine, W. J. M. A Manual of Applied Mechanics. Charles Griffin and Co., London, 1885, pp. 219-220.
19. Rendulic, L. Ein Beitrag zur Bestimmung der Gleitsicherheit. Der Bauingenieur, No. 19/20, 1935.
20. Résal, J. Poussée des Terres. Paris, 1910.
21. Spencer, E. Circular and Logarithmic Spiral Slip Surfaces. Jour. Soil Mech. and Found. Div., ASCE, Vol. 95, No. SM1, 1969, pp. 227-234.
22. Taylor, D. W. Stability of Earth Slopes. Jour. Boston Society of Civil Engineers, Vol. 24, 1937, pp. 197-246.
23. Terzaghi, K., and Peck, R. B. Soil Mechanics in Engineering Practice. John Wiley and Sons, 1948.

Discussion

LESLIE L. KARAFIATH, Grumman Aerospace Corporation—The application of plasticity theory to slope stability problems requires the finding of solutions for the basic differential equations of plastic equilibrium. These equations combine the differential equations of static equilibrium with the Mohr-Coulomb failure criterion characterized by the effective strength parameters c and ϕ; the development of the differential equations in a form suitable for numerical integration is due to Sokolovski. The solution of these equations is a family of slip lines that form zones of plastic equilibrium; each point within these zones is in failure condition. The mode of failure of granular materials that follow that Mohr-Coulomb criterion is, indeed, zone failure, as earth pressure experiments and sand amply demonstrate.

The strength properties of soils that generate pore pressures may be described by the undrained strength parameters c_u and ϕ_u. Formal solutions of the differential equations of plasticity can be obtained by substituting these parameters in the Mohr-Coulomb failure criterion. These solutions, however, are invalid in the physical sense, because the inclination of the slip lines to the direction of principal stresses is 45 deg $\pm$ $\phi_u/2$ in the formal solutions, whereas theory and experiments equally indicate that the inclination of the failure surface is governed by the effective angle of friction and its angle is 45 deg $\pm$ $\phi/2$. Thus plasticity theory does not apply to cases where the use of undrained strength parameters is appropriate; indeed, the soil in such cases fails along a narrow band that may be called a single failure surface. The development of such a single failure surface is often the result of pore water migration toward the most stressed portion of the soil mass and other progressive failure phenomena. This process will be discussed in more detail elsewhere.

The authors do not present zone solutions for the basic differential equations of plastic equilibrium but assume a surface of "velocity discontinuity" in their analyses and apply the limit theorems of plasticity theory to determine upper bounds for the height of a stable slope. The assumption of a discontinuity surface is essentially equivalent to assuming a single failure surface in the conventional ("limit equilibrium" in the authors' terminology) methods; it is a reasonable assumption for short-term slope stability problems controlled by the undrained shear strength of soil. By skillful selection of the variables, the authors arrive at an expression for the stable slope height (Eq. 21) that is amenable to minimizing; the authors call the minimum value of the stable slope height "least upper bound." Although more elegant, this procedure corresponds to the search for the critical failure surface in conventional analyses. It appears that the same equation could be obtained by considering moment equilibrium about point O, and, therefore, it is not surprising that the stability factors for the same failure surface geometry the authors show in Figures 7 and 8 for the limit equilibrium (3) and plasticity methods (7) are the same except for a slight difference

at ϕ = 25 deg for β = 30 deg, which may be an inaccuracy in the calculation. The authors also show that, for plane failure surfaces, the limit equilibrium method and the upper bound theorem yield identical results and conclude that the application of limit theorems developed in plasticity theory provides a mechanism for bounding the solution and contributes thereby additional information on the validity of the solution.

There are several reasons why the limit theorems fail in this respect when applied to soil mechanics, particularly slope stability problems. First, if the upper and lower bound theorems, originally applied in soil mechanics to zone solutions of the basic differential equations of plasticity, are considered valid for any surface discontinuity, then limit equilibrium solutions are statically admissible and so, therefore, are lower bound solutions. Second, the lower and upper bound theorems may provide a mechanism for bounding the solution, as the authors state, but this bounding would be valid only for the particular discontinuity geometry chosen. To obtain true brackets of the stability factors for the slope stability problem, bounds for all potential failure surface geometries would have to be determined. If a zone solution for the problem had been found, the boundary discontinuity would be unique and this problem would not arise. Third, the whole philosophy of the upper bound theorem is objectionable from the soil mechanics point of view. The validity of a solution is judged on the basis of a velocity field that would obtain after failure if the soil obeyed the prescribed plastic strain rate. Strains and volume changes that the soil undergoes prior to failure in the process of mobilizing its ultimate strength are completely disregarded. These strains and volume changes are appreciable; their compatibility with the stress field is the criterion that should determine the validity of solutions. Admissibility of velocity fields may be important in analyses of plastic flow, as for example in extrusion problems, but preoccupation with velocity fields in slope stability, earth pressure, or bearing capacity problems diverts attention from the analysis of prefailure volume changes and strains.

H. Y. FANG and T. J. HIRST, Closure—The authors wish to thank Karafiath for his valuable comments. They agree that analyses of prefailure volume change and deformation are desirable. However, until improved soil stress-strain characterizations are available, practical solutions to soil engineering problems will continue to be based on simplified idealizations of soil behavior. Limit equilibrium and plasticity approaches are two such idealizations.

Karafiath notes that, in the case of analyses involving the undrained strength parameters, c_u and ϕ_u, plasticity solutions are invalid in the physical sense because the principal stresses are inclined at 45 deg $\pm$ $\phi/2$ to the slip lines and not at 45 deg $\pm$ $\phi_u/2$. Such an observation may be equally applied to limit equilibrium solutions. This incompatibility of theory with real behavior is further complicated by the dilatant nature of soils. Volume changes accompanying the application of shear stress can magnify inhomogeneities initially present in all soils and can lead to the development of preferred planes of failure that are unrelated to the theoretically predicted failure surfaces. In the case of both limit equilibrium and plasticity approaches, such inhomogeneity renders all solutions rigorously unacceptable. The authors never intended to suggest that, in terms of stress-strain behavior, the theory of plasticity is more rigorous than limit equilibrium. Certainly both methods have very real limitations.

That the plasticity solutions (7) are in agreement with the limit equilibrium solutions (3) is not sufficient to imply that the plasticity solutions correspond to conventional analyses. The assumptions on which the plasticity method is based were outlined by Chen and Scawthorn (4) and others, and are fundamentally different from those of the conventional limit equilibrium approach. The fact that the solutions are the same attests to little else than an apparent insensitivity of the stability factors to the assumed material behavior. In this regard, it should be noted that the discrepancy between the limit equilibrium solution (3) and the plasticity solution (7) for ϕ = 25 deg and β = 30 deg is believed to be due to rounding errors in the original limit equilibrium hand calculation.

Application of plasticity theory to slope stability problems will provide upper and lower bounds for the critical height. The nearness of the bounds to the true critical height of an embankment depends on two considerations: (a) How well does the theory of plasticity model the real behavior of the soil in the embankment, and (b) how close are the chosen stress and plastic deformation fields to those that would obtain in a perfectly plastic embankment? The bounding of the solution is valid for any stress or deformation field that satisfies the conditions of the limit theorems. It is not necessary to determine all potential stress and deformation fields (or failure surface geometries) in order to establish true bounds to the solution. The bounds may frequently be improved (i.e., brought closer to the true solution), however, by searching for additional acceptable stress and deformation fields.

If conventional limit equilibrium solutions are statically admissible, then, by definition, they represent lower bound solutions. Conventional limit equilibrium solutions consider conditions along an assumed failure surface only. This, in itself, does not guarantee that the yield criterion is not violated elsewhere, and therefore such solutions are not lower bounds.

Karafiath's objection to the overall philosophy of the upper bound approach cannot be accepted by the authors. The stress-strain relationship used in the upper bound solutions is based on the idealized flow rule applied at the moment of incipient failure, not after failure. Limit equilibrium methods, on the other hand, do not consider the stress-strain relationship of the soil at any stage prior to, at, or after failure.

In summary, a useful and acceptable method of analysis must satisfy two conditions: (a) It must yield realistic answers, and (b) it must be simple to apply. The plasticity theory approach is simple because it provides a closed-form solution to the problem. It has been shown to yield reasonable answers when compared with limit equilibrium solutions whose validity has been established on the basis of practical experience. Finally, application of plasticity theory to slope stability problems provides an opportunity for bounding the solution. Rational interpretation of all of the approximate solutions available to an engineer will continue to be the most practical and attractive approach to slope stability problems until material behavior in complex stress states, such as embankments, is better understood.

Coefficient of Earth Pressure at Rest as Related to Soil Precompression Ratio and Liquid Limit

MEHMET A. SHERIF and DAVID E. KOCH, Department of Civil Engineering, University of Washington

From experiments on three types of Seattle clays conducted in a specially designed stress meter, the authors established a relationship between the precompression ratio, P_R, and the coefficient of earth pressure at rest for overconsolidated soils with $P_R \leq 12$. This relationship is also found applicable to several soil types tested by other researches. A unique relationship was observed between the coefficient of earth pressure at rest for normally consolidated soils and the liquid limit of the soils tested by the authors and others. A reduction in the magnitude of the coefficient of earth pressure at rest for overconsolidated soils as a function of increasing depth below the ground surface is indicated. Also, a rationale for the increase of this coefficient because of overconsolidation is suggested.

•THIS PAPER deals with the coefficient of lateral earth pressure at rest, designated K_0, for overconsolidated and saturated cohesive soils. Samsioe (5) was the first to recognize the increase in K_0 as a result of overconsolidation. Zeevaert (8) and Kjellman and Jakobson (3) have also contributed. Skempton (6) observed increases in the values of K_0 with increasing overconsolidation ratios. His findings were based on the variations of the pore pressure parameter A during triaxial testing of heavily overconsolidated London clay. Recently variations of consolidometer devices, or simple consolidation rings, have been used by Neyer (4), Hendron (2), and Brooker and Ireland (1) for the determination of K_0 during overconsolidation.

In view of the variation in the results obtained by these past researches, which depended on the soil type, it was first decided by the authors to add to the existing body of knowledge by testing three additional soils in a specially designed stress meter—where lateral deformations could be kept at zero—to see how well the previous researches' data concerning the relationship between K_0 and overconsolidation ratio correlated with these findings. Second, it was judged desirable to know how well the increase of K_0 with an increasing overconsolidation ratio correlates with certain basic engineering soil properties such as liquid limit, plastic limit, plasticity index, etc., and what the limitations, if any, would be on such a dependency. Third, it was hoped to provide a rational explanation for the increase of K_0 with an increase in the overconsolidation ratio. The data and the discussions presented below show the extent to which each of these objectives has been realized.

RATIONALE FOR INCREASE OF K_0 DURING OVERCONSOLIDATION

If an attempt is made to analyze stresses—axial and lateral—acting on a unit soil mass at a given depth below the ground surface, would the lateral stresses, σ_3, and axial stresses, σ_1, be equal? This question is apparently basic. If the sample has never carried an axial load greater than what it is presently carrying, then the soil is normally consolidated and the lateral stresses would always be less than the axial stresses. On the other hand, if the sample in its past history was buried under a greater depth of

Paper sponsored by Committee on Embankments and Earth Slopes.

soil, part of which was subsequently removed as a result of erosion, or if it were heavily overloaded by glacial ice loads that disappeared with the melting of the ice, would σ_3 remain constant, or would it be reduced in the same ratio as σ_1? An attempt will be made to answer these pertinent questions.

Because of a reduction in the axial stress, σ_1, upon partial unloading of an overconsolidated clay, the soil finds itself in a different state of stress, to which it tries to adjust. The lateral stresses in this new state can only be determined by the existing axial stresses and the engineering properties of the soil if it were possible for material to experience adequate upward expansion corresponding to a reduction in axial stresses. The question that might be asked at this point is: Can this adequate upward expansion take place?

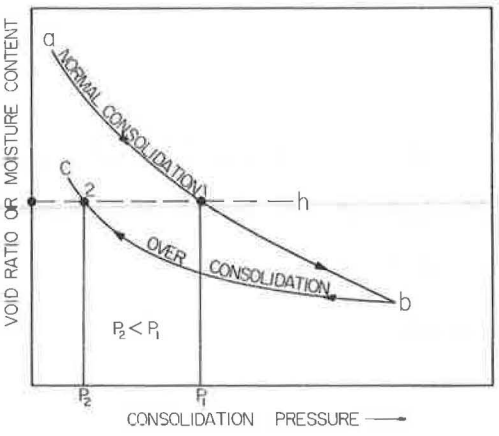

Figure 1. Variation of internal attractive and repulsive forces within the clay-water system during cyclic consolidation process.

To answer this, the authors will consider the physical (external compressive) and physicochemical (internal attractive and repulsive) forces that operate in a soil sample at equilibrium during a cyclic consolidation process. Curves a-b and b-c in Figure 1 represent respectively the normal consolidation and overconsolidation cycles for a given soil sample. The horizontal line h drawn at a given moisture content intersects both the normal consolidation and overconsolidation curves at points 1 and 2 respectively. The fact that a lower external compressive stress is required to keep the soil sample at the same volumetric relationship during the overconsolidation cycle (point 2) than during normal consolidation (point 1) indicates that the internal attractive forces must have increased during overconsolidation. This increase in the internal attractive stresses would, therefore, prevent complete vertical strain recovery of the soil. This being the case, the following relationship should hold:

$$\frac{e_1^*}{e_1} = \frac{1 - 2\upsilon K_o^*}{1 - 2\upsilon K_o} < 1.0 \qquad (1)$$

where

e_1 = the total recoverable vertical strain under axial stress, σ_1, if the soil were able to adequately expand upward after the reduction of the original axial stresses;
e_1^* = the actual vertical strain recovered under the same axial stresses, σ_1, for overconsolidated soil;
υ = Poisson's ratio;
K_o = the coefficient of earth pressure at rest for normally consolidated soil; and
K_o^* = the coefficient of earth pressure at rest for overconsolidated soil that is presently subjected to axial stress σ_1.

Thus, for Eq. 1 to be satisfied, K_o^* must be greater than K_o. Consequently, the originally induced lateral stresses cannot be reduced at the same ratio as axial stresses. This would mean that the lateral earth pressures for overconsolidated soils will be greater than those for corresponding normally consolidated soils. Depending on the degree of overconsolidation, it is entirely possible that the lateral stresses may even be greater than the present axial stresses, thus making the coefficient of lateral pressure greater than unity. The experimental data obtained from tests conducted by the authors and others on overconsolidated clays support this argument, as indicated in the following paragraphs.

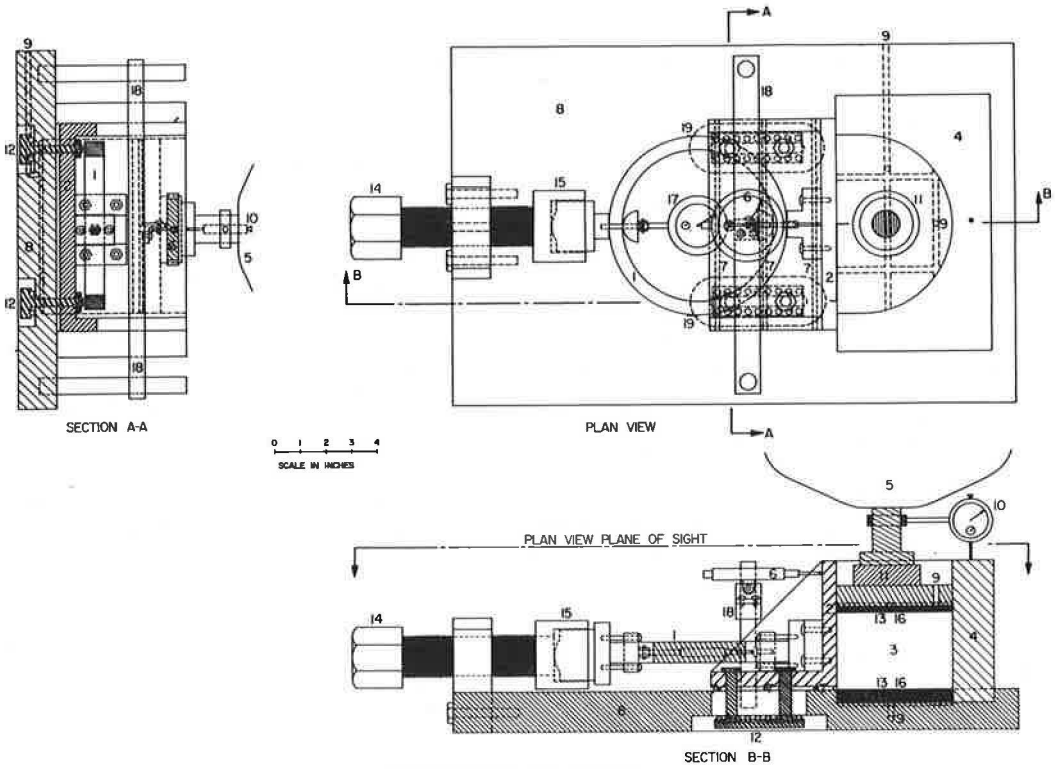

DESCRIPTION OF PARTS

1. Proving ring
2. Retaining wall
3. Soil sample
4. Soil container
5. Vertical pressure loader
6. Horizontal deformation measuring gage (0.0001 in.)
7. Cylindrical rollers
8. Base
9. Drainage outlets
10. Vertical consolidation measuring gage (0.001 in.)
11. 20,000 lb capacity load cell
12. Ball bearing assembly to prevent tilting and rotating of the retaining wall.
13. Top 8 bottom porous plates
14. Screw (12 threads/in.)
15. Socket
16. Screen
17. Proving ring dial gage
18. Support for horizontal deformation measuring gage
19. Electric strain gages

Figure 2. Stress meter.

COEFFICIENTS OF LATERAL STRESSES IN OVERCONSOLIDATED SOILS

Instrumentation

For the purpose of studying the state of lateral stresses in heavily overconsolidated clay, it was essential to conduct the experiments in a specially designed apparatus so as to duplicate, as closely as possible, the past stress history of soils and to estimate realistically the presently existing lateral stresses in the field. It was necessary for the apparatus to be equipped with refinements that could minimize experimental error and yet be flexible enough to serve well the various purposes for which it was intended. The apparatus consists of the following main parts:

1. A semicircular soil container 7.0 in. in diameter and 3.5 in. deep (Fig. 2, item 4). These dimensions were chosen to accommodate testing of a large enough sample with minimum sidewall friction, within the limiting capacity of the available loading facilities.

2. One yielding wall, with adequate flexibility, used in connection with at-rest, active, and passive earth pressure measurement. This part is a solid retaining wall in the form of an angle (Fig. 2, item 2) resting on very accurately made rollers (Fig. 2, item 7). In addition, special arrangements are made to prevent the wall from tilting in horizontal and vertical directions and to further minimize the friction between the moving wall and the base (Fig. 2, item 12).

3. A specially designed 10,000-lb-capacity proving ring (Fig. 2, item 1), equipped with a 1.0001-in. strain dial gage, used to monitor the magnitude of lateral stresses exerted by the soil against the retaining wall. Also, two electrical strain gages are installed on the outer surface of the ring to increase its load-reading sensitivity (Fig. 2, item 19). While one end of the proving ring rests against the retaining wall, the other end is fitted into a specially designed socket secured to the base (Fig. 2, item 15) by which the stresses on the proving ring can be varied to either prevent or control the amount and direction of lateral yielding of the retaining wall as dictated by theoretical and practical requirements. The ring is designed to withstand a force of 10,000 lb with a maximum deformation of 0.172 in. and is made of specially forged and heat-treated steel with 197,000-psi yield strength.

4. A stress-controlled 11,000-lb-capacity, calibrated, air-operated loader (Fig. 2, item 5), used to apply axial stresses. The magnitudes of the axial stresses during loading and unloading cycles are determined using a 20,000-lb-capacity, calibrated Baldwin Lima Hamilton-type C2-MIC load cell (Fig. 2, item 11).

Types of Soils Tested

All the experiments were conducted on Seattle clays obtained from various locations along the freeway. Table 1 gives pertinent engineering properties of the soils tested. This table also includes data on another Seattle clay tested by Neyer (4).

Experimental Data

Several experiments were conducted on samples 1, 2-1, 2-2, and 3 (Table 1) with the object of determining K_o, the coefficient of lateral earth pressure at rest as defined by

$$K_o = \frac{\sigma_3}{\sigma_1} \tag{2}$$

where

σ_1 = axial stresses applied to the sample by the hydraulic loader, and
σ_3 = measured horizontal stresses transmitted against the stationary retaining wall at the end of 100 percent consolidation under σ_1 or at a consolidated equilibrium state, as defined by Tschebotarioff (7).

The soils were first remolded and thoroughly mixed with distilled water at their liquid limit consistency and stored in a humid room in plastic containers for a period of 2 weeks prior to testing. Subsequently, they were placed in the stress meter and subjected to incremental increases in axial stresses up to a maximum of 333 psi for sample 1, 375 psi for sample 2-1, 395 psi for sample 2-2, and 380 psi for sample 3, and then reduced to zero in decrements. A 24-hour period was allowed to lapse between each stress increment and decrement during loading and unloading cycles. This time was found to be adequate for the soil to reach 100 percent consolidation, which was apparent from the consolidation-time curves plotted during the experiments.

TABLE 1

ENGINEERING PROPERTIES OF SOILS TESTED

Sample Number	Field Water Content (percent)	Liquid Limit (percent)	Plastic Limit (percent)	Percent Clay
1	32.6	56.8	33.7	62
2-1	27.3	46.8	29.2	53
2-2	27.3	46.8	29.2	53
3	22.7	38.2	28.0	—
Neyer	—	66.7	24.6	68

The at-rest lateral stresses, induced during the axial loading and unloading cycles, were measured by the proving ring at the end of 100 percent consolidation under each axial load increment. The proving ring was attached to the retaining wall on one end and to the specially designed socket on the other end. The socket was designed so that the forces on the proving ring could be increased smoothly to prevent lateral movement of the retaining wall.

Figures 3, 4, 5, and 6 show the relationships obtained between the axial and the lateral stresses during the experiments.

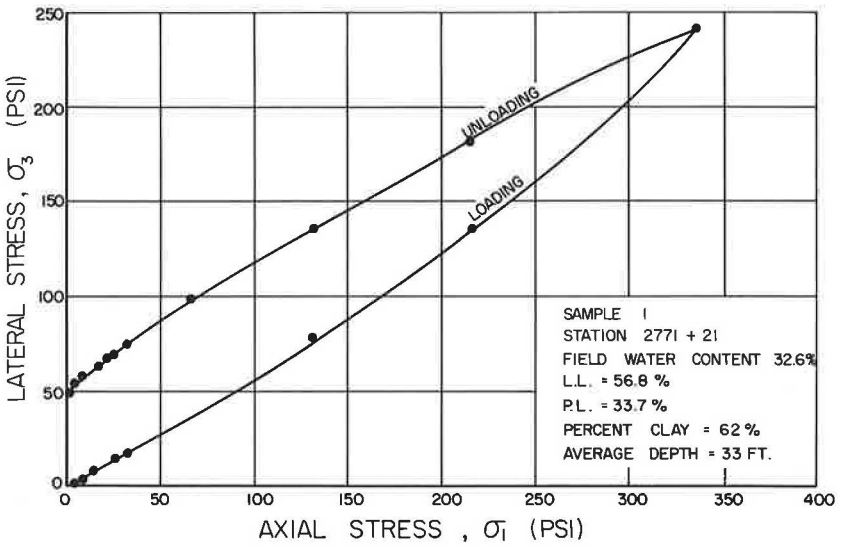

Figure 3. Relationship between axial and lateral stresses during loading and unloading cycles on remolded Seattle clays—sample 1.

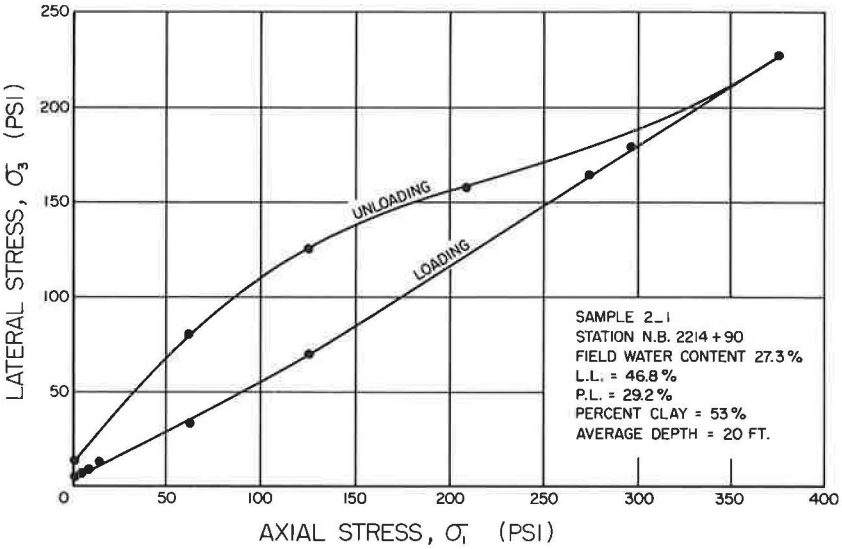

Figure 4. Relationship between axial and lateral stresses during loading and unloading cycles on remolded Seattle clays—sample 2-1.

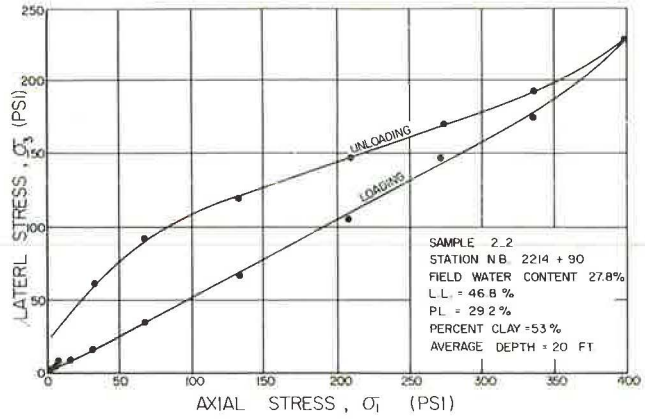

Figure 5. Relationship between axial and lateral stresses during loading and unloading cycles on Seattle remolded clays—sample 2-2.

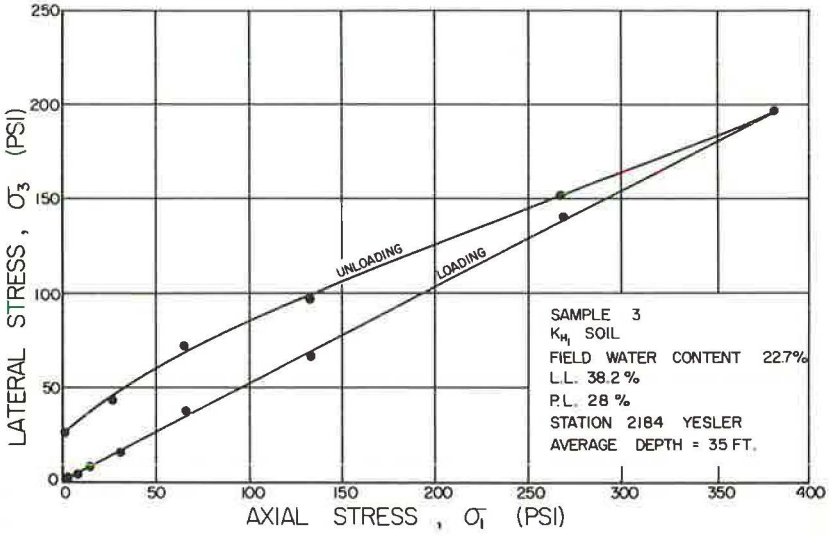

Figure 6. Relationship between axial and lateral stresses during loading and unloading cycles on remolded Seattle clays—sample 3.

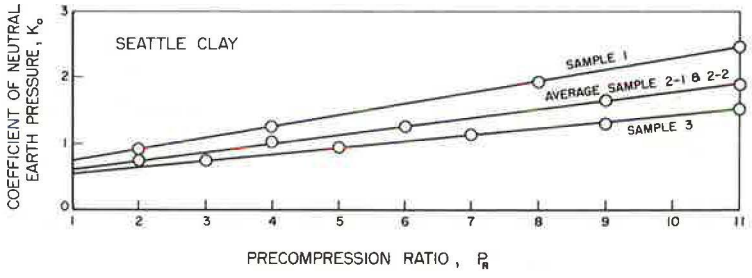

Figure 7. Precompression ratio, P_R, versus coefficient of neutral earth pressure, K_o (during overconsolidation).

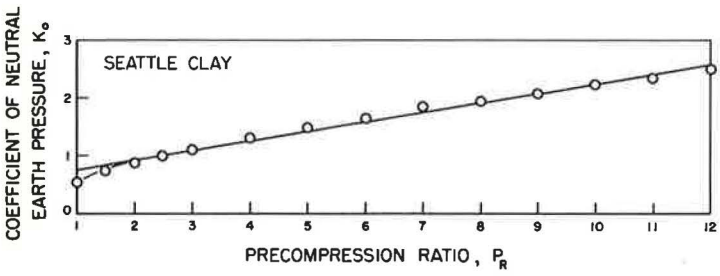

Figure 8. Precompression ratio, P_R, versus coefficient of neutral earth pressure, K_o, of Seattle clay—plotted from Neyer's data (4).

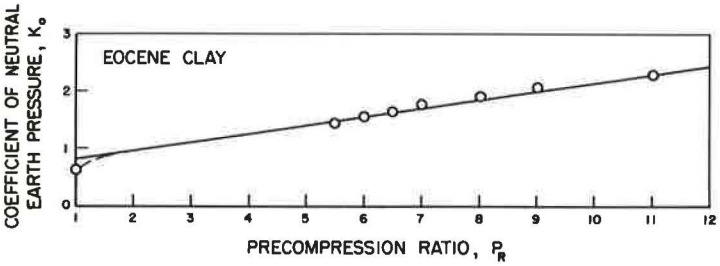

Figure 9. Precompression ratio, P_R, versus coefficient of neutral earth pressure, K_o, of Eocene clay—plotted from Skempton's data (6).

An important outcome of this investigation is the data shown in Figure 7. The curves for samples 1, 2-1, 2-2, and 3 in Figure 7 were obtained from the experimental data shown in Figures 3 through 6 by plotting the overconsolidation ratio, P_R, against K_o. P_R is defined as the ratio between the experimental precompression stress, P_C, to which the soil is subjected, and the axial stress, σ_1, acting on the sample during the unloading cycle. K_o is defined as the ratio between the horizontal stress registered on the proving ring attached to the stationary wall and the axial stress, σ_1, during the same process. For comparison, the authors plotted Neyer's data on Seattle clays (4), which were obtained from strain gages placed at the outer face of a conventional consolidation ring (Fig. 8), and Skempton's results from Eocene clay (6), which were obtained from triaxial tests (Fig. 9). Experimental results obtained by Brooker and Ireland (1) from five different soils tested in a Hendron-type (2) consolidation test unit were plotted by the authors and summarized in Figure 10. A close correlation between the behavior of the soils tested by the authors and other investigators working with different soils is readily discernible from the data shown in Figures 7, 8, 9, and 10. Furthermore, these

TABLE 2
BEHAVIOR OF SOILS TESTED

Soil Type	λ	α	Soil Type	λ	α
Chicago clay	0.50	0.110	Eocene clay	0.83	0.144
Goose Lake clay	0.55	0.090	Seattle clay	0.76	0.164
Weald clay	0.65	0.120	Seattle clay No. 1	0.75	0.174
London clay	0.80	0.090	Seattle clay No. 2	0.63	0.128
Bearpaw clay	0.85	0.080	Seattle clay No. 3	0.57	0.097

curves can be represented in the form

$$K_o = \lambda + \alpha\,(P_R - 1) \tag{3}$$

where λ and α vary for different soils as given in Table 2.

A plot of λ and α for each soil against its respective liquid limit is shown in Figure 11. It is significant to note that the data points corresponding to λ lie almost on a straight line for all soils shown in Table 2. The α values, on the other hand, vary widely and randomly. The λ curve in Figure 11 can therefore be represented in the form

$$\log \lambda = 0.00275\,(LL - 20) + \log\,(0.54) \tag{4}$$

Because λ in Eq. 4 corresponds to the K_o value at $P_R = 1$ (see Eq. 3 and Figs. 7 through 10), therefore λ equals the coefficient of earth pressure at rest for normally consolidated clays. Thus, Eq. 4 establishes a relationship of practical significance between the coefficient of earth pressure at rest for a normally consolidated soil and its liquid limit. Although no correlation between the authors' and other investigators' data regarding α values was obtained, a probable relationship between α and the liquid limit

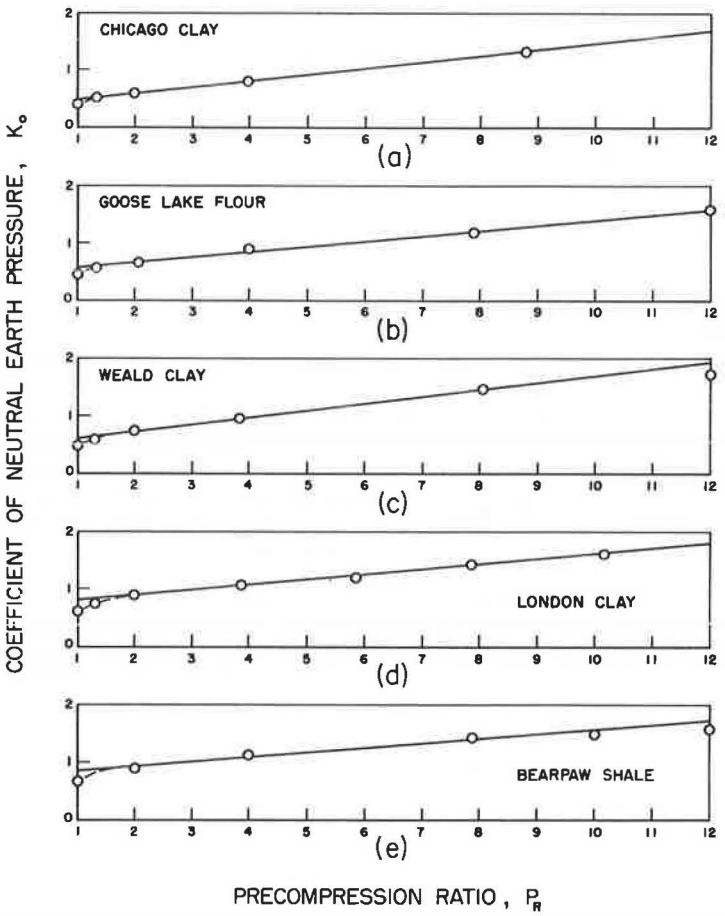

Figure 10. Precompression ratio, P_R, versus coefficient of neutral earth pressure, K_o—plotted from Brooker and Ireland's data (1).

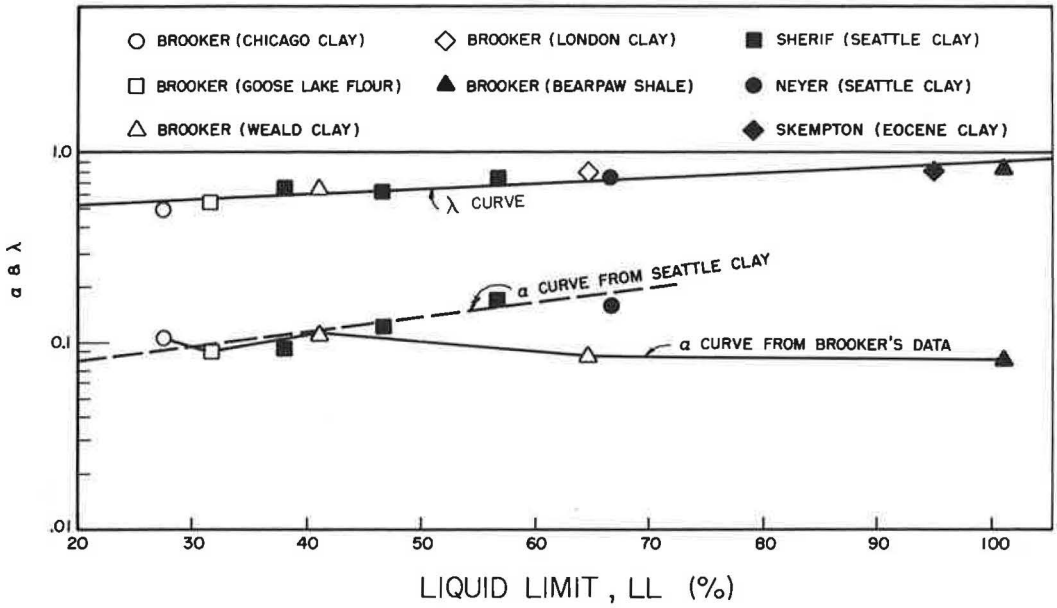

Figure 11. Liquid limit versus α and λ.

is discernible for local Seattle clays, as shown by the dashed line in Figure 11. For Seattle clays only, α can be represented in the form

$$\log \alpha = 0.00745 \, (LL - 20) + \log (0.08) \tag{5}$$

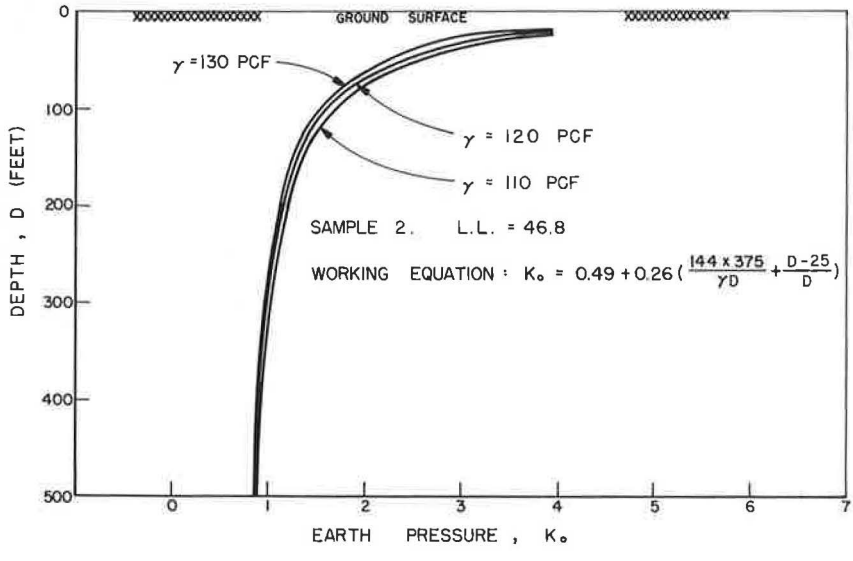

Figure 12. Neutral coefficient of earth pressure versus depth.

It is clear that, in order to apply Eq. 3 in practice, the engineer must first run consolidation tests to determine the precompression pressure, P_C (from which he can determine the precompression ratio, P_R), and then a liquid limit test to determine the values of λ (from Eq. 4) and α (from Fig. 11), and afterward substitute these values into Eq. 3 to find K_o for overconsolidated soils. It is significant to note, however, that, as the precompression ratio theoretically approaches infinity (which will be the case as the axial stress, σ_1, nears zero on the surface of the ground), the K_o values also approach infinity, and, therefore, the validity of Eq. 3 becomes questionable at the ground surface. As a matter of fact, the portion of the data not shown in Figures 7, 8, 9, and 10 indicates that the linearity between K_o and P_R ceases to exist beyond an average P_R value of 12 in all soils given in Table 2. Therefore, Eq. 3 is restricted in application to overconsolidated soils with precompression ratios less than 12.

Figure 12 is a typical representation of the relationship among the coefficient of earth pressure at rest, K_o, the depth of the soil below the ground surface, and physical soil properties such as density and liquid limit for one of the Seattle clays tested. Figure 12 shows that the K_o value for overconsolidated soils decreases with increasing depth. This is only logical in view of the fact that the soil element buried at very great depths below the ground surface will not be affected by relatively small variations on the surface of the ground, and a soil at such great depths can be assumed to be normally consolidated.

ACKNOWLEDGMENTS

The experimental data included in this paper were obtained during the authors' research study on the engineering behavior of Seattle freeway clays, which was sponsored jointly by the Washington State Highway Department and the U. S. Bureau of Public Roads. The authors gratefully acknowledge the support and the consistent cooperation received from these sponsors. Suggestions and criticisms from H. Bolton Seed and R. G. Hennes during the preparation of this paper are also appreciated.

REFERENCES

1. Brooker, E. W., and Ireland, H. O. Earth Pressures at Rest Related to Stress History. Canadian Geotechnical Jour., Vol. 2, Feb. 1965, pp. 1-15.
2. Hendron, A. J. The Behavior of Sand in One-Dimensional Compression. Dept. of Civil Engineering, Univ. of Illinois, PhD thesis, 1963.
3. Kjellman, W., and Jakobson, B. Some Relations Between Stress and Strain in Coarse Grained Cohesionless Materials. Proc. Royal Swedish Geotechnical Institute, No. 9, 1955.
4. Neyer, J. C. Lateral Pressure in Preconsolidated Clay. Univ. of Washington, MS thesis, 1963.
5. Samsioe, A. F. Report on the Investigation of the Compressibility of the Ground of the Hydro-Electric Power Plant Svir 3. First Internat. Conf. on Soil Mech. and Found. Engineering, Vol. 3, 1953, pp. 41-47.
6. Skempton, A. W. Horizontal Stresses in an Overconsolidated Eocene Clay. Proc. Fifth Internat. Conf. on Soil Mech. and Found. Engineering, Vol. 1, 1961, pp. 351-357.
7. Tschebotarioff, G. P., and Welch, J. D. Effect of Boundary Conditions on Lateral Earth Pressures. Proc. Second Internat. Conf. on Soil Mech. and Found. Engineering, Vol. 3, 1948, pp. 308-313.
8. Zeevaert, L. Discussion. Proc. Third Internat. Conf. on Soil Mech. and Found. Engineering, Vol. 3, 1953, pp. 113-114.

Dynamic Behavior of Embedded Foundation-Soil Systems

YONG S. CHAE, Department of Civil Engineering, Rutgers, The State University

Development of theoretical solutions to the problem of dynamic interaction between foundation and underlying soil is discussed with a view to idealizations and uncertainties associated with the theories, with a particular emphasis on the effect of embedment on the interaction. An experimental investigation to study the dynamic behavior of embedded foundation-soil systems is described. Based on small-scale model tests on footings of various sizes and shapes, evaluation is made of the effect of embedment depth, mass ratio, and foundation shape on the dynamic response of the system. It is found that the amplitude of motion of the embedded foundation is greatly reduced by the additional shearing resistance along sides of the foundation and a shift in the contact pressure distribution. Embedment is found, however, to have no appreciable effect on the resonant frequency of the system. The system with a higher mass ratio produces a greater amplitude for a given depth of embedment, but the effect of mass ratio becomes smaller with increasing embedment depth. The effects of embedment depth, mass ratio, and foundation size are expressed in terms of two newly defined dimensionless parameters, the amplitude reduction coefficient and the embedment factor, by means of which the dynamic response of embedded foundations can be adequately determined.

•IN RECENT YEARS, there has been an increasing demand for knowledge of the dynamic behavior of foundation-soil systems that can be used in foundation designs for facilities that incorporate dynamic loading. These facilities range from industrial machine foundations and radar towers to highway and airport construction.

A properly designed highway or airport pavement must first of all meet the general requirements for all foundations. The loads imposed by traffic have to be transferred to soil layers capable of supporting them without failing in shear (bearing capacity), and the deformations of the soil layers should be such that they do not suffer excessive permanent settlement. Therefore, in the design and analysis of pavement-soil systems the most critical quantities considered are the bearing capacity and deformation characteristics of the underlying soil, which, in turn, are dependent on the material constants of the soil (the modulus of elasticity, shear modulus, Poisson's ratio, coefficient of subgrade reaction, etc.). The success with which the road or runway is built thus depends on the accuracy with which the material properties of the soil are determined.

At present roads and runways are largely designed on the basis of knowledge of the performance of other roads under similar traffic and subgrade conditions and by testing soil under static loading, such as unconfined compression, plate loading, density, CBR, and others. The use of static loading, however, does not represent the true nature of actual loading resulting from traffic, which is of a dynamic nature. Because the applied load is alternating and repetitive in nature, the material properties under such a load must be investigated in terms of dynamic response and behavior of pavement-soil systems. Such a dynamic testing, in a reversed process, will also provide a rapid, nondestructive testing technique for assessing the performance of a road.

Paper sponsored by Committee on Foundations of Bridges and Other Structures.

Past research indicates that theoretical values of the stresses and deformations generated by moving vehicles in multilayered elastic systems depend on the relative values of the dynamic elasticity of the layers forming the road and their thicknesses. It is, therefore, essential to obtain information concerning the dynamic material properties of the common road-making materials under repeated loading of the form applied by traffic. The ultimate objective of the measurement of dynamic properties would be then to develop a method of pavement design based on the dynamic behavior of pavement-soil systems.

DEVELOPMENT OF DYNAMIC ANALYSIS

An analytical solution that has been gaining wide acceptance among researchers and engineers in recent years is the theory that treats the system as an oscillator resting on a semi-infinite, homogeneous, isotropic, elastic body (elastic half-space). The theory was first developed by Reissner (9), who presented a solution for the case of vertical excitation of an oscillator on a circular base, assuming a uniform contact pressure between an oscillator and the elastic body. Reissner's theory has since been extended by Sung (12), who treated the problems for various types of contact pressure distribution, and by Arnold, Bycroft, and Warburton (1), who considered cases for different modes of vibration. The elastic half-space theory was used by Richart and Whitman (11) to compare with a very extensive series of field tests conducted at the Army Engineer Waterways Experiment Station (5). The comparison showed a reasonably good agreement between the theory and the field experiment.

More recently, it has been demonstrated by Lysmer and Richart (8) that the theory for footings resting on an elastic half-space leads to solutions whereby the dynamic behavior of a footing resting on an actual foundation can be represented by a "lumped parameter" system consisting simply of a mass-spring-dashpot. In such "lumped" systems, the mass represents all of the inertia present in the actual system, while the springs and dashpots respectively represent all of the deformability and damping present in the actual system. The key step is evaluation of parameters of the equivalent lumped system. Once this has been done, the response of the actual system can be readily obtained by the use of available mathematical solutions of the lumped system.

DETERMINATION OF DYNAMIC PROPERTIES OF SOILS

Whether the theoretical solutions are used directly (elastic half-space) or indirectly in the form of the lumped parameter system, however, the ability of this theory to predict dynamic response of real foundations depends largely on the accuracy with which the material properties of soil are determined. There are a number of experimental methods to determine the dynamic properties. These methods may be divided into two general categories: (a) those in which tests are performed on a small sample of soil usually in triaxial compression, and (b) those in which the testing on soils is considered to be in situ. The "resonant column" method and the "amplitude ratio" method are performed on soil specimens encompassed in a triaxial chamber. The "wave propagation (seismic)" method and the "elastic half-space" method, in which a small- or large-scale vibrator is set on the soil mass, are performed on soils in situ or in simulated in-situ conditions. Detailed discussion of various methods, test results, and comparisons were made by Chae (3).

The elastic half-space method has been widely used by many researchers in the past as a means of determining the material constants of soil. The accuracy that the method yields, however, is dependent on how closely the actual foundation conditions agree with the idealized condition assumed in the theory, as the effect of certain parameters are either ignored or simply idealized in the theory. The analysis and determination of dynamic response require, therefore, consideration of the following additional parameters: (a) the magnitude of dynamic force applied, (b) the type of dynamic contact pressure distribution between the foundation and soil and its variation with frequency, (c) the shape of the foundation, and (d) the embedded depth of foundation.

EVALUATION OF PARAMETERS NOT CONSIDERED IN THEORY

In the past some progress has been made in evaluating the effect of some of these parameters. The following information briefly summarizes the work done to date.

Magnitude of Dynamic Force Applied

Determination of the dynamic load requires careful consideration. The magnitude, direction, and point of application of various forces applied determine the mode of vibration. The effects of this parameter were studied by Fry (5), Jones (7), and Chae (2). They have shown that the effect of increasing the input force is to decrease the resonant frequency, and the decrease is greater with the systems having higher mass ratios. This variation of resonant frequency with the magnitude of input force is not indicated in the theory. This effect may be explained by the fact that a change in the magnitude of input force causes a change in the pressure distribution under the footings, and the resonant frequency is in turn dependent on the pressure distribution. This point was elaborated by Richart (10) in connection with his concept of an "effective radius" to be used as a tool for the transformation of pressure distribution caused by the variation in input force.

Type of Dynamic Contact Pressure Distribution

The elastic half-space theory assumes the pressure distribution at the base of the footing to be constant regardless of the exciting frequency. The investigation conducted by Chae (2) has shown, however, that it varies with the frequency. The test results on an Ottawa sand show that under a constant total soil reaction the dynamic pressure appears to shift toward the edge of the footing with increasing frequency, changing the shape of distribution from a parabolic type to that corresponding to a rigid base. Even with a rigid base resting on an ideal elastic medium the effect of changing the frequency is to change the intensity of pressure across the base of the footing. The variation of dynamic pressure resulting from a change in frequency is a consequence of the change in amplitude and phase relations between the reaction pressures on each ring, caused by a change in the wave velocity traveling in the soil. Thus, the dynamic soil pressure against the footing is a function of the velocity of the footing moving into the soil and the velocity of the elastic waves in the soil that dissipate this input energy.

Shape of Foundation

In theory, the effect of the footing shape is ignored. The theory is derived on the basis of circular footings. In the case of the footing shape being other than a circle, an equivalent radius based on an equal area is used. This means that a footing of any shape, whether it be circle or rectangle, would yield the same response as long as the area of the footing remains the same. An investigation has been conducted at Rutgers (4) using small-scale models for the vertical mode of vibration. There were six circular, six square, and ten rectangular model footings tested in a soil tank filled with a New Jersey beach sand.

The test results and analysis thereof have revealed that the resonant frequency increases and the maximum amplitude of displacement decreases with a decrease in mass ratio for all shapes of footings, as predicted by the elastic half-space theory. However, the resonant frequency of circular footings is less sensitive to a change in the mass ratio than the square or rectangular footings, and the displacement of rectangular footings is less sensitive to a change in the mass ratio than the circular footings. It has also been found that the use of an equivalent radius based on equal area in computing the resonant frequency of square and rectangular footings appears valid because the predicted results compared favorably with the experimental results. The use of an equivalent radius based on equal area appears valid for the determination of mass ratio in computing maximum amplitude of square footings, but it is not valid for rectangular footings. A suggestion is made to use an equivalent radius, based on a perimeter ratio, in computing the dynamic response of rectangular foundations.

EFFECT OF FOOTING EMBEDMENT ON DYNAMIC BEHAVIOR

Whereas the theory treats the footing to be resting on the surface of elastic half-space, actual foundations usually are partially embedded. A mathematical model of such an embedded footing is shown in Figure 1. In this figure, m_o, r_o, and D are the mass, radius, and diameter of the footing respectively; D_f is the depth of embedment; G, ρ, and μ are the shear modulus, mass density, and Poisson's ratio of the soil; and Q_1 is the amplitude of input force. For the system of a footing resting on the surface, the resonant frequency f_o and maximum amplitude $A_{o,max.}$ can be expressed as follows in the simplified elastic half-space theory:

$$f_o = \frac{(G/\rho)^{1/2}}{2\pi r_o} \cdot \frac{(B - 0.36)^{1/2}}{B} \tag{1}$$

$$A_{o,\,max.} = \frac{Q_1}{K} \quad \frac{B}{0.85(B - 0.18)^{1/2}} \tag{2}$$

in which B = mass ratio, defined as $m_o \cdot (1 - \mu)/4\rho r_o^3 = b(1 - \mu)/4$, and K = spring constant, defined as $4Gr_o/1 - \mu$. In the case of the lumped parameter system, the resonant frequency and maximum amplitude can be readily obtained once the parameter mass, spring constant, and damping are evaluated. From the interrelationship among the material constants G or K and the dynamic response f_o or $A_{o,max.}$, the effect of each parameter on the other can be determined for a given system having a mass ratio B.

There have been some attempts to investigate analytically, mostly based on the finite element technique, the effect of embedment on dynamic behavior under various modes of vibration. However, no major results have been published as of the time of this writing. The results of experimental work by the Corps of Engineers (5) have shown that the effect of partial embedment has been, in general, to increase the resonant frequency and to decrease the amplitude of motion at resonance. This indicates changes in the dynamic properties of soil, whether they be expressed in terms of the equivalent spring constant and damping or in terms of the elastic moduli.

The reduction in motion of an embedded rigid foundation is due primarily to the additional shear resistance along sides of the footing and to a shift in the contact pressure distribution caused by the surcharge around the footing. Thus, the effect of embedment depth (or the amount of surcharge), weight, and size of the footing.

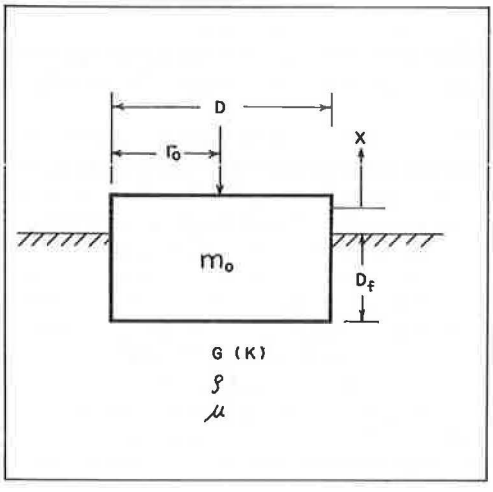

Figure 1. Mathematical model of embedded footing.

EXPERIMENTAL INVESTIGATIONS

Experimental investigations were based on the behavior of model footings embedded in a sand bed and subjected to steady-state vibration. There were five footings of various shapes, sizes, and weights yielding eight different test systems. The test setup was the same as that reported by Chae (4) in connection with previous research. A brief description follows.

Sand Bin and Loading Frame

A sand bin was constructed of 8-in. three-cell cinder blocks. It had inside dimensions of 4.8 by 4.8 ft and was 4.0 ft in height. The holes in the blocks were filled with mortar, and the wall was reinforced to ensure adequate resistance to the lateral

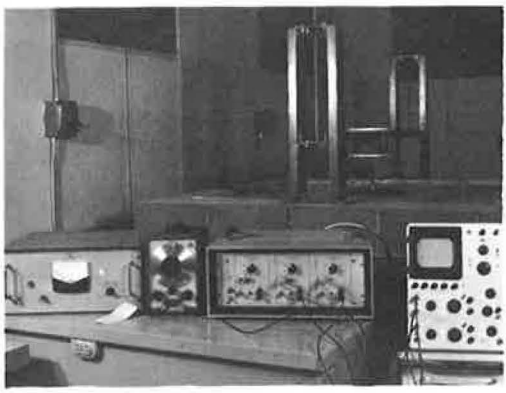

Figure 2. Overall experimental setup.

earth pressure and the lateral component of force from the loading frame.

The sand used was beach sand from Seaside Heights, New Jersey, and 93 percent of the sand was retained between the No. 20 and No. 60 sieves. The sand was compacted in six layers, each approximately 8 in. thick, using a vibratory compactor. A density test was performed during and after the compaction and the density was computed to be 110.2 pcf and to have a void ratio of 0.51.

The loading frame was designed so that its resonant frequency would not be within the predicted testing range and to make the structure as rigid as possible. The loading frame, shown in Figure 2, consisted of vertical columns and a cross beam to which the oscillator was attached. The height of the oscillator in relation to the footing was adjustable as necessary.

Footings

The footings were made of 1-in. thick steel plates cut to various sizes and shapes. Three circular footings, a square footing, and a rectangular footing were used. Footings of circular shape were dimensioned to provide area to perimeter ratios of 2, 3, and 4 for the purpose of comparison in analyzing the results. The square and rectangular footings were designed with area to perimeter ratios of 3 and 4 respectively to aid in the study of the effect of shape of a footing on the dynamic response. The footing properties are given in Table 1. To obtain a more diversified scope of testing, provisions were made to use the various footings as extra weight on each other by bolting one or more footings together. The mass ratio could then be varied for a given shape of footing by adding as many weights as desired.

Embedment of the footing was achieved by placing sand surcharge around the thick aluminum tube that was rigidly bolted to the perimeter of the footing. The embedment depth was varied by the depth of surcharge around the footing. The tube was found to be very rigid laterally so that the shear was fully mobilized along the perimeter.

Overall Test Setup and Procedure

Figure 2 shows the overall setup in the laboratory. Figure 3 shows a schematic diagram of the instrumentation sequence in the overall test setup. The vibrator used was a constant-force electromagnetic exciter. The exciter received its alternating

TABLE 1

PROPERTIES OF MODEL FOOTINGS

Shape of Footing	Dimension (in.)	Weight (lb)	Area (sq in.)	Area to Perimeter Ratio	Mass Ratio, b	Equivalent Mass Ratio, B
Circular	D = 8	17.3	50.3	2	4.3	0.72
		35.9			8.8	1.47
	D = 12	37.1	113.1	3	2.7	0.45
		88.4			6.4	1.07
	D = 16	62.4	201.8	4	1.9	0.32
		139.1			4.3	0.72
Square	12 by 12	45.4	144.0	3	2.2	0.37
Rectangular	12 by 24	90.5	288.0	4	1.5	0.25

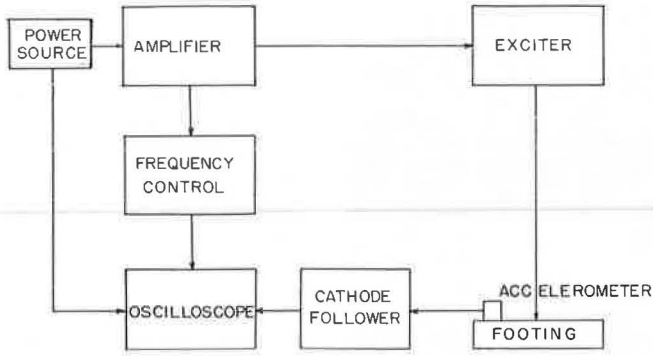

Figure 3. Schematic diagram showing instrumentation sequence.

current from an amplifier that was connected to an outside power source. The frequency was varied by a wide-range frequency meter. The accelerometer was used to measure the footing acceleration and consequently the footing displacement. The acceleration range of the accelerometer was 0.001 to 1,000 g at a frequency range of 0.4 to 2,000 cps. The accelerometer produced a signal with a high impedence and consequently it was connected to a cathode follower. The Tektronix oscilloscope provided linear dual-beam displays with a wide range of sweep rates combined with a high input sensitivity.

After the equipment was connected as shown in Figures 2 and 3, the input current was set at a desired level and kept constant so that the amplitude of input force remained constant. The frequency was then varied in much smaller increments. The peak-to-peak value of footing acceleration and phase angle between the input force and acceleration were recorded at each frequency. The displacement was then computed from the acceleration and frequency measured.

ANALYSIS OF TEST RESULTS

The experimental results for the resonant frequency are given in Table 2, and the results for the maximum amplitude are plotted in Figures 4, 5, and 6 for the circular footings, in Figure 7 for the square footing, and in Figure 8 for the rectangular footing. In these figures variation of the maximum amplitude is shown as a function of embedment depth, which was varied up to 10 in.

It is observed in these figures that embedment has, as expected, a significant effect on the maximum amplitude of motion. This can readily be explained in terms of change in the material constant G or stiffening spring constant K in the lumped-parameter system. These figures also show the general trends, as far as the maximum amplitude is

TABLE 2

EXPERIMENTAL RESULTS FOR RESONANT FREQUENCY

Footing	Mass Ratio	Depth of Embedment (in.)					
		0	2	4	6	8	10
Circular							
D = 8 in.	4.3	131	129	128	121	121	—
	8.8	132	131	125	125	121	—
D = 12 in.	2.7	135	136	134	129	128	—
	6.4	127	125	128	125	122	—
D = 16 in.	1.9	134	129	126	123	124	123
	4.3	120	116	117	115	116	114
Square	2.2	129	132	129	132	129	122
Rectangular	1.5	130	131	121	130	131	130

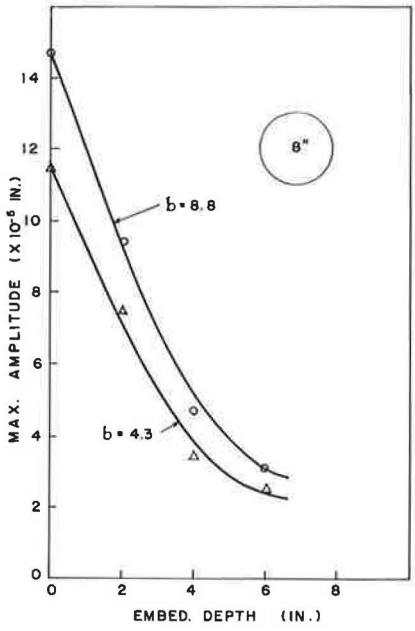

Figure 4. Maximum displacement amplitude versus embedment depth for 8-in. diameter footing.

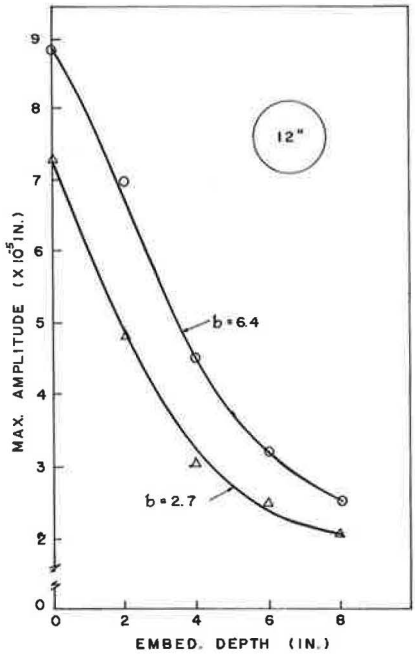

Figure 5. Maximum displacement amplitude versus embedment depth for 12-in. diameter footing.

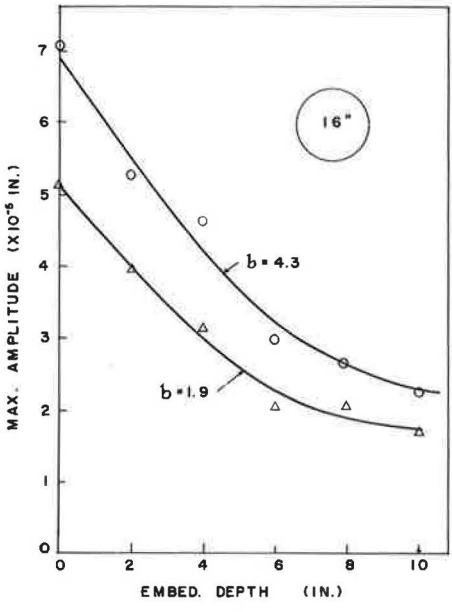

Figure 6. Maximum displacement amplitude versus embedment depth for 16-in. diameter footing.

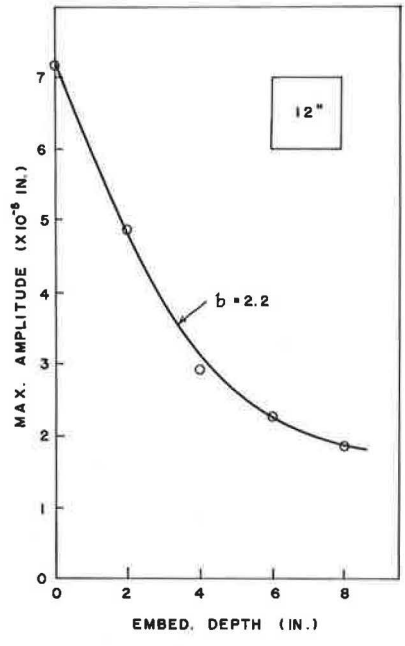

Figure 7. Maximum displacement amplitude versus embedment depth for square footing.

concerned, as one would expect from the elastic half-space theory for a constant force oscillator. The maximum amplitude is greater with higher mass ratio for a given system having the same input force, and this is true with the embedded footings. The effect of mass ratio seems, however, to get smaller as the embedment depth is increased. Another point of interest is that the rate of decrease becomes smaller with increasing embedment depth and it appears that beyond a certain depth of embedment further reduction in amplitude may not be obtained.

It is noted in Table 2 that embedment has no appreciable effect on the resonant frequency. Theoretically, an increase in the value of spring constant (stiffening) should increase the resonant frequency as long as the mass remains the same. With embedded footings, however, the mass of the system appears to increase because of the surcharge neutralizing the stiffening effect of the spring.

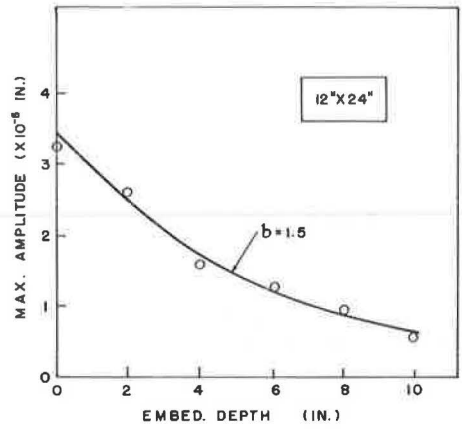

Figure 8. Maximum displacement amplitude versus embedment depth for rectangular footing.

A comparison of Figure 7 with Figure 5, and Figure 8 with Figure 6 shows that the effects of embedment for square and rectangular footings are similar to those for circular footings having the same mass ratios. The mass ratio of a noncircular footing can be computed in terms of an equivalent radius based either on equal area or on a perimeter ratio as defined by Chae (4).

An interesting feature of the experimental results is exhibited when the amount of amplitude reduction at each embedment depth is compared to the maximum amplitude of motion of the footing resting on the surface of soil. To show this, two new dimensionless quantities, designated as the amplitude reduction coefficient R_f and the embedment factor N, are introduced and are defined as

$$R_f = \frac{A_{max.}}{A_{o,\,max.}} \tag{3}$$

$$N = \frac{D_f}{D} \tag{4}$$

Figures 9, 10, and 11 show the amplitude reduction coefficient plotted against the embedment factor for the three circular footings. These figures show patterns generally similar to those for the amplitude-embedment depth curves. The reduction coefficient decreases as the embedment factor increases, and the rate of decrease becomes smaller with an increasing embedment factor. It is of interest to note, however, that the mass ratio does not significantly change the reduction coefficient for a given embedment factor.

To elaborate the fact just pointed out, the test results shown in Figures 9, 10, and 11 are combined and plotted in Figure 12. It is evident in this figure that the relationship between the reduction coefficient and the embedment factor can be derived independently of the mass ratio. This implies that, for any footing-soil systems, the reduction of amplitude due to embedment can be determined once the amplitude of the footing resting on the surface $A_{o,\,max.}$ and the embedment depth D are known. In practical situations the embedment factor ranges up to 0.5. For this range the reduction in amplitude is up to about 60 percent, and the reduction coefficient may be

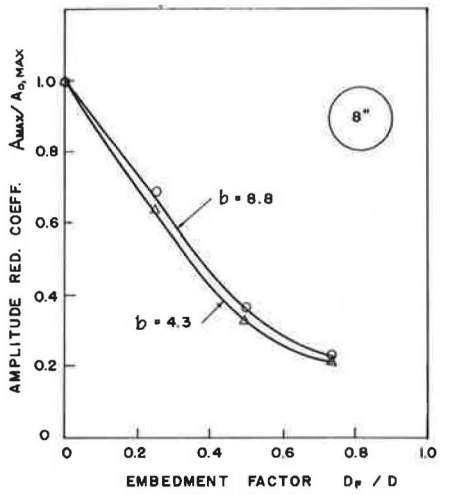

Figure 9. Amplitude reduction coefficient versus embedment factor for 8-in. diameter footing.

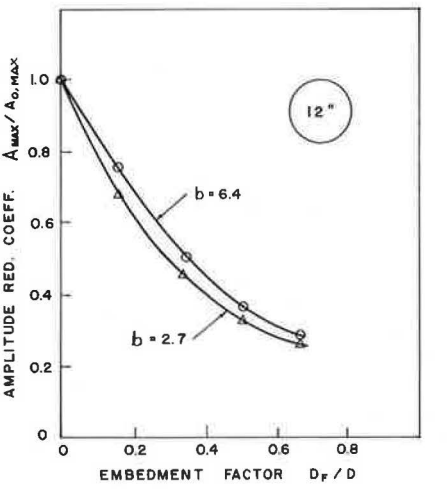

Figure 10. Amplitude reduction coefficient versus embedment factor for 12-in. diameter footing.

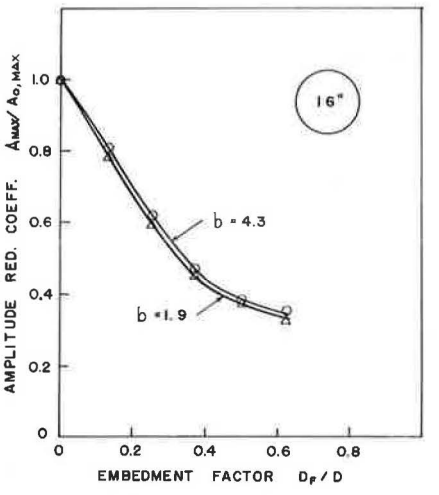

Figure 11. Amplitude reduction coefficient versus embedment factor for 16-in. diameter footing.

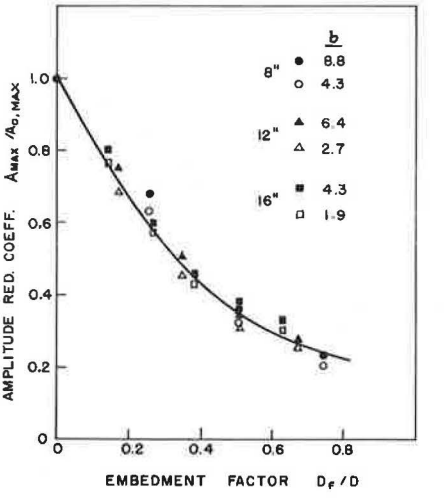

Figure 12. Amplitude reduction coefficient versus embedment factor for all circular footings.

expressed, for a quick approximate calculation, as a function of the embedment factor as

$$R_f = 1.0 - 1.25\left(\frac{D_f}{D}\right) \tag{5}$$

Then the maximum amplitude of an embedded footing can be determined from the following relationship:

$$A_{max.} = R_f \cdot A_{o,\,max.} = \left[1.0 - 1.25\left(\frac{D_f}{D}\right)\right] A_{o,\,max.} \qquad (6)$$

CONCLUSIONS

The essential conclusions to be derived from the experimental investigation may be summarized as follows:

1. The maximum amplitude of motion of an embedded footing is greatly reduced by the additional shearing resistance along sides of the footing. The reduction gets generally greater with increasing embedment depth. The rate of decrease becomes smaller, however, as the depth of embedment is increased. Embedment does not significantly change the resonant frequency resulting from a greater mass associated with the footing vibration.
2. The maximum amplitude is greater for the system having a higher mass ratio. The effect of mass ratio becomes smaller, however, with increasing embedment depth.
3. The effect of embedment for square and rectangular footings is similar to that for circular footings having the same mass ratios.
4. The amplitude reduction coefficient, which is the ratio of amplitude of the footing embedded to that at the surface, is independent of the mass ratio when plotted as a function of the embedment factor, which is the ratio of embedment depth to the diameter of the footing.
5. The amplitude reduction coefficient may be empirically expressed in terms of embedment factor.

ACKNOWLEDGMENTS

The author wishes to acknowledge the encouragement and assistance of M. L. Granstrom, Chairman of the Civil Engineering Department at Rutgers, who provided the laboratory facilities for this research. The author's appreciation is also extended to the Rutgers Research Council for a faculty research grant. Special thanks are also given to Y. C. Chiang who conducted the laboratory tests.

REFERENCES

1. Arnold, R. N., Bycroft, G. N., and Warburton, G. B. Forced Vibration of a Body on an Infinite Elastic Solid. Jour. Appl. Mech., Trans. ASME, Vol. 77, 1955, pp. 391-400.
2. Chae, Y. S. Dynamic Pressure Distribution at the Base of a Rigid Footing Subjected to Vibratory Loads. U. S. Army Engineer Waterways Experiment Station, Vicksburg, Miss., Contract Rept. No. 3-88, May 1964.
3. Chae, Y. S. The Material Constants of Soils as Determined From Dynamic Testing. Proc. Symposium on Wave Propagation and Dynamic Properties of Earth Materials, Univ. of New Mexico, Aug. 1967.
4. Chae, Y. S. Vibration of Noncircular Foundations. Jour. Soil Mech. and Found. Div., ASCE, Nov. 1969, pp. 1411-1430.
5. Fry, B. Development and Evaluation of Soil Bearing Capacity. U. S. Army Engineer Waterways Experiment Station, Vicksburg, Miss., Tech. Rept. No. 3-632, July 1963.
6. Hertwig, A., Fruh, G., and Lorenz, H. Die Ermittlung der für das Bauwesen wichtigsten Eigenshaften des Bodens durch erzwungene Schwigungen. DEGEBO, No. 1, J. Springer, Berlin, 1933.
7. Jones, R. In-Situ Measurement of the Dynamic Properties of Soil by Vibration Method. Geotechnique, March 1958, pp. 1-21.
8. Lysmer, J., and Richart, F. E., Jr. Dynamic Response of Footings to Vertical Loadings. Jour. Soil Mech. and Found. Div., ASCE, Jan. 1966, pp. 65-91.

9. Reissner, E. Stationare, axialsymmetrische, durch eine schuttelunde Masse erregte Schwigungen eines homogenen elastischen Halbraumes. Ingenieur-Archiv, Vol. 7, 1936, pp. 381-396.
10. Richart, F. E., Jr. Foundation Vibrations. Trans. ASCE, Vol. 127, Part I, Aug. 1962, pp. 863-898.
11. Richart, F. E., Jr., and Whitman, R. V. Comparison of Footing Vibration Tests With Theory. Jour. Soil Mech. and Found. Div., ASCE, Vol. 93, No. SM6, Nov. 1967, pp. 143-168.
12. Sung, T. Y. Vibrations in Semi-Infinite Solids Due to Periodic Surface Loading. Symposium on Dynamic Testing Soils, ASTM Spec. Tech. Publ. 156, 1953, pp. 35-63.

Control and Performance During Construction of a Highway Embankment on Weak Soils

VICTOR ELIAS and HERBERT STORCH, Storch Engineers

•METHODS of controlling embankment construction over compressible and weak foundations to ensure safety against shear failure along a circular arc are described in this paper. The design and construction performance of a highway embankment constructed in Revere, Massachusetts, on Interstate 95 by the Massachusetts Department of Public Works over deep compressible deposits of Boston Blue Clay are described, with emphasis on the methods of construction control used to ensure stability against circular shear-type failures during construction.

The use of a recently developed ICES computer program to compile construction control charts based on effective stress stability analyses, which relate the factor of safety to the measured pore pressures, is presented, and assessment is made of its value. Detailed results of site measurements of excess pore pressure, settlement, and horizontal deformations are presented to indicate the magnitude and value of these measurements in controlling the rate of construction and in delineating areas in which remedial measures are warranted. A comparison between predicted and measured excess pore pressures is made to assess the applicability of some current theoretical methods of analysis in predicting stability of embankments by the effective stress method. Conclusions are drawn on the applicability of the effective stress method of stability analysis used in conjunction with on-site pore pressure measurements to compile field control charts for use in controlling the rate of embankment construction.

THE SITE AND SOIL CONDITIONS

The portion of Interstate 95 described is part of the federally assisted Interstate Highway Program being constructed north of Boston in a low tidal swamp area. The project, approximately 2.3 miles long, begins at the existing Cutler Circle in Revere, Massachusetts, and ends at the Saugus River in the town of Saugus, Massachusetts. The project consists of a moderately high embankment that will carry eight lanes of traffic. The roadway was designed and is being constructed by the Massachusetts Department of Public Works.

The entire roadway alignment is located in the low tidal swamp area that is roughly bisected by the Pines River. Existing ground elevations average +5 (U.S. Geologic Survey), and the entire project area is subject to tidal inundations. Borings disclosed that the entire site (Fig. 1) was covered with a surface deposit of brown fibrous peat, sometimes underlain by soft organic silt, with a total thickness ranging from 2 to 26 ft. Below this level, loose to medium-dense, gray, silty, medium to fine sand deposits were encountered ranging in thickness from 2 to 30 ft.

Underlying the sand, a thick stratum of inorganic clay known as Boston Blue Clay was encountered, varying in consistency and color from stiff and light gray at the top to very soft and blue-gray. This clay stratum varies in thickness from a minimum of 30 ft to a maximum of 180 ft within the proposed areas of construction. Below the clay a thin mantle of dense, gravelly, glacial till and gray shale bedrock was encountered at depths ranging from 90 to 204 ft.

Paper sponsored by Committee on Embankments and Earth Slopes.

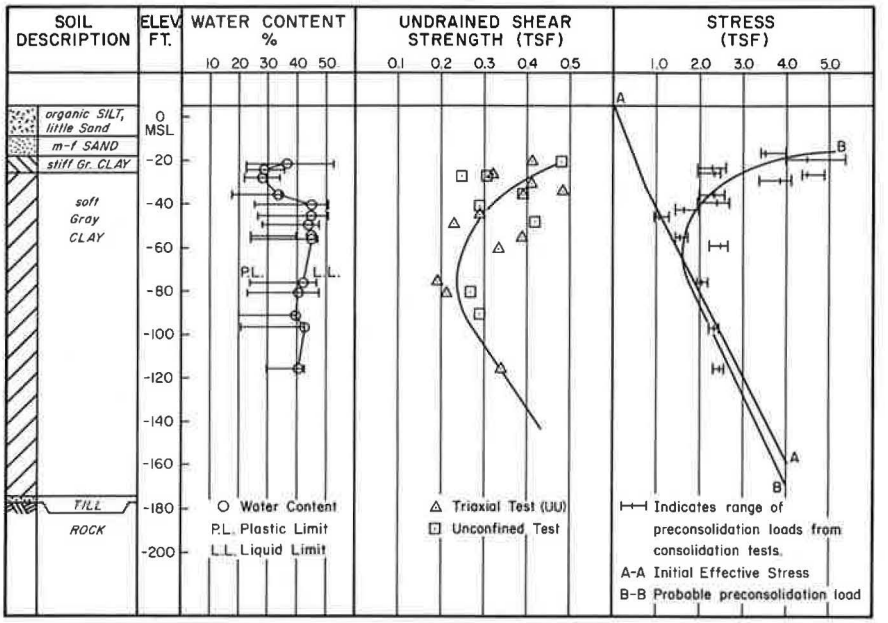

Figure 1. Geotechnical data.

SOIL PROPERTIES

Laboratory testing was performed to determine the shear and compressibility characteristic of the deep blue clay deposit. The blue-gray clay is inorganic and occasionally stratified, with thin lenses of silt and sand throughout. The lower moisture contents and shear planes produced by desiccation in the upper portions of the clay stratum indicate it to be overconsolidated (O.C.) at least to an elevation of -50. Shear and compressibility characteristics obtained from results of laboratory triaxial and standard oedometer tests are given in Table 1.

The measure of compressibility given in Table 1 applies for the virgin portion of the consolidation curves only. In the O.C. clays the recompression index (C_R) averaged 0.075. Time-settlement relationships were studied both from laboratory relationships (log-time method) and by evaluation of past performance of a nearby 400-ft-long test embankment constructed in 1957. The modulus of elasticity (E_S) of the composite clay stratum was back-figured by comparing the field settlement records obtained from the initial stages of consolidation at the 1957 test embankment. Based on this approach, a composite modulus of approximately 7,000 psi was obtained.

The friction angle at maximum obliquity in terms of effective stress and the variation of pore pressure parameter (A_f) with O.C.R. ratio was studied from a series of consolidated undrained triaxial tests with pore pressure measurements.

TABLE 1

AVERAGE SOIL PROPERTIES, BOSTON BLUE CLAY

Soil	$\frac{Cc}{1+e_o}$	$\frac{Cv}{\frac{f2}{day}}$	Su (psf)	$\bar{\phi}$ (deg)	$\bar{c}$ (psf)	AF	O.C.R.
O.C. clay	0.10-0.18	0.15	1100-600	23	400	-0.1 to +0.5	6 - 1
N.C. clay	0.18-0.24	0.40	500-800	26	0	0.75	1

DESIGN CONSIDERATIONS

The use of embankments throughout necessitated an evaluation of the settlement to be expected from the compression of the deep deposit of clay. The compression of the surface peat was not considered, as its removal was decided on at the inception of the project. Settlement studies by oedometer methods modified by the inclusion of immediate settlement, as suggested by Skempton, indicated a range of settlements to 3.5 ft over a period of up to 25 years. The magnitude and rate of settlement at the end of construction were estimated at 4 to 8 in. per year and were deemed unacceptable.

Studies were undertaken to determine procedures that would cause settlements to occur prior to final grading and paving and would keep the continuing long-term settlement within tolerable limits. The use of surcharge or overloads for periods of up to 2 years prior to pavement construction to induce settlements was adopted as the most economical method, in view of the anticipated reuse of the surcharges for the construction of a future interchange within the work limits. Analysis of surcharge requirements indicated the need of surcharge up to 23 ft to induce the desired settlements within the required time.

Stability analyses of these high surcharged embankments, based on total stress methods utilizing unconsolidated undrained triaxial test (UU) and unconfined compression test (U) shear strengths, indicated a factor of safety varying between 0.75 and 0.9. Based on these low calculated factors of safety, effective stress analyses were made to better understand the relationship of pore pressure generation and dissipation on the safety of construction and to take advantage of higher shear strengths indicated by CU tests. For these computations, pore pressures were predicted by the relationship proposed by Skempton:

$$\Delta U = \Delta\sigma_3 + A(\Delta\sigma_1 - \Delta\sigma_3)$$

with stress increments computed by elastic theory and the pore pressure coefficient (A_f) obtained by laboratory methods. The response of pore pressure to load ($\overline{PPR}$), defined as the ratio of instantaneously generated pore pressure to the vertical pressure increment at a given load, was then modified to reflect the dissipation of pore pressure during construction, as given in Table 2.

Stability analyses for embankments to elevation +40 based on these pore pressure relationships and effective shear strength parameters indicated a factor of safety ranging from 0.95 to 1.05. Based on these results, it was concluded that construction was feasible if sufficient construction control by in situ instrumentation was provided for and if provision was made in the contract for a controlled rate of fill placement as well as the inclusion of requirements for stabilizing berms and waiting periods, the need and extent of which would be determined in the field during the progress of construction.

FIELD INSTRUMENTATION

Instrumentation was selected to measure horizontal and vertical movements as well as piezometric pressures at the centerline of embankments. Open, porous tube, Casagrande-type piezometers were selected to measure centerline foundation pore pressures and were installed at 20 locations, each generally having three piezometers at various depths. Prior use of Casagrande piezometers in the Boston area established that the developed time lag was tolerable when used for large fill projects. In addition, their lack of hardware, gages, etc., above ground makes them suitable for installation in urban areas where the incidence of vandalism is very high. The inclinometer selected was the Wilson slope indicator. The inclinometer casing, in 5-ft sections, was jointed together with telescoping couplings, attached by four hollow rivets that would

TABLE 2

RATIO OF PREDICTED PORE PRESSURE RESPONSE ($\overline{PPR}$) TO LOADING

Embankment Elevation (+ M. S. L.)	O. C. Clay	N. C. Clay
20	0.54	0.63
30	0.51	0.60
40	0.49	0.57

break under a weight of approximately 250 lb and allow the casing to slide within each joint for a maximum distance of 6 in. per joint. Casings through the clay strata and into the glacial till were installed at cross sections, each section having four casings.

Settlement plates consisting of 4 ft by 4 ft steel plates with 2½-in. riser pipes welded to the plate were installed at the bottom of the excavation. Settlement anchors or plugs designed to measure the incremental settlement of the clay were installed at three locations, each location consisting of three anchors embedded at various depths. The anchors were of the Borros type. Displacement stakes of a simple crossarm design were installed at regular intervals near the toe of the embankment and at a distance of approximately 100 ft from the toe.

Settlement, piezometric levels, and horizontal deflection patterns occurring laterally from the centerline were monitored at a separate instrumented research section within the project under the direction of the Massachusetts Institute of Technology. The problem of data acquisition, management, storage, and immediate evaluation was partially solved by the placement of a small electronic computer in the field office to perform all repetitive and programmable computations. The time-consuming slope-indicator computations were performed in the field office on an Olivetti Underwood Programa 101 computer at the end of each day, and results were plotted the next morning. The stability analyses were updated weekly or as necessary by use of commercially available IBM 306/75 computers, where new input could be entered by telephone from the field office.

The total cost of the instrumentation was approximately $170,000, not including the cost of the research section. Instrumentation installation was made a part of the general construction contract.

EMBANKMENT CONTROL CRITERIA

The embankment instrumentation at this site was installed primarily to control the rate of filling, ensure safe construction, and determine the need for counterweight berms. The secondary objective was to monitor the long-term settlement behavior of the foundation in order to determine the appropriate time of surcharge removal.

Where the stability of embankments is marginal and successful completion of the project is dependent on the increase of shear strength resulting from the partial dissipation of pore pressure, it is essential that the rate of construction be closely controlled using the results of field measurements. For this approach to be used effectively, it is necessary to prepare in advance a set of control charts that directly relate the calculated factor of safety to the measured excess pore water pressures for the given height of embankment. These analyses were performed by computer methods using the commercially available version of the ICES lease program that uses an approximate form of the limit equilibrium approach as developed by Bishop to estimate the factor of safety of a slope or embankment. It also computes the factor of safety by the Fellenius method of slices, which serves as a first approximation for the Bishop method.

Circular arc effective stress analyses, using the ICES computer program, studied stability as a function of the pore pressure ratio R_u = (pore pressure/vertical total stress) in conjunction with soil strength parameters obtained by laboratory investigations. The lateral distribution of pore pressures can be represented by dividing the foundation into a number of zones within which the excess pore pressure is equal and is related to the excess pore pressure under the centerline by a factor determined by theoretical calculations or field measurements. Typical lateral distribution measured at the research section for the N.C. clays is shown in Figure 2.

The initial computations were made when the embankments had reached about half of their final height and at which time the pore pressures and their lateral distribution had developed a recognizable pattern. The early pore pressure data, in addition, indicated that the embankments could be idealized by two typical sections differentiated by the thickness of the in situ sand layer above the clay foundation. The critical section, having the thin natural sand layer, was characterized by higher pore pressures and larger vertical and horizontal deflections under the same load. Details of the

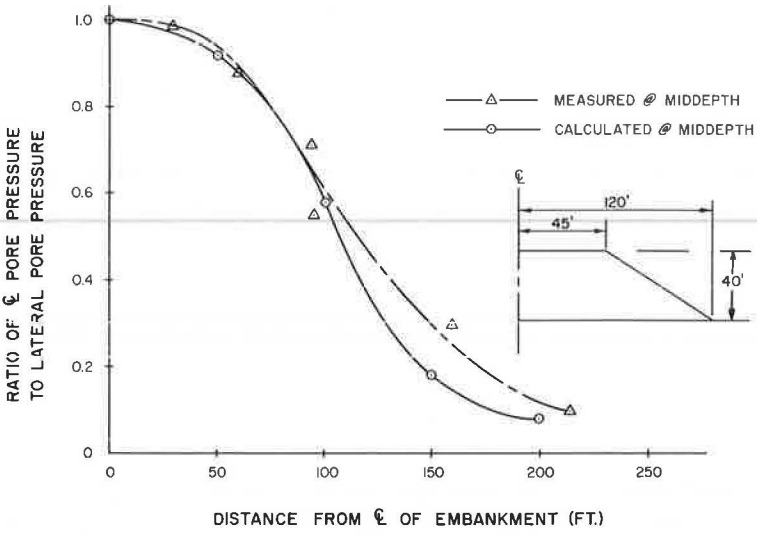

Figure 2. Lateral distribution of pore pressure, N.C. clay.

parameters used for a typical stability analysis for this critical section are shown in Figure 3.

In order to interpret the results of the stability analyses summarized in Figure 4 in a manner most useful for field control procedures, it was necessary to select a value below which the factor of safety would not be permitted to fall during construction. Because of local foundation variations and questions of applicability of this method

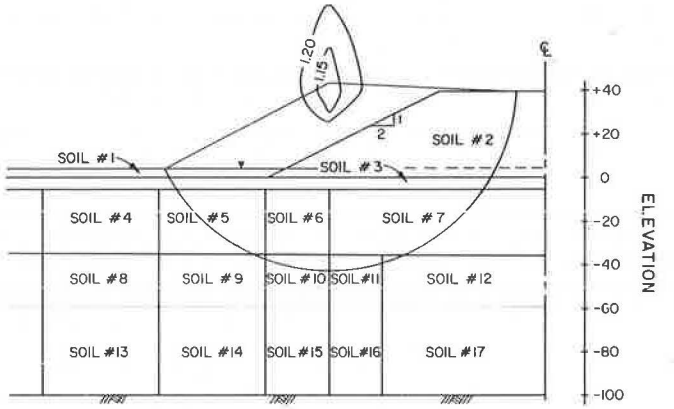

SOIL #	TYPE	γ	$\bar{\phi}$	$\bar{c}$	R_u
1	PEAT	75	0	0	2 *
2	FILL	130	33	0	2 *
3	SAND	125	33	0	2 *
4	O.C. CLAY	115	23	400	0.64
5	"	115	23	400	0.98
6	"	115	23	400	0.78
7	"	115	23	400	0.37
8	N.C. CLAY	115	26	0	0.70
9	"	115	26	0	0.89

SOIL #	TYPE	γ	$\bar{\phi}$	$\bar{c}$	R_u
10	N.C. CLAY	115	26	0	0.79
11	"	115	26	0	0.69
12	"	115	26	0	0.67
13	"	115	26	0	0.64
14	"	115	26	0	0.76
15	"	115	26	0	0.71
16	"	115	26	0	0.65
17	"	115	26	0	0.65

* CONVENTION FOR WATER TABLE.

Figure 3. Typical stability analysis.

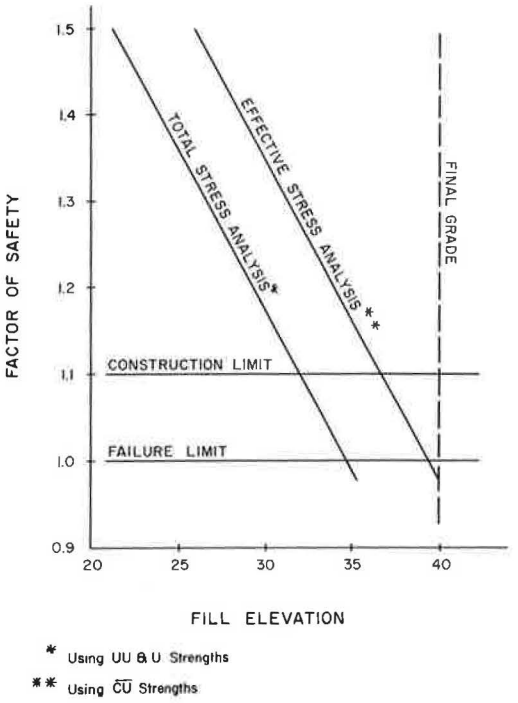

Figure 4. Summary of stability analyses.

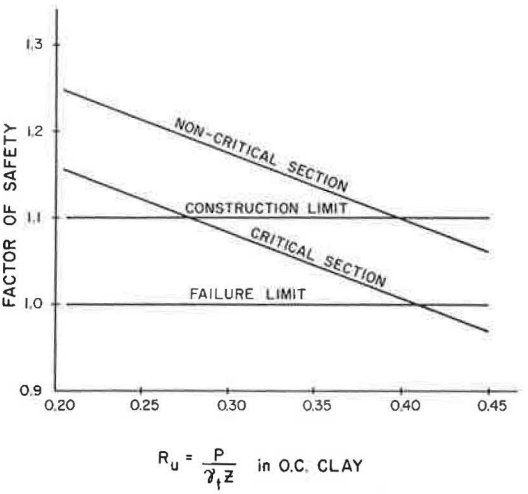

Figure 5. Effect of pore pressure variation on the factor of safety for a typical 40-ft embankment.

of analysis at a failure condition, the lowest limit for a construction factor of safety was established at 1.1.

Examination of these initial stability charts indicated that this limit might occur when embankments reached an approximate elevation of +35 or 5 ft short of completion. Study of the failure circles for these heights indicated that the critical circles were largely affected by the pore pressure in the O.C. clays and that control in this zone within tolerable limits would ensure safe construction. Additional stability studies were undertaken for embankments to an elevation of +35 and +40 in which the pore pressures in the O.C. clay were varied to determine the maximum pore pressure permissible during construction.

The resulting typical control chart for embankments to final elevation is shown in Figure 5, in which the factor of safety is plotted as a function of the pore pressure ratio R_u. By use of these charts, field personnel were able to immediately interpret the measured pore pressures and decide whether the factor of safety was sufficient to permit additional lifts to be placed. In addition to the control exercised by pore pressure devices, settlement plate and inclinometer data were used during construction in delineating problem areas.

EMBANKMENT PERFORMANCE

Construction at the site began in the summer of 1967, continued through the winter of 1967-68, and was halted for the winter of 1968-69 at a time when embankments had reached an approximate elevation of +35. After complete excavation of the surface organic soils, fill brought to the site by railroad from New Hampshire was placed in lifts not exceeding 1 ft at a rate of 1 ft per week.

The weekly rate of fill placement from May to November 1968 averaged 125,000 cu yd per week, which was the practical limit for this operation. The total anticipated volume of fill for the project was approximately 3,700,000 cu yd, and an allowance for 800,000 cu yd for stabilizing berms was provided for on a contingency basis.

The rates of pore pressure generation and dissipation for typical cross sections are shown in Figures 6 and 7. Because the rates of pore pressure generation at the various

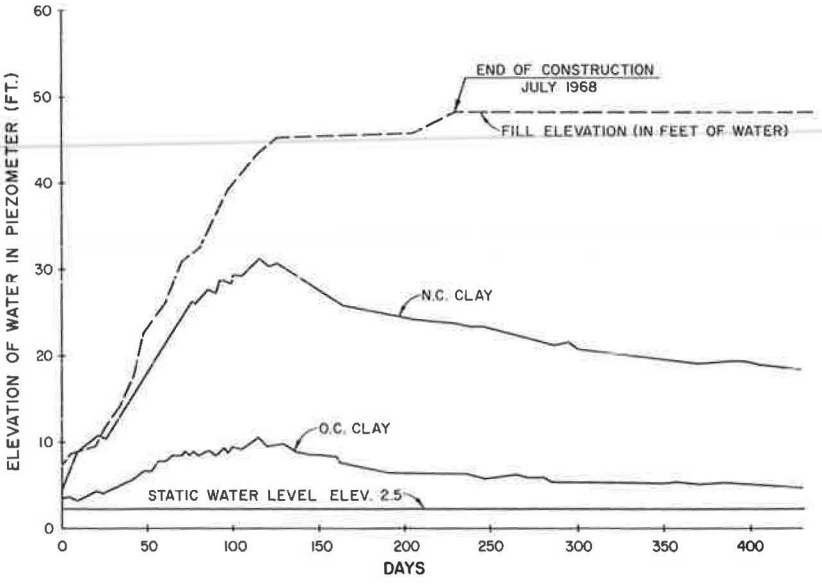

Figure 6. Measured pore pressures for a low embankment.

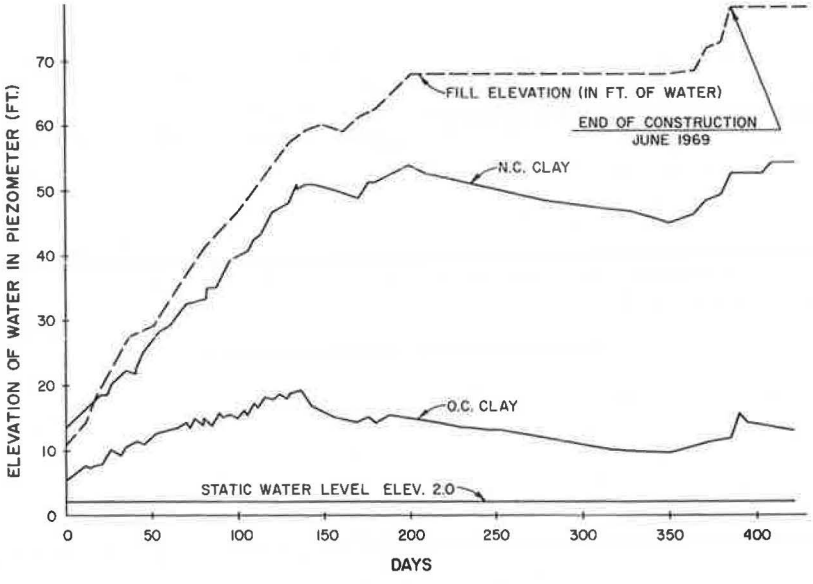

Figure 7. Measured pore pressures for a high embankment.

cross sections were fairly constant, it was possible to relate the increases in maximum pore water pressures to the corresponding increases in loading with some degree of accuracy throughout the construction phase. These relationships are given in Table 3 as factors showing the measured pore pressure response to loading ($\overline{PPR}$) at various stages of construction. Lateral distribution of pore pressures monitored in detail at the research section yielded consistent data.

TABLE 3

RATIO OF MEASURED PORE PRESSURE RESPONSE TO LOADING

Embankment Elevation (+ M.S.L.)	O.C. Clay	N.C. Clay
15	0.20 ± 0.10	0.57 ± 1.10
20	0.20 ± 0.10	0.56 ± 0.10
25	0.21 ± 0.10	0.57 ± 0.10
30	0.18 ± 0.15	0.54 ± 0.10
35	0.17 ± 0.15	0.62 ± 0.10
Average	0.19 ± 0.12	0.57 ± 0.10

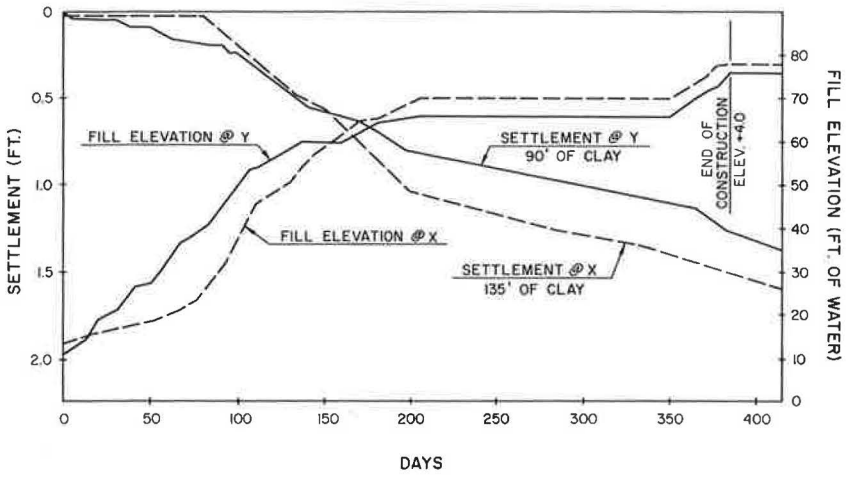

Figure 8. Measured settlement according to settlement plates.

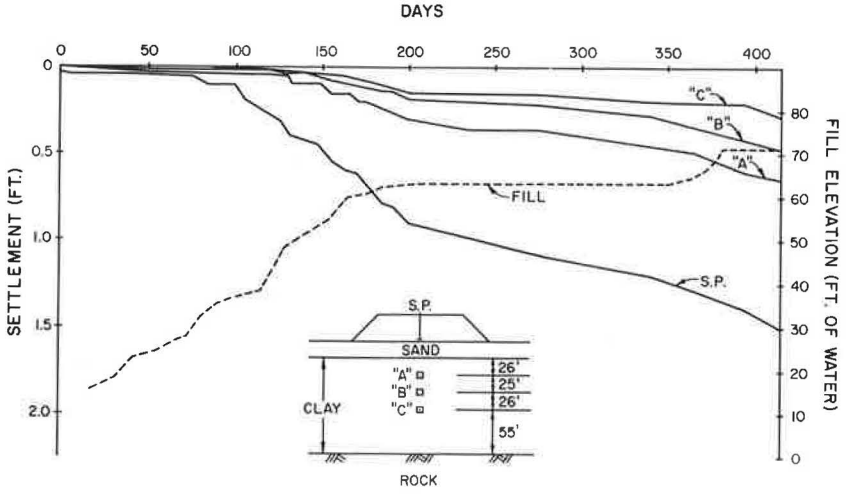

Figure 9. Measured settlement at a settlement anchor.

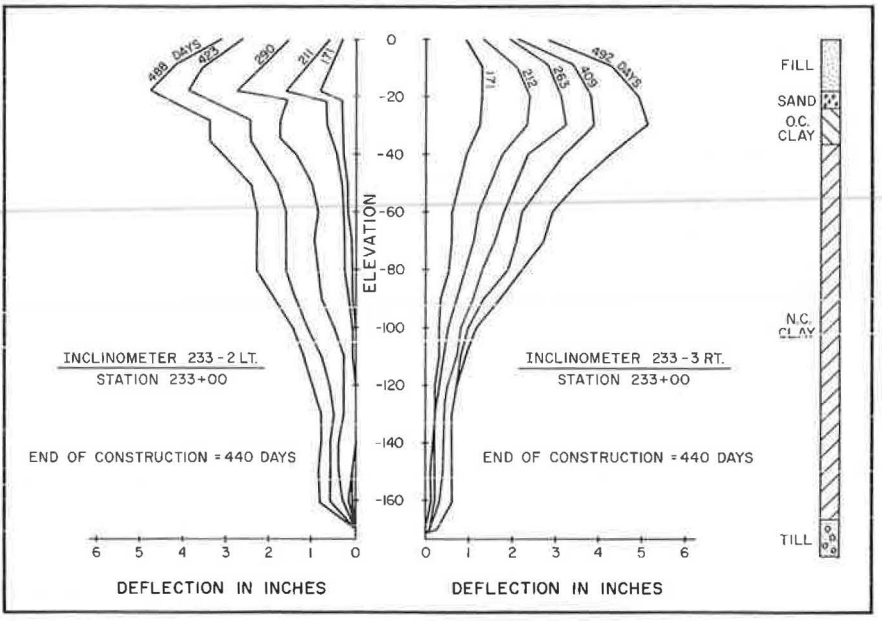

Figure 10. Measured deflections for a high embankment.

Surface settlements were measured by settlement plates at the centerline throughout the project. Typical settlements of embankments constructed over various depths of compressible clay are shown in Figure 8. The incremental settlement measured at a typical settlement anchor is shown in Figure 9. Horizontal deflections were measured as soon as the settlement plates indicated vertical movements. Typical horizontal deflections measured are shown in Figure 10.

Embankment construction proceeded until November 1968 when embankments had reached an approximate elevation of +35. At this time the measured pore pressures were high enough to indicate that the factor of safety was about 1.1 and that continued construction would unnecessarily jeopardize the embankments.

Sufficient pore pressure dissipation over the major portion of the project occurred in the winter of 1968-69 to allow reopening of the project in the spring of 1969 and continue it to completion in July 1969.

In one area approximately 800 ft long, very little dissipation occurred in the O.C. clays, and significant rises of pore pressure were recorded in the piezometers placed in the N.C. clays during a period of no construction acitivity. In addition, both settlement and lateral deformation on the west side of the embankment proceeded at rates approximately twice as great as elsewhere on the project. Therefore, prior to resumption of full-scale construction, a small stabilizing counterberm 75 ft wide and approximately 10 ft high was placed on the west side only.

SUMMARY AND DISCUSSION

The primary objectives were to monitor construction, to control the rate of filling in such a manner as to prevent instability, and to minimize the use of counterberms. The tools used to assess the factor of safety were the measured excess pore pressures at the centerline of the embankments, and it was of little practical concern during construction how they were produced.

Comparison between the predicted pore pressures (Table 2) and the measured pore pressures (Table 3) indicates that use of Skempton's proposed relationship, with

stresses computed by the usual elastic methods, overestimates the pore pressure generated in the O.C. clays and generally gives a fair assessment of generated pore pressures in the N.C. clays at significant depths below the loaded surface.

Recent work by Christian on undrained stress distribution utilizing finite element techniques suggests that horizontal stresses are significantly affected by drainage conditions and that analyses of foundation behavior dependent on horizontal stresses not conforming to the actual partial drainage case would overestimate the magnitude of these stresses. This assessment qualitatively explains the overestimation of horizontal stresses at relatively shallow depths in proximity to the loaded area, where significant drainage and consolidation during construction occurred.

It has been known for some time that horizontal movements often develop in conjunction with vertical subsidence. No reliable method of predicting the total magnitude and allowable horizontal deflections for embankments has been advanced. Previous work by Gould proposed a method of converting axial strains from laboratory triaxial data to shear strains on a failure plane assuming that volume changes are negligible. On that basis it was calculated from laboratory data that the failure strain in the in situ O.C. clay would be limited to about 10 in. Measurements of horizontal strain for embankments constructed to an elevation of +40 yielded an average maximum of 5 in. of lateral strain during construction except for one potentially unstable area where over 7 in. of strain were measured when the embankment had reached an elevation of +32. To preclude further strains a stabilizing berm previously described was constructed prior to placement of additional fill. The settlement anchors were most useful in isolating the seat of settlement during construction and showed that the major settlement took place in the upper O.C. clays. The magnitude of the settlement measured to date indicates that the conventional settlement analyses overestimated the probable total settlement by almost 100 percent.

The settlement plates, inclinometer casing, and Borros-type settlement anchors performed well during construction. The displacement stakes yielded no measurable data. The open-type Casagrande piezometers performed well only in areas of minimal settlement. Where significant settlements (more than 6 in.) took place, the failure incidence approached 50 percent during construction. Recovery of a failed piezometer tip indicated that the failure occurred as a result of pinching and bending of the plastic riser pipe between the top of the sensing tip and the bottom of the casing that contained the seal. This failure mode could only have been caused by sufficient differential settlement between the tip, which settled relatively little in comparison to the casing, which was dragged down by much larger consolidation of the upper O.C. clays.

CONCLUSIONS

1. Based on experience with this project, it appears that effective stress methods of analysis, together with in situ measurements of pore pressures, provide an effective tool in controlling construction of embankments over soft strata and provide a realistic assessment of step-by-step stability.
2. Stability analyses utilizing shear strengths obtained by unconfined compression tests and unconsolidated undrained triaxial tests underestimated the calculated factor of safety of this embankment.
3. Settlement analyses by conventional oedometer methods seriously overestimated the measured settlement at this embankment.
4. The introduction of the ICES lease stability program provides a practical, fast, cheap, and effective method of analyzing the stability of embankments by means of construction control charts once pore pressure trends are established during the initial phase of construction.
5. The measurement during construction of lateral and horizontal movements in addition to pore pressures is a valuable tool in isolating potential problem areas where corrective steps may be warranted.
6. The instrumentation of foundation behavior and control during construction made possible the elimination of almost all of the planned stabilizing berms, resulting in a savings of almost $2,000,000.

7. It appears that measurements of pore pressures in foundation soils anticipated to settle significantly should be made by piezometers other than those of the conventional Casagrande type.

ACKNOWLEDGMENTS

The authors are indebted to the Massachusetts Department of Public Works and its engineering staff for complete cooperation throughout design and construction and for permission to publish field data from the I-95 Revere-Saugus project. Special recognition is due Robert Tierney, Engineer of Highways, Massachusetts Department of Public Works, for his contributions during the design phase and in reviewing this paper.

REFERENCES

1. Skempton, A. W., and Bjerrum, L. A Contribution to Settlement Analysis of Foundations on Clay. Geotechnique, Vol. 7, 1957.
2. Skempton, A. W. The Pore Pressure Coefficients A and B. Geotechnique, Vol. 4, 1954.
3. Henkel, D. J. The Shear Strength of Saturated Remoulded Clays. Research Conf. on Shear Strength of Cohesive Soils, 1960.
4. Storch Engineers. Soils and Foundation Report for Interstate Route 95, Revere-Saugus, Mass. Report to Highway Engineers, Inc., Boston, Mass., 1965.
5. Storch Engineers. Supplemental Soil and Foundation Report for Interstate Route 95, Revere-Saugus, Mass. Report to Highway Engineers, Inc., Boston, Mass., 1966.
6. Design Manual, Soil Mechanics, Foundations and Earth Structures. NAVDOCKS DM-7.
7. Gould, J. P. A Study of Shear Failure in Certain Tertiary Marine Sediments. Research Conf. on Shear Strength of Cohesive Soils, 1960.
8. Christian, J. T. Undrained Stress Distribution. Jour. Soil Mech. Div., ASCE, Vol. 94, No. SM6, 1968.

Photoelastic and Finite Element Analysis of Embankments Constructed Over Soft Soils

ROBERT L. THOMS and ARA ARMAN, Louisiana State University

The objective of this study was to determine displacements and stresses beneath embankments constructed over soft organic soils (muck) using experimental models and the finite element method. This study was motivated by the fact that embankments are frequently constructed over soft organic soils in southern Louisiana, and the analysis of such embankments is necessary in order to effect a possible savings in construction and maintenance costs. Stresses and displacements were determined experimentally and numerically for model embankments that underwent large deflections when constructed over models of trenched and untrenched soft soils. In the experimental phase of the study, grid and photoelastic methods were used to determine deformations and stresses in the model soil, which consisted of a soft gelatin mix with an embedded ink grid. A gelatin slab, which modeled a cross section of the soil supporting an embankment, was formed in a tank with glass sides. Model embankments were placed in the tank on the gelatin, and resulting grid deformations and photoelastic fringes in the gelatin were photographed.

In the numerical phase of the study, the finite element method was used to determine stresses and displacements in the soil. Experimental and numerical results for maximum normal and shearing stress along the centerline beneath the embankments were compared with results obtained by classical linear elasticity. For embankments undergoing large deformations, where analysis by the classical theory using small deformation restrictions and superposition principles is suspect, it was found that the stress values were bounded above by the classical solution in the case of maximum shear stress and were very close to those predicted by the classical solution in the case of normal stress.

It is concluded that the designer is conservative in using the classic Boussinesq approach in predicting both maximum shear stress and maximum vertical normal stress along the centerline and beneath an embankment undergoing large deformations. Where trenching is used, negative (upward) as well as positive (downward) displacements should be taken into account in estimating the area of the net cross section of an embankment. Trenching is not recommended for the placement of embankments on soft foundations unless (a) the trench is to be used as an economical waterway to transport bulk embankment material and equipment for the construction, or (b) the trenching operation will remove soft material and expose stiffer layers with higher bearing capacity. Untrenched embankment configurations produced no stress concentrations beneath the embankment.

•IN DETERMINING the state of stress beneath an embankment, it has been traditional to apply the linear theory of elasticity. The general assumptions made in the linear

Paper sponsored by Committee on Embankments and Earth Slopes.

theory of elasticity are that (a) the material is continuous, homogeneous, and isotropic; (b) the stress-strain relations are linear and obey Hooke's law; and (c) only small deformations occur.

Some obvious deviations from these assumptions occur in natural soils, especially in muck. Natural soils are not homogeneous; the compressibility of the soil in the foundation varies with depth. However, it was demonstrated that, in clays of moderate or high plasticity, the modulus of elasticity is practically independent of depth (1). Taylor (2) suggested that in many cases the variation of the stress-strain relations with regard to depth is not very large and the overall action is about the same as in the hypothetical case, in which the moduli of elasticity are constant and equal to the average value.

Stress-strain relations for soils are known to be frequently nonlinear. The usual procedure used in the analysis of such soils is to estimate an approximating "effective reaction" modulus.

Finally, the deformation occurring in soils can be quite large, thus violating the third assumption previously listed. In this case the stress state predicted by the linear theory of elasticity is obviously suspect to a degree determined by the magnitude of deformation occurring. Despite these violations of the basic assumptions of linear elasticity, this theory has been applied extensively with apparent good sucess (3).

This report presents the summary of work performed using models and a numerical analysis approach to determine the state of stress existing beneath an embankment placed on a soft soil such as muck. It was assumed throughout this study that finite deformations of the embankment could occur, and that the use of an effective reaction modulus was adequate for representing the material behavior of the soft soil.

REVIEW OF PAST WORK

Studies Based on Linear Elasticity

In 1885 Boussinesq derived a detailed and simple solution for determining the state of stress in a semi-infinite elastic isotropic solid subjected to a point load. Boussinesq's derivation has been perhaps the most frequently used solution for determining stress states in soils underlying embankments.

In 1920 Carothers (4) published solutions he developed for the stress distribution produced by triangular, trapezoidal, and terrace loading. Recently semi-empirical equations for evaluating the stresses in a nonhomogeneous foundation were presented by Huang and Zhang (5). Equations for stress in anisotropic soils were developed recently by Barden (6). Jurgenson (7) proposed a method for the analysis of embankment foundations that are homogeneous to an indefinite depth. Gilboy (8) proposed a method for the analysis of embankment foundations using Boussinesq's equations.

Perloff (9) recently analyzed embankments assumed to be continuous with the supporting soil by the complex variable technique of Muskhelishvili for linear elasticity. This work apparently represents the most complete analysis using linear elasticity to date. His analysis assumed the embankment and supporting soil to have the same material properties.

Experimental Studies Using Gelatin as the Model Soil

In constructing the models to be tested in this study, gelatin was used to simulate soft soil occurring in the natural state. In the area of soil mechanics problems, Farquharson and Hennes (10) were the pioneers with the first significant study using gelatin in conjunction with the method of photoelasticity.

In 1966 Richards and Mark (11) published the results of their work dealing with the use of gelatin for photoelastic studies of gravity structures. Their technique is general and has the capability of treating many interesting problems.

Review of the Finite Element Method

The numerical analysis phase of this study was based on the finite element method. The literature on applications of the finite element method is extensive, and the reader

is referred to works by Zienkiewicz and Cheung (12) and Przemieniecki (13) for a relatively complete survey through 1966. In the area of soil mechanics, the finite element method was applied by Clough (14), Zienkiewicz (12), Girijavallabham and Reese (15), and others. These studies, as well as Perloff's (9) exact solution by Muskhelishvili's methods, were restricted to the use of small deflection theory.

Finite element methods for the treatment of nonlinear problems involving large deflections have been presented and several laternate approaches are available. The method used in this study is due to Argyris (16) and involves applying increments of load in a sequence in order to keep the problem linear within any one loading increment.

Another source of difficulty is nonlinear material behavior. If time-dependent material behavior is significant, then the problem is complicated further. The determination of a realistic numerical representation of nonlinear time-dependent material behavior is a formidable task. This particular problem was not studied in this project.

DESCRIPTION OF THE MODEL STUDY

The model study consisted essentially of constructing a model of an embankment over muck. The model embankment was loaded and displacements and stresses were obtained. Then modeling laws obtained from dimensional analysis were used to predict qualitatively and quantitatively the characteristics of displacement and stress distributions. Gelatin was used to simulate muck in the model, and photoelastic and grid methods were used to determine stresses in the gelatin. Displacements were measured by using a grid system embedded in the gelatin.

Figure 1 shows the type of prototype embankments considered, along with a schematic diagram of a model representing the prototype. The model is based on certain idealizations of the prototype that will now be considered.

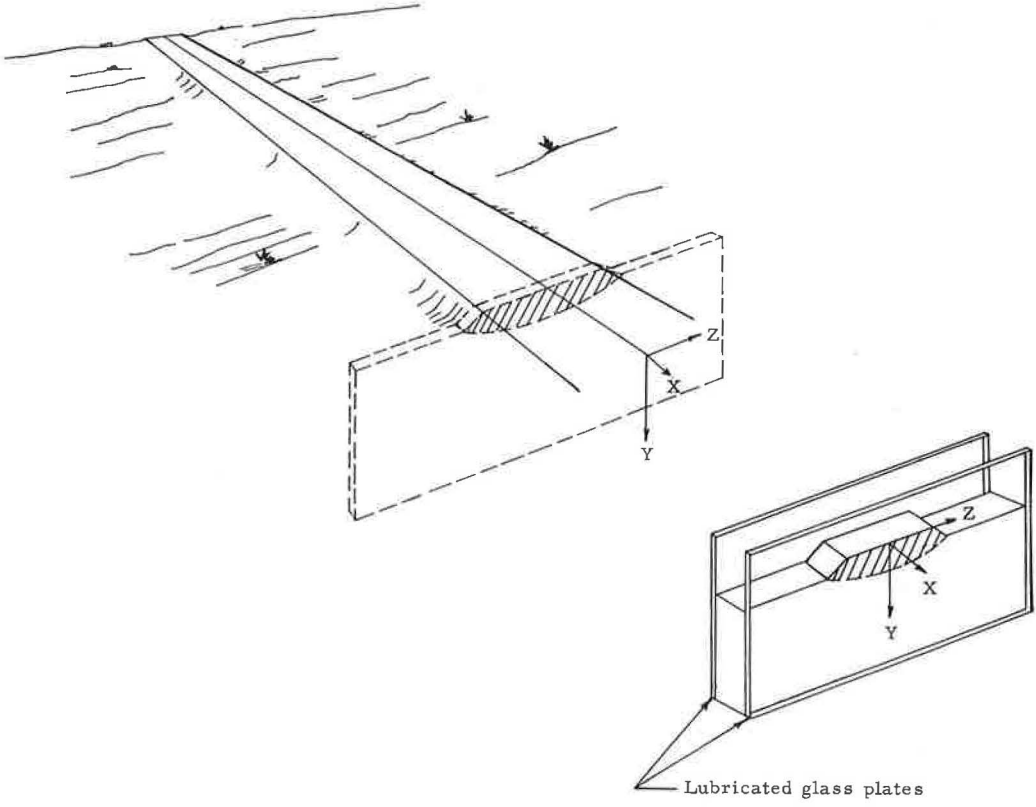

Figure 1. Idealized prototype embankment and model.

Assumptions Concerning the Actual Embankment

The following simplifying assumptions were made concerning the actual embankment (or prototype):

1. It was assumed that the muck was homogeneous in character and infinite in extent horizontally and semi-infinite vertically.
2. The embankment was assumed to be infinitely long with constant cross sections. Thus, the displacement of a typical cross section of the loaded prototype could be represented by the behavior of a slab of material constrained between two parallel lubricated plane surfaces (state of plane strain). Even in an actual prototype that varies with length, the typical cross sections at several stations could be represented approximately by appropriate models such as shown in Figure 1.
3. It was assumed that values of displacement and stress in the prototype were desired only after an initial significant displacement of the muck had occurred.
4. It was assumed that significant displacement of the muck occurred in a relatively short time after loading and that thereafter the embankment did not settle greatly. Hence, the variations of gelatin properties in the model with respect to time were considered to be a property of the model and were not correlated with variations of such properties with respect to time in an actual embankment. Essentially the prototype was assumed to have effective material properties that were independent of time.

It should be noted that the use of gelatin, which is essentially incompressible and viscoelastic, eliminated the possibility of considering model soil deformations resulting from consolidation and plastic flow.

Based on the foregoing assumptions, the following variables were assumed significant for geometrically similar embankments:

$$u = f(L, W, E, \tau, \mu) \tag{1}$$

The symbols are defined in the Appendix.

The value of Poisson's ratio was assumed to be the same in the model and prototype, i.e., $\mu = 0.5$. Consequently, the following dimensionless products were found by inspection of the remaining variables:

$$\frac{\mu}{L} = f\,\frac{E}{WL}, \frac{\tau}{WL} \tag{2}$$

The characteristic length L used was half the width of the crown c of the embankment. The following modeling laws were written using the dimensionless products given previously:

$$(u)_p = \frac{(c)_p}{(c)_m}\,(u)_m \tag{3a}$$

$$(\tau)_p = \frac{(Wc)_p}{(Wc)_m}\,(\tau_m) \tag{3b}$$

$$(E)_p = \frac{(Wc)_p}{(Wc)_m}\,(E_m) \tag{3c}$$

Description of Experimental Apparatus and Technique

Because a semi-infinite slab of soft soil loaded by body forces was being modeled, it was necessary to reduce the edge effects of the model boundary by building a tank that was large relative to the model embankments studied. A large model was also nec-

essary to reduce the difficulty of measuring strains resulting primarily from body-force loading.

The embankment and supporting soil models were formed in a steel-framed tank that was 3 in. wide and had clear glass sides 30 in. deep and 60 in. long (Fig. 2). Each of the glass walls was constructed of a 1-in. thick tempered glass plate on the outside and a $\frac{1}{4}$-in. stress-free glass plate on the inside. Sandwiched between the two glass plates was a sheet of Polaroid Corporation Circular Polarizing Material No. HNCP-37, 19 in. by 44 in. by 0.02 in. (Fig. 3).

Figure 2. Model casting and testing tank.

The two criteria used in developing a technique for embedding a grid in the model were to obtain a grid system that (a) would have well-defined lines with precise dimensions and (b) would not disrupt the characteristics of the gelatin either by adding strength to it or by reducing its strength.

The technique used was somewhat similar to that used by previous workers using an embedded grid method (17). A frame was fabricated of aluminum channels that would be inside the model tank. Holes were drilled at $\frac{1}{2}$-in. intervals in the channels so that a rectangular gridwork of taut nylon string could be suspended in the gelatin mix. After the mix solidified, ends of the string outside the tank were soaked in ink and the strings withdrawn. Traces of the holes were then left embedded in the gelatin for reference purposes.

Before the grid frame was placed in the tank, the tank was prepared for the gelatin solution. The inside of the tank was washed thoroughly with a mild detergent and warm water. Then a solution of water and zepherine chloride was applied to kill all existing bacteria that could attack the solidified gelatin. The sides of the tank were allowed to dry, and all inside surfaces were coated with Dow-Corning-7 Mold Release Compound to minimize the adhesion of the solidified gelatin to the glass. Following the preparation of the tank and the grid frame in the manner described, the grid frame was lowered into the tank and leveled in order to present a horizontal and vertical grid system.

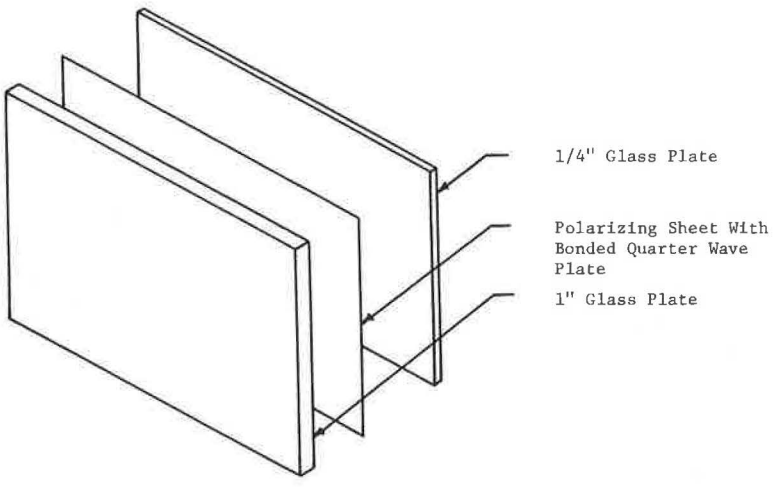

Figure 3. Arrangement of polarizing sheets in modeling tank.

The gelatin mix used to model muck was composed of powdered bone gelatin, glycerine, and sodium propionate (a preservative). The mixtures, weighing approximately 190 lb each, consisted of 5, 5½, or 6 percent gelatin (depending on stiffness desired), 5 percent glycerine, and 1 percent sodium propionate by weight, with the balance being water at 140 F. The solution was allowed to cool to 110 F before it was pumped into the tank.

A smaller tank, 8 in. wide, 10 in. long, and 1.53 in. deep, was manufactured using an aluminum frame and ½-in. thick Plexiglas walls. A ½-in. by ½-in. grid made of braided nylon line was strung across the aluminum channels of the frame through holes drilled in the center of the channels. This tank was designed to be used as a calibration specimen in conjunction with the model tank.

Both the embankment model tanks and calibration specimen tanks were filled with gelatin at the same time, were covered, and were kept in the same environment (an air-conditioned laboratory) until the gelatin had solidified and was ready for loading.

Construction of the Model Embankments

The model embankments were constructed of two different materials and were placed on two different foundation cross sections. Glass beads of the type used for striping paint were used to simulate cohesionless material, and models of embankments cut from solidified gelatin blocks were used to represent cohesive material.

The embankment models were placed on foundations simulating both on-grade and ditched cross sections. "Ditching" of the model soil was performed by placing in the gelatin a trapezoidal block of lubricated wood having the cross section of the desired ditch. The block was placed before solidification and was removed after solidification of the gelatin. Thus, a clear-cut, well-defined ditch was left in the foundation material.

Where glass beads were used, the loading was performed by pouring beads on the foundation in different manners, representing various loading or construction methods in the field. Model embankments were built in uniform layers or in concentrated loading sequences.

Where cohesive embankments were used, the block of gelatin, shaped as an embankment, was placed on top of the foundation in a single operation. The use of various loading techniques, foundation cross sections, and embankment materials yielded qualitative information concerning the construction sequence, the effect of geometrics, the effect of "ditching" operations, etc. In addition, similar information was obtained by placing berms on each side of the embankments.

THE CALIBRATION SPECIMEN

In order to relate the measured values of strain and the photographed isochromatic fringes to normal stresses and maximum shear stresses respectively, it was necessary to determine the values of the modulus of elasticity, E, and the model fringe value, f_σ. This was accomplished by the use of a calibration specimen.

The method of calibration was developed by Frocht (18) and Durelli (17) and later used by Richards and Mark (11). This method consists of placing on end in the polariscope a rectangular block composed of the same material as the model and measuring deformations and the locations of horizontal fringes. The block was cast flat and consequently the deformations and fringes resulting in the block when it was placed on end were due to the weight of the block itself. The specimen was confined between two parallel Plexiglas plates with spacers 1.53 in. deep. Thus, a state of plane strain existed. Silicone lubricants were used between the gelatin and the plates to ensure that friction did not affect the results.

The block deflected under its own weight. The vertical normal stress at any point in the gelatin was then determined by the equation

$$\sigma_y = \rho y \tag{4}$$

where ρ is the specific weight of the gelatin and y is the vertical distance from the top to any point where the stress is desired. A Cartesian x-y reference frame in the mid-

plane of the calibration specimen was assumed. Because $\sigma_x = 0$, i.e., the model was unconfined in the horizontal or x direction, the maximum shear stress was

$$\tau_{max} = \frac{\sigma_y}{2} = \frac{\rho y}{2} \tag{5}$$

Using the embedded grid, the strains ϵ_{xx} and ϵ_{yy} could be determined at any point. Because for this case the x and y axes were also the principal axes, the relationship between the maximum shear strain and the strains in the x and y directions was

$$\gamma_{max} = \epsilon_{xx} - \epsilon_{yy} \tag{6}$$

Therefore, the shear modulus was attainable from

$$G = \frac{\tau_{max}}{\gamma_{max}} = \frac{\rho y/2}{\epsilon_{xx} - \epsilon_{yy}} \tag{7}$$

Values of G were determined from data collected at several points within the calibration specimen and then averaged.

Then, the modulus of elasticity was found by the relationship $E = 2(1 + \mu)\, G$. The gelatin was assumed to be essentially incompressible, which implied $\mu = 0.05$. Therefore $E = 3.0\, G$.

The model fringe value was determined from basic equations relating shear stress to fringe order. From photoelasticity theory (18),

$$f_\sigma = \frac{2\tau_{max} h}{n} \tag{8}$$

The maximum shearing stress from Eq. 5 substituted into Eq. 8 yields

$$f_\sigma = \frac{\rho y h}{n} \tag{9}$$

Thus, for several values of y and the corresponding values of n, an average value of the model fringe value was obtained for one specific time and gelatin mixture.

DETERMINATION OF STRESS AND STRAIN

Methods of Determining Stress and Strain

The Lagrangian description of the engineering definition of strain was used throughout the study (21). Values of normal strain were obtained by using a 1-in. (undeformed) line segment for a reference length in the embedded grid in the gelatin model. It should be noted that the large size of the model permitted the use of a large reference length.

Because gelatin is incompressible ($\mu = 0.5$), it was not possible to determine explicitly normal stresses directly from normal strain in the plane strain case. For plane strain, assuming that Hooke's laws are valid,

$$\sigma_y = \frac{E(1 - \mu)}{(1 + \mu)(1 - 2\mu)} \left(\epsilon_y + \frac{\mu}{1 - \mu}\, \epsilon_x\right)$$

which becomes meaningless as $\mu \to 0.5$. However, the values of shearing stress (and effective stress) can be obtained by using measurements of the deformed grid and data from the calibration specimen.

The shear difference method (19) was used in conjunction with shear stress determined as noted previously to compute vertical normal stress at any point in the gelatin. The shear difference method is based on approximate integration of the equations of equilibrium, and no additional approximations are introduced for large strain analysis as compared to small strain analysis, provided that the final geometry of the deformed model is used. It should be noted that the shear difference method required an assumption on the "starting" value of the vertical normal stress at the surface of the gelatin. Away from the model embankment the vertical normal stress was obviously zero, but under the embankment it was assumed that the vertical stress was equal to the height of the embankment times the specific weight of the model embankment material. This is the assumption used in the classical solution for stress beneath embankments; however, some investigators have recently questioned this assumption.

Maximum shear stresses were also determined in the gelatin by using photoelasticity theory. The theory is essentially the same as discussed previously in the description of the calibration specimen, and involved photographing and analyzing fringes obtained through the loading of the birefringent gelatin "soil".

It was assumed that at any instant of time the time-dependent gelatin possessed the linear stress-strain relationship $\tau/\gamma = G$. This was justified by plotting a series of stress-strain curves at predetermined times for the calibration specimen. At any one time the curves were found to be linear, thus making it necessary only to photograph the model and to calibrate the specimen simultaneously in order to use the equation given.

Comparison of Stress Values

Figure 4 shows maximum shear stress values down the centerline beneath the model embankment as determined by the grid method and photoelastic method. The values obtained by each of the two experimental methods were in adequate agreement. Also shown is a plot of the maximum shearing stress as given by the solution of Boussinesq. The largest maximum shearing stress obtained experimentally was approximately 80 percent

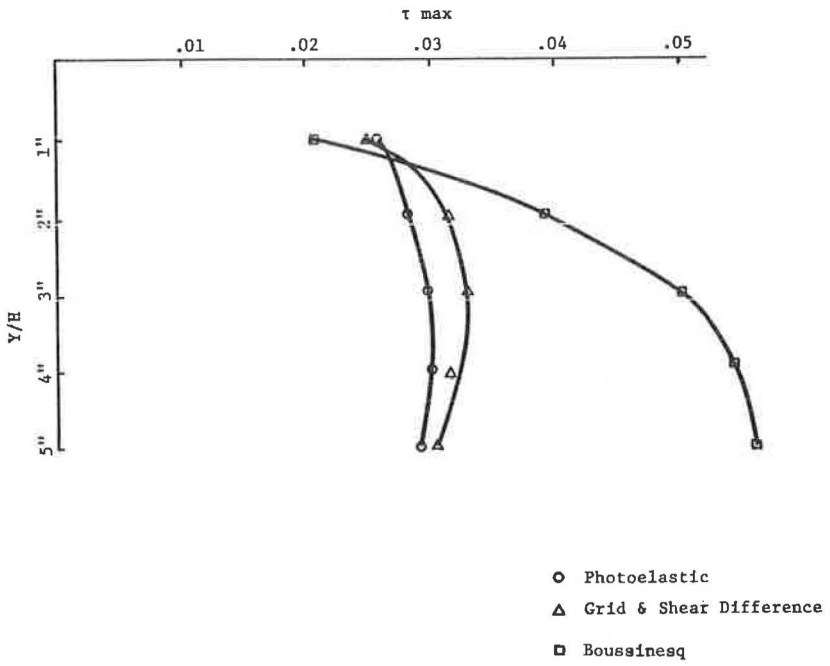

Figure 4. Theoretical and experimental stresses under an embankment.

smaller than the largest shearing stress obtained by the Boussinesq solution. However, while the Boussinesq solution is valid only for relatively small displacements (as would occur for stiff soils), the experimental results were obtained from work with simulated muck where large displacements have occurred.

Plots of superimposed grids before and after deformation for each of the three embankment types were studied. In addition, plots of values of vertical strain, as determined directly from the embedded deformed grid lines in the loaded gelatin model, were made. These plots, in addition to the plots of directions of maximum shearing stress at preselected discrete points and plots of vertical stresses as obtained by the shear difference method in conjunction with values of stress measured from the embedded deformed grid, were analyzed to correlate experimental values with values predicted by the classical linear theory of elasticity.

Thus, experimentally determined values of maximum shearing stress in soft soils beneath the center of the embankments appeared to be appreciably less (80 to 90 percent) than those predicted by the classical linear theory of elasticity that assumes only small displacements occur. On the other hand, maximum vertical normal stresses appeared to decrease less rapidly with depth beneath the model embankment that underwent large displacements.

Analysis by the Finite Element Method

A study was performed to test the feasibility of using the finite element method to analyze embankments constructed over soft soils where large displacements would occur. The effects of changes in geometry were accounted for by using the geometric stiffness matrix approach of Argyris (16).

The analysis necessary for the finite element method is phrased most conveniently in terms of matrix notation. The set of equations relating loads and displacements at the model points of the body can be written $[K]\{u\} = \{F\}$, where $[K]$ is a square matrix with the number of rows or columns equal to the number of displacement components in the finite element model of the body. Also, $\{u\}$ and $\{F\}$ are column matrices with the same number of rows. The matrix $[K]$ is referred to traditionally as the stiffness matrix, and the $\{u\}$ and $\{F\}$ matrices are referred to respectively as the displacements and force vector. The equation can be regarded as a set of linear algebraic equations involving the unknown displacements $\{u\}$, which can be solved by some appropriate method. With the displacements determined, it is possible to calculate approximate values of stress within any one element.

Because the scope of the numerical analysis of the study was limited to a feasibility study, details on the computer program employed have been omitted. The program employed can be used to account for large deformations and to represent a piecewise linear effective stress-strain relationship for the soil.

To verify the computer program written for this study, the finite element method was used to compute the deflections and stresses in a carefully controlled gelatin calibration specimen. The resulting computed deflection was then compared to the measured deflection of the actual calibration specimen. The material properties of the gelatin specimen were obtained and used in the numerical model of the same specimen. Agreement between the loaded configuration of the physical and numerical calibration specimens was excellent. A finite element analysis that did not take

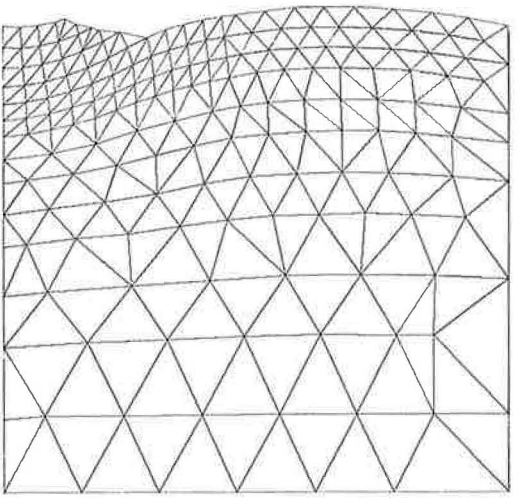

Figure 5. Finite-element model of embankment with total load.

into account large changes in geometry differed in deflections by approximately 15 percent from the plotted specimen shown. This justified considering the effect of large deformations.

The finite element method used in this study to analyze large deflections employed the technique of applying the load in increments. The problem was regarded as linear for each increment of load. The final configuration represented the accumulated effect of the incremental loadings. Figure 5 shows the final deflected configuration of a finite element model of an embankment in which the loading was applied in four increments.

Figure 6 shows plots of maximum shear stresses beneath the embankment down the centerline as computed by Perloff (9) and by the finite element method used in this study. Also shown are plots of maximum shear stress obtained by the experimental method used in the current study and plots of stress obtained by the Boussinesq solution (classical method). It is of interest to compare the various solutions to determine if the classical small deformation theory (Boussinesq, Perloff) yields results close to those predicted by taking large deformations into account.

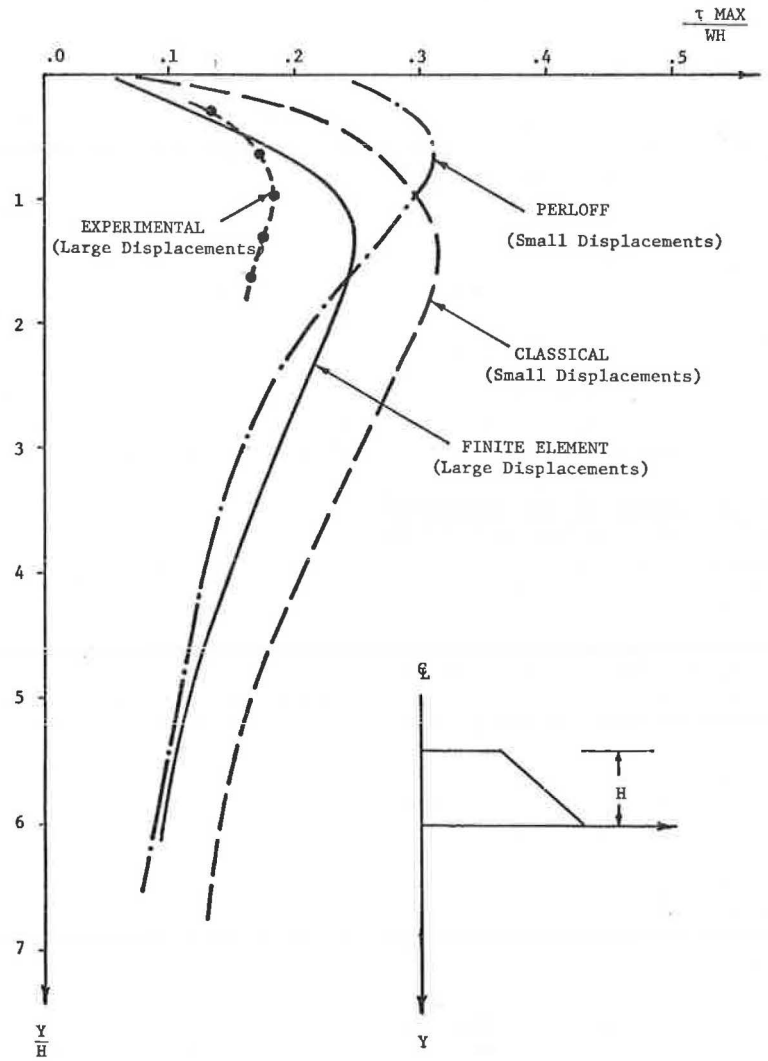

Figure 6. Maximum shear stress beneath embankment.

The finite element approach yields a maximum shearing stress value that is approximately midway between those values determined experimentally and those values determined by small-deformation methods. Using the finite element approach, the maximum stress is predicted to occur at a distance (measured in the undeformed material) beneath the embankment that is approximately equal to that predicted by the classical approach. The experimental method yields results that agree approximately with the finite element method until the experimentally determined maximum stress value is obtained; then the values diverge.

Figure 7 shows a plot of vertical normal stresses beneath the embankment down the centerline. Beneath the embankment the finite element solution is close to the classical assumption, and then it rapidly approaches Perloff's solution (9). The experimental solution for normal stress was "started" at the level of stress as calculated by the

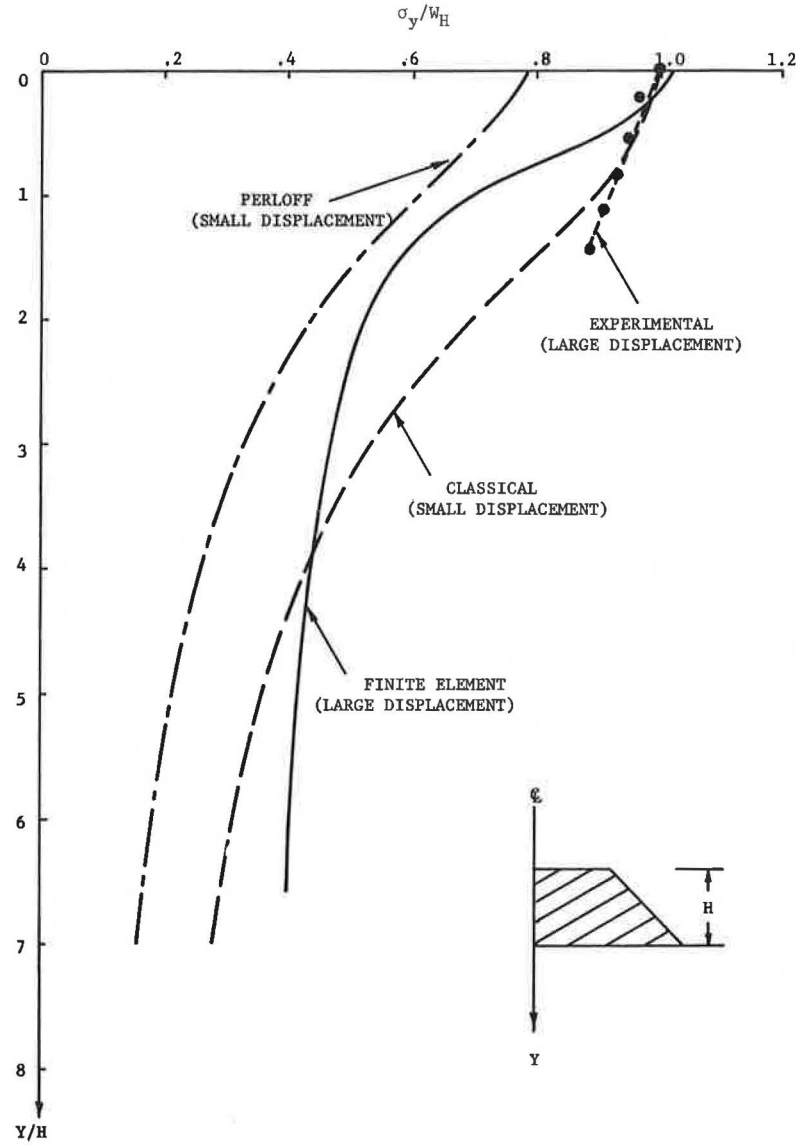

Figure 7. Vertical normal stress beneath embankment.

classical method. The shape of the plotted curve of the experimentally determined values apparently agrees more closely with the curve corresponding to the classical solution.

In summary, it appears that for embankments undergoing large displacements, the maximum shearing stresses beneath the embankment along the centerline are less than those predicted by small deformation theory methods. However, certain precautionary comments should be added. The shearing stress may well increase (from that predicted by small deformation theory methods) at other locations away from the centerline. Finally, the finite element study was preliminary in nature because it was essentially a feasibility study. Additional study of this method for cases where large time-dependent deformations occur is presently in progress.

QUALITATIVE ANALYSIS OF MODEL FOUNDATIONS

Loading tests performed on trenched and untrenched embankment foundations were analyzed for this study. Embankments with and without berms were loaded on both types of foundations, and the results of each of these tests were analyzed.

Qualitative Analysis of Trenched Foundations

Trenched model foundations were loaded with embankments both with and without berms as outlined previously. The following observations were made as a result of the analysis of these loading tests:

1. The initial trenching operation produced negative vertical displacements (upward) and accompanying negative stress conditions under the trench. These characteristics did not indicate any impending danger of failure. However, in the measurements of the final cross section of a trench in the field, they may cause some confusion unless this rebounding of the bottom of the trench is taken into account.
2. Continued placement of the embankment material developed photoelastic fringes, qualitatively speaking, with a pattern similar to that of stresses developed in an elastic media composed of homogeneous material stressed by an infinitely long load as defined by Boussinesq.
3. After the loading of the embankment without berms was completed, photoelastic fringes developed in the foreslopes of each trench. These fringes were in circular patterns beginning at the bottom of each side of the trench and extending to the surface of the foundation material. These fringes ended either at the toe of the overlying embankment or in the immediate vicinity of the overlying embankment. These stressed surfaces can develop into the local slip-circle-type failure at the toe of the embankment. This type of failure will cause rotation of a part of both the embankment and the foundation material if stressed beyond the strength of that particular section of the material. Thus, the trenched sections filled with noncohesive materials developed stresses that tended to push the foreslopes of the trench in the direction away from the centerline section of the foundation, which also had a stress concentration that could cause secondary failures.
4. Even under excessive loads applied in an effort to cause failure of the foundation, the modeling media (gelatin) did not display any signs of attaining a plastic state of stress. Thus, in all cases tested in this study, it would be improper to compare the results of these tests with theoretical stress distributions based on the theory of plasticity.
5. Negative vertical displacements (mud waves) occurred starting at the toe of each embankment without berms and extending to the rigid boundaries of the model foundation, which were the side walls of the steel tank. Because gelatin is an incompressible material, additional loads extended the mud waves further toward the rigid boundary and produced higher mud waves. The effect of the boundaries in this case was critical. In actual situations, when an embankment is placed in an area where the vertical displacement of the adjacent areas is critical, the boundary effects resulting from the total or partial confinement of the subgrade should be carefully studied.
6. The placing of berms on trenched sections increased the negative vertical displacement (mud waves) by moving the stressed section closer to the rigid boundaries of

the foundation (sides of the modeling tank). However, the placement of berms decreased by 1.8 percent the strain under the center of the embankment of the model material. From a practical standpoint, this improvement is not worthy of any real consideration.

7. Except in one situation, the addition of berms did not contribute to the general stability of the embankment. The exception is that the slip-circle-type stress concentration, which had developed at the foreslopes of the trenches, closed into a loop after the placement of the berms and went deeper into the foundation material. There was no longer any danger of failure at that point. Thus, the use of berms in trenched sections seems justified only when there is a possibility of developing rotational failure at the lateral extremities of the embankment.

8. Embankments, with or without berms, in trenched sections produced larger shear displacements than those produced in untrenched sections with similar material properties.

9. The negative vertical displacement (mud waves) that developed on trenched sections were 2 to 3 times larger than those that developed on untrenched sections.

10. The sequence of loading of the trenched sections did not affect the pattern of the final stress distribution. However, when the loading was performed in such a manner that one part of the total cross section was built up before the rest of the foundation was loaded, local stress concentrations of high intensity were observed during the loading process. These local stress concentrations could develop into local failures. The best results, both from the standpoint of displacement and uniform stress distribution, were obtained by loading the foundation (building up the embankment) in uniform layers throughout the cross section.

11. Because the use of cohesive material in trenched sections is impractical from the standpoint of obtaining compaction, no attempt was made to model a cohesive embankment in a trenched section.

12. The final stress distribution under a trenched section was somewhat similar to the stress distribution under a rigid plug (Fig. 8).

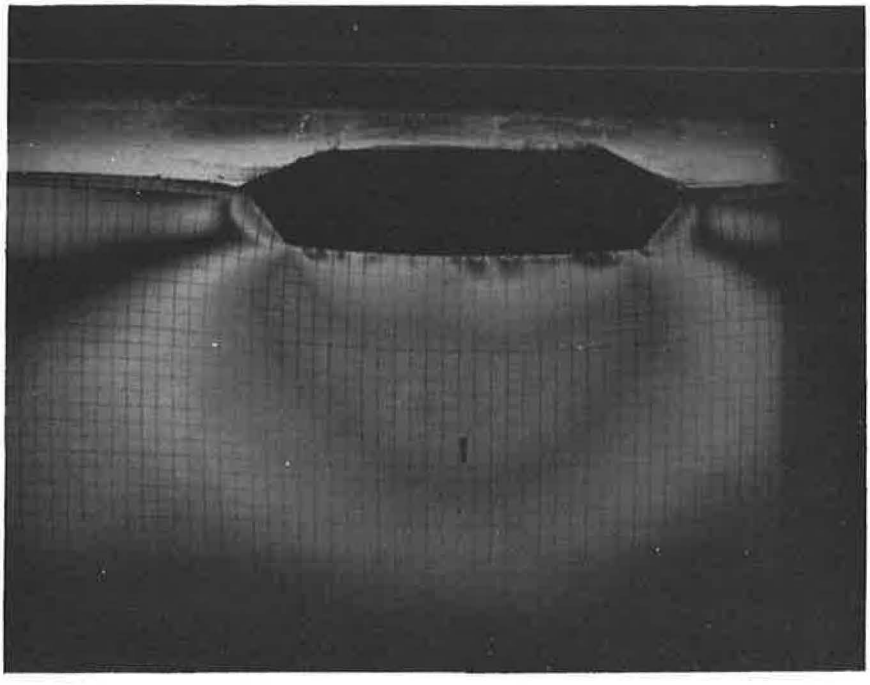

Figure 8. Fringes under trenched section.

Qualitative Analysis of Untrenched Sections

Both cohesive and noncohesive embankments were modeled for untrenched sections. The results of these two types of embankments were similar except as noted in the following. The analysis of untrenched sections after the loading of the embankments of various types (cohesive or noncohesive, with berms or without berms) resulted in the following observations:

1. Untrenched sections produced a stress distribution pattern similar to that of trenched sections except for the lack of circular stress concentrations that had occurred at the foreslopes of trenched sections. Under untrenched sections these stresses were not present.
2. With noncohesive embankments a secondary stress section developed in the foundation adjacent to the toes of the embankment.
3. With cohesive embankments there were no observable secondary stresses in the regions adjacent to the toes of the embankment. Thus, these secondary stress concentrations away from the embankment, which may be critical in cases where other structures exist in these regions, did not form when a cohesive embankment material was used. This indicates that, as a result of the cohesion, the embankment supported itself and did not exert secondary horizontal stresses in a direction away from the centerline of the embankment. Because gelatin was the modeling material for the cohesive embankment, it was possible to observe the stress patterns that developed in the embankment itself. The only stress concentrations that threatened to cause incipient failure were slip-circle-type stress concentrations that developed on the foreslopes of the embankment. Based on these observations, the design of a cohesive embankment on an untrenched section has only two stress criteria to satisfy. These two criteria are (a) that the shear stress should not exceed the shear strength of the material and (b) that slope failures should be prevented.
4. Qualitatively a cohesive embankment on an untrenched section was observed to be the most stable embankment-foundation combination.
5. The addition of berms to embankments on untrenched sections did not contribute to the stability of the embankments. Neither the stress distribution nor the strains or displacements were altered by the addition of berms.
6. When failure was induced by overloading the embankment, initial failure occurred in the vicinity of the toe of the embankment. Here, starting at the surface, the foundation material was put into tension as a result of the excessive displacement that took place under the embankment. This caused tension cracks to open in the regions at the toe of the embankment. After this the material under the embankment started developing fissures and eventually failed. The embankment rotated and in a single mass sank through the fissure that had developed beneath it.
7. Under embankments of approximately the same weight, untrenched sections developed less shear displacement beneath the centerline of the embankment than trenched sections.
8. The mud waves that developed on untrenched sections were considerably less pronounced than those that developed on trenched sections.
9. Untrenched sections did not present any disadvantages when compared to trenched sections. In fact, in only two situations is trenching recommended. Trenching is advisable when the trenches will create a temporary waterway for the transportation of the embankment material. In areas where soft deposits are located, this might be the only way to transport the embankment material. Second, trenching is recommended when the majority of the soft deposits can be removed by the trenching operations. Otherwise, untrenched sections have the advantage of adding a load to the present overburden that, as a result of consolidation, will accelerate the settlement of the embankment and increase the shearing strength of the foundation material.

CONCLUSIONS

Based on the results of this study, the following conclusions were reached by the researchers:

1. The finite element analysis is a very promising tool for the analysis of distribution of stresses and strains beneath embankments with large shear displacements.
2. Along the centerline beneath embankments undergoing large displacements maximum shear stress is apparently smaller than that calculated by approaches assuming small deformation.
3. Maximum normal stress beneath embankments is apparently no greater than that obtained by approaches assuming small deformation theory.
4. The designer is conservative in using the classical approach (Boussinesq) in predicting both maximum shear stress and maximum vertical normal stress along the centerline and beneath an embankment undergoing large deformations.
5. The use of models for photoelastic analysis, as described in this report, is an effective tool for the qualitative analysis of the overall stress and strain patterns in soils supporting embankments and other adjacent structures.
6. The embedded grid method developed for gelatin models in this study is an effective tool for evaluating large strains and displacements.
7. Where trenching is used, negative (upward) as well as positive (downward) displacements should be taken into account in estimating the area of the net cross section of an embankment.
8. Trenching is not recommended for the placement of embankments on soft foundations unless (a) the trench is to be used as an economical waterway to transport bulk embankment material and equipment for the construction, or (b) the trenching operation will remove soft material and expose stiffer layers with higher bearing capacity.
9. Placement of berms produced no desirable effects in an elastic material except for reducing the stress concentration at the toe of trenched embankments. In a plastic material, however, stability may be enhanced through the use of berms.
10. Untrenched embankment configurations produced no stress concentration beneath the embankment.

ACKNOWLEDGMENT

The authors would like to extend their thanks to all students, technicians, and clerical and editorial helpers who worked on this study. Special thanks and acknowledgments are due to James O. DeViller, former graduate research assistant, and John Horn, former laboratory assistant, for their work on the experimental phase of this study; to Hector Rosenfeld, former graduate research assistant, and Ronald S. Reagan for their work on the numerical phase of this study; and to Charles Hill and Ann Lewis for their assistance in the photographic and editorial work.

REFERENCES

1. Finn, W. D. Stress in Soil Masses Under Various Boundary Conditions. Univ. of Michigan, Ann Arbor, unpublished PhD thesis, 1962, p. 10.
2. Taylor, D. Fundamentals of Soil Mechanics. Wiley and Sons, New York, 1960.
3. Turnbull, W. J., Maxwell, A., and Ahlvin, R. G. Stress and Deflections in Homogeneous Soil Masses. Proc. Fifth Internat. Conf. Soil Mechanics, Pt. 2, Paris, 1961, pp. 337-346.
4. Carothers, S. D. Direct Determination of Stresses. Proc. Royal Society of London, Series A, Vol. 97, 1920, pp. 110-123.
5. Huang, Wen-xi, and Zhang, Wen-Zhang. Settlement Analysis of Soil Foundations, of Hydraulic Structure and Stress Distribution in Foundations. Scientia Sinica, Vol. 8, 1959, pp. 1393-1417.
6. Barden, Laing. Stress and Displacements in Cross-Anisotropic Soil. Geotechnique, Vol. 13, 1963, pp. 198-210.
7. Jurgenson, Leo. On the Stability of Foundations of Embankments. Internat. Conf. Soil Mechanics and Foundation Engineering, 1936, pp. 194-200.
8. Gilboy, Glenn. Stability of Embankment Foundations. Trans. Second Conf. Large Dams, Vol. 4, 1936.
9. Perloff, W. H., Baladi, G. Y., and Harr, M. E. Stress Distributions Within and Under Long Elastic Embankments. Highway Research Record 181, 1967, pp. 12-41.

10. Farquharson, F. G., and Hennes, R. G. Gelatin Models for Photoelastic Analysis of Stress in Earth Masses. Civil Engineering, Vol. 10, Pt. 4, 1940, pp. 211-214
11. Richards, R., Jr., and Mark, B. Gelatin Models for Photoelastic Analysis of Gravity Structures. Experimental Mechanics, Jan. 1966, pp. 30-38.
12. Zienkiewicz, O. C., and Cheung, Y. K. The Finite Element Method in Structural and Continuum Mechanics. McGraw-Hill, New York, 1967.
13. Przemieniecki, J. S. Theory of Matrix Structural Analysis. McGraw-Hill, New York, 1968.
14. Clough, R. H. The Finite Element in Plane Stress Analysis. Proc. Second ASCE Conf. on Electronic Computation, Philadelphia, Sept. 1960.
15. Girijavallabham, C. V., and Reese, L. C. Finite Element Method for Problems in Soil Mechanics. Jour. Soil Mech. and Found. Div., ASCE, Vol. 94, No. SM2, March 1968.
16. Argyris, J. H. Matrix Displacement Analysis of Three-Dimensional Elastic Media, Small and Large Displacements. AIAA Jour., Vol. 3, No. 1, Jan. 1965.
17. Durelli, A. J., Phillips, E. A., and Tsao, C. H. Introduction to the Theoretical and Experimental Analysis of Stress and Strains. McGraw-Hill, New York, 1965
18. Frocht, M. M. Photoelasticity, 2 volumes. Wiley and Sons, New York, 1941 and 1948.
19. Dally, J. W., and Riley, W. F. Experimental Stress Analysis. McGraw-Hill, New York, 1965.
20. Arman, A. A New Concept in Design and Construction of Embankments Founded on Muck. Div. of Engineering Research, Louisiana State Univ., 1965.
21. Parks, V. J., and Durelli, A. J. On the Definitions of Strain and Their Use in Large Strain Analysis. Experimental Mechanics, Vol. 7, No. 6, June 1967.

Appendix

NOTATION

The following symbols are used in this paper:

- L = length of embankment;
- u = displacement;
- W = specific weight of backfill material;
- E = modulus of elasticity;
- τ = shearing stress;
- μ = Poisson's ratio;
- $K_{()}$ = ratio of model property to prototype property (property in parentheses);
- c = width of embankment crown;
- $()_p$ = property in parentheses is characteristic of prototype;
- $()_m$ = property in parentheses is characteristic of model;
- f_σ = model fringe value;
- x, y, z = rectangular coordinates;
- σ = normal or principal stress;
- ρ = specific weight of the gelatin;
- ϵ = strain;
- G = shear modulus;
- h = thickness;
- n = fringe order;
- l_i = initial length of line segment;
- l_f = final length of deformed line segment;
- P = grid point in gelatin; and
- γ = shearing strain.

Statistical Approximation for Consolidation Settlement

HAMEED A. ELNAGGAR, University of Pittsburgh; and
RAYMOND J. KRIZEK, The Technological Institute, Northwestern University

Statistical procedures are used to describe consolidation data from various types of compressible, fine-grained soils, and an approximate method is developed to estimate consolidation settlements. The suggested technique is presented in graphical form and is illustrated by several example problems.

•WHEN A LOAD is applied to a compressible foundation soil, the magnitude of the resulting settlement depends on both the compressibility of the foundation soil and the magnitude and distribution of the imposed load. The degree of accuracy required in determining such settlements is governed by the nature of the structure and its sensitivity to total and differential settlements. For example, a rigid frame structure will generally not tolerate large differential settlements between adjacent columns, whereas a large-diameter oil tank with a steel bottom may tolerate differential settlements of several inches between the center and the edge. In the case of a highway embankment crossing areas underlain by soft soils, differential settlements may cause dips in the finished road surface, and total settlements may necessitate fill volumes in excess of the original plans. Also, differential settlements in the cross section of a highway embankment may cause serious longitudinal stresses or unacceptable joint separations in a buried culvert, as well as a decrease in its drainage capacity. For this reason, it is usually desirable to install such structures with a camber to compensate for the expected settlements. This work is directed toward the development of an approximate technique whereby consolidation settlements may be estimated for situations that do not require or warrant a more detailed and accurate soils engineering analysis.

SOIL COMPRESSIBILITY AND CONSOLIDATION

The application of a load to a soil will, in general, cause instantaneous and time-dependent deformations to occur. These deformations may consist of two parts, one part resulting primarily from normal stresses and consisting of volume changes and the other part resulting from shear stresses under conditions of constant volume. Depending on the physical properties of the soil, the magnitudes and rates of these deformations may vary considerably. Although all types of deformation may be important in particular situations, the following analysis will be limited to the time-dependent deformations resulting from volume changes or consolidation of the soil.

For a layer of normally consolidated clay of thickness D, natural void ratio e_o, compression index C_c, and natural overburden pressure p_o, the settlement S under an applied load Δp may be expressed as

$$\frac{S}{D} = \frac{C_c}{1 + e_o} \log \frac{p_o + \Delta p}{p_o} = FL \qquad (1)$$

Paper sponsored by Committee on Construction Practices—Earthwork.

where

$$F = \frac{C_c}{1 + e_0} \tag{2}$$

and

$$L = \log \frac{p_0 + \Delta p}{p_0} \tag{3}$$

The loading factor L in Eq. 3 includes the loading effects, and its exact values depend on the actual configuration of the applied load. The compressibility factor F expresses the compressibility of the soil.

METHOD OF ESTIMATING SETTLEMENT

Determination of Soil Compressibility

Because of the difficulties, expense, and time delay that normally accompany field sampling and laboratory consolidation tests, it is highly desirable to devise some approximate scheme for determining the soil parameters required to compute consolidation settlements for different types of soils. Rutledge (5) found some correlation between C_c and the natural water content w_n of various soils, and this was later confirmed by Peck and Reed (4) and Osterberg (2). Rutledge also found a correlation between C_c and the natural void ratio e_0 of the different soils tested. Approximately 300 data points

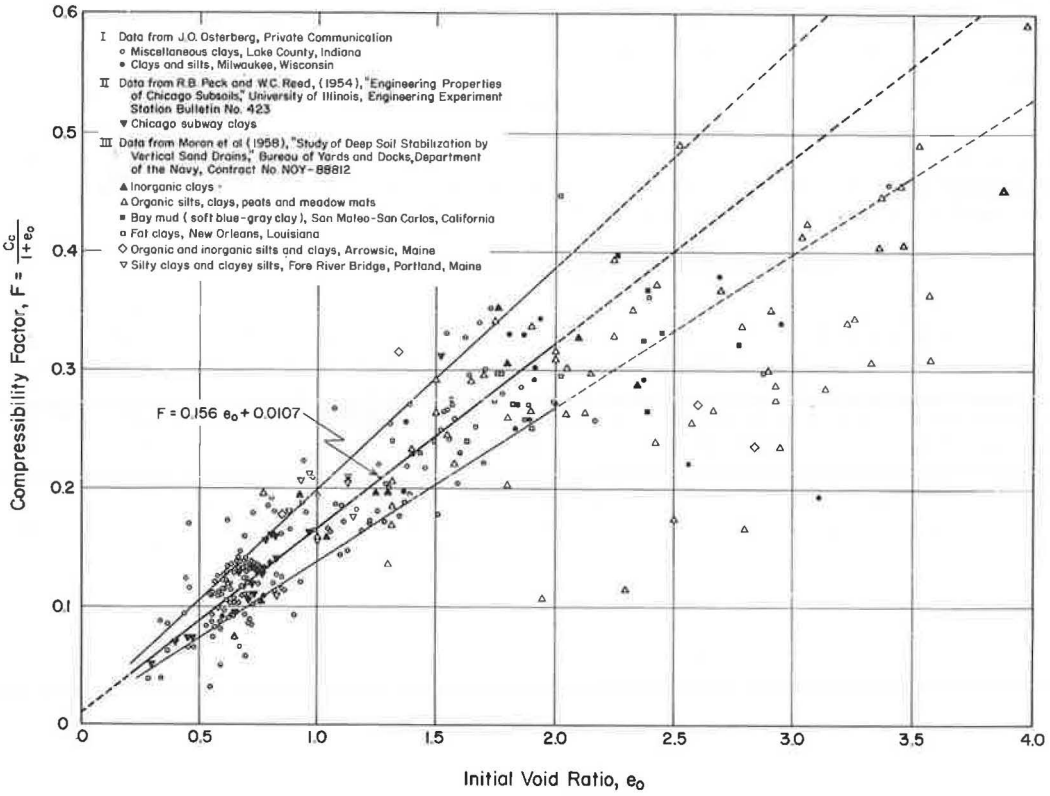

Figure 1. Compressibility factor versus initial void ratio.

representing inorganic and organic clays and silty soils were collected from the literature, and a plot of F versus the initial void ratio e_o is shown in Figure 1. For values of e_o less than approximately 2, there appears to be a reasonable correlation between F and e_o. For e_o greater than 2, parameters other than e_o obviously influence F to such an extent that any correlation between F and e_o is indistinguishable. As a result, the following development is restricted to soils with an initial void ratio less than 2. Soils with e_o greater than approximately 2 are highly compressible and are generally organic in nature, and a considerably greater problem exists.

Approximately 230 of the data points in Figure 1 have an initial void ratio e_o less than 2, and the method of least squares was used to determine the "best fit" straight line describing these data. With F as the dependent variable and e_o as the independent variable, the regression line is given by

$$F_{est} = 0.156\, e_o + 0.0107 \tag{4}$$

To test the "goodness of fit" of Eq. 4, the correlation coefficient r was computed by the equation

$$r = \sqrt{\frac{\sum \left(F_{est} - \overline{F}\right)^2}{\sum (F - \overline{F})}} \tag{5}$$

where F_{est} represents the value of F as estimated from Eq. 4 for a given value of e_o, $\overline{F}$ is the mean value of F for N data points, and F is the observed value. The dimensionless correlation coefficient r measures the goodness of fit achieved by Eq. 4 and it equals unity for perfect correlation. Because the computed value of r is 0.93, a very high linear correlation is implied. The standard error of estimate of F on e_o is given by

$$S_{F \cdot e_o} = \sqrt{\frac{\sum_{i=1}^{N} \left[F^i - F^i_{est} \right]^2}{N}} \tag{6}$$

For the data points considered, $S_{F.\, e_o}$ was found to be 0.028, and the standard error of estimate for various subsets of N varied from 0.022 to 0.032. The standard deviation of F is equal to 0.0755, giving a variance of F of 0.0057, or $(0.0755)^2$.

To estimate the average percent error to be expected when using Eq. 4, the following approach is utilized. Consider a straight line passing through the point $F_{est} = 0$ and making an angle of $\pm\theta$ with the regression line. The percent error in using the regression line will be the same for all data points lying on this line. More generally, the data points lying in the angular sectors $\Delta\theta$ between two pairs of straight lines radiating from the point $F_{est} = 0$ at $\pm(\theta - \frac{1}{2}\Delta\theta)$ and $\pm(\theta + \frac{1}{2}\Delta\theta)$ to the regression line will have approximately the same percent deviation from the regression line. For any given angle θ, the number n of data points in the particular angular sector $\Delta\theta$ under consideration was counted and normalized with respect to the total number N of data points to give a parameter f equal to n/N. Values of f were plotted versus θ in Figure 2, and from these data a probability density function can be defined; that is, the curve that, for a large sample of size N, approximates the frequency curve. A normal distribution curve was found to describe these data very closely, as verified by a goodness-of-fit test. Approximately 69 percent of the data points lie between ±5 deg of the regression line, and 94 percent lie between ±10 deg. As seen in the inset to Figure 2, this means that there is a 69 percent chance that the computed value for F will be within 20 percent of the actual value, and a 94 percent chance that the computed value will be within 44 percent of the actual value.

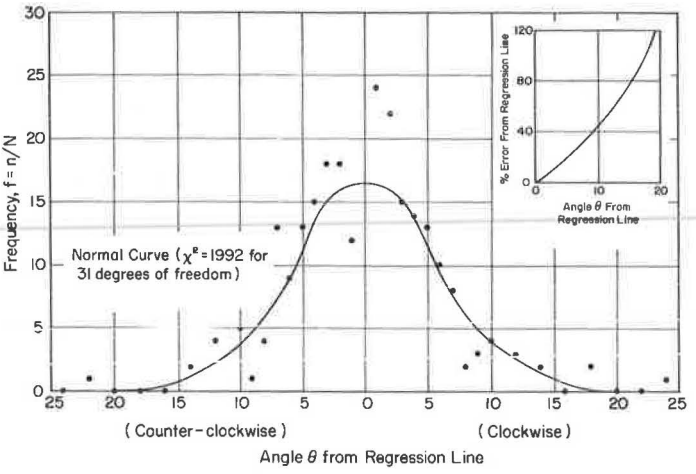

Figure 2. Statistical distribution of compressibility factors.

The preceding correlation between F and e_o indicates that soils with the same in-situ void ratio would consolidate approximately the same magnitude. Such a correlation, however, should not be used indiscriminately; rather, it must be applied in conjunction with sound engineering judgment in order to benefit from its full potential. In particular, it should be emphasized that the foregoing concept is only valid statistically, and its results when applied to an individual situation may be misleading. For example, as can be seen in Figure 1, the compressibility factor may vary from the regression line by a factor of 2 or ½ for particular cases. In order to provide some suggested alternatives in applying the principles outlined, two additional lines at ±5 deg from the regression line are shown in Figure 1. These lines may be regarded as upper and lower median estimates, F_{um} and F_{lm} respectively. Under certain conditions, the use of one or the other of these lines will serve to place lower bounds on the expected error. Which of these lines best represents the characteristics of a given soil is left to engineering judgment. In the absence of any positive reason for using the F_{um} or the F_{lm} line, use of the F_m line is recommended. Extreme caution is advised against the over-enthusiastic or indiscriminate use of this approach for determining expected settlements. The procedure is a very approximate one and intended for use only in situations where it is not necessary to determine precisely the magnitude of anticipated consolidation settlements. For structures that are sensitive to slight settlements, a different approach should be used, and consolidation tests should be performed on good undisturbed samples to evaluate the consolidation characteristics of the soils underlying the specific structure.

The procedure suggested herein involves the determination of the natural void ratio of the soil. One convenient way of obtaining e_o is by use of the expression

$$e_o = G_s \frac{\gamma_w}{\gamma_d} - 1 \qquad (7)$$

where γ_d is the dry density, γ_w is the density of water, and G_s is the specific gravity of the soil particles. Figure 3 shows curves for γ_d versus e_o for different values of G_s as well as the same series of lines shown in Figure 1 and discussed previously. The use of the chart in Figure 3 is demonstrated by the following example.

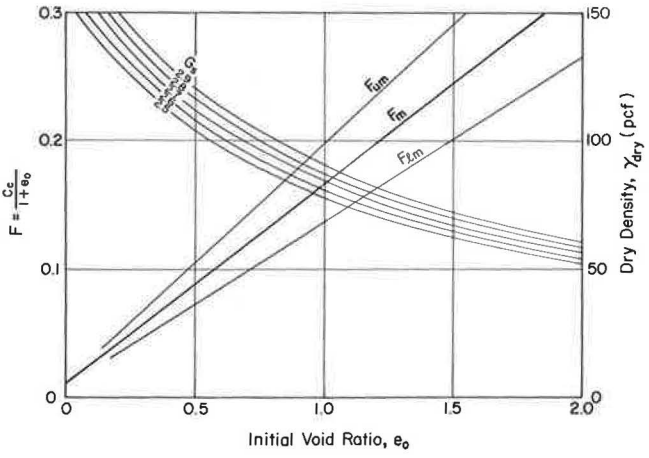

Figure 3. Nomograph for compressibility factor.

Example 1

Given: γ_d = 90 pcf; G_s = 2.63

Determine:

(a) Under normal conditions, what is the mean value of the compressibility factor?
(b) If visual inspection of the soil samples indicates some organic matter, which is evident by the dark color and the odor of the soil, what is the probable value for the compressibility factor?
(c) What is the percentage difference in F if the mean value, case (a), is used for the relatively more compressible soil, case (b)?

Solution: Referring to Figure 3, and using the given values for γ_d and G_s, we obtain e_o = 0.82.

(a) for e_o = 0.82, F_m = 0.138.
(b) The soil in this case will probably be more compressible than average because of its content of organic matter; therefore, for e = 0.82, F_{um} = 0.165.
(c) The percent difference in F is

$$\frac{0.165 - 0.138}{0.165} \times 100 = \frac{0.027}{0.165} \times 100$$

$$= 16.4 \text{ percent}$$

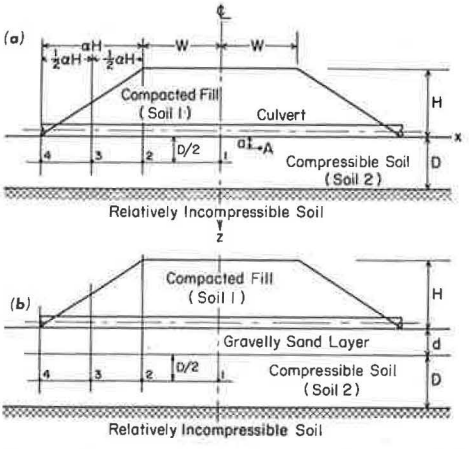

Figure 4. Typical cross sections of compacted embankment and underlying soils.

Determination of Settlement

In order to develop this technique in a reasonably general manner, a trapezoidal load distribution (such as encountered in a highway embankment) will be assumed. Uniformly distributed loads may then be treated as special cases. Figure 4a shows the cross section of a compacted fill embankment (soil 1)

of top width 2W, height H, and side slopes α to 1, underlain by a compressible normally consolidated soil layer (soil 2) of depth D resting on a relatively incompressible foundation soil. This general cross section is, for example, typical of situations in which culvert camber should be determined. If we assume that the groundwater surface is approximately the same as the surface of the compressible layer, the submerged unit weight γ_2' of the soil in the latter layer is $\gamma_2 - \gamma_W$, where γ_2 is the total unit weight of the compressible soil and γ_W is the unit weight of water. In addition, the total unit weight of the compacted fill may be designated as γ_1.

An approximation of the stress distribution in the compressible soil under and adjacent to the embankment may be obtained from Figure 5, which was originally presented by Osterberg (3). With a knowledge of this stress distribution and the compressibility characteristics of the compressible soil, the settlement at any point A may be calculated from the relationship

$$S_A = \frac{C_c}{1 + e_0} \int_a^D \log \frac{p_0(z) + \Delta p(z)}{p_0(z)}\, dz \qquad (8)$$

where $p_0(z)$ is the overburden stress distribution under point A and $\Delta p(z)$ is the stress distribution under point A resulting from the embankment load. Although the application of Eq. 8 is rather straightforward and is susceptible to the development of a family of curves, this degree of refinement is probably not justified for the type of problems considered here. Alternatively, if we make the simplifying assumption that the vertical stresses existing at the midpoints of the compressible layer represent the average values of the vertical stresses in a vertical strip, the settlement at the top of the compressible layer may be written as

$$\frac{S}{D} = \frac{C_c}{1 + e_0} \log \frac{p_0(D/2) + \Delta p(D/2)}{p_0(D/2)} \qquad (9)$$

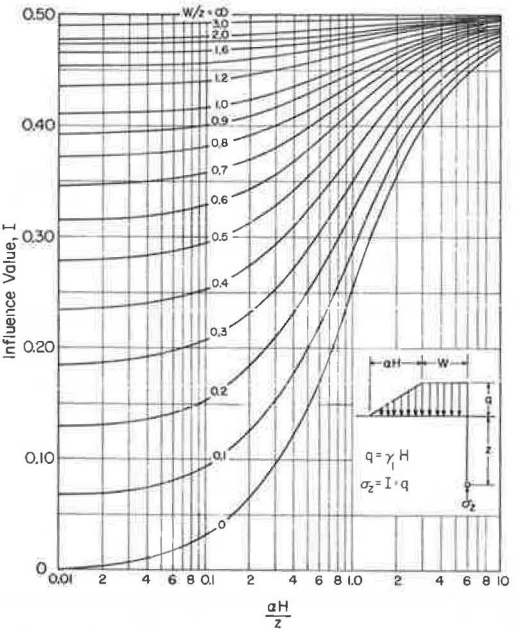

Figure 5. Influence chart for vertical stresses under a trapezoidally distributed strip load.

where the overburden effective stress $p_0(D/2)$ is given by $0.5D\gamma_2$.

To obtain values for the induced vertical stresses $\Delta p(D/2)$ and the associated settlements S, we consider four points 1, 2, 3, and 4, as shown in Figure 4. For point 1, which is under the center of the embankment, the weight of the embankment may be assumed as fully acting; hence, Δp at this point is $\gamma_1 H$. If the further approximations are made that γ_2' equals 60 pcf and γ_1 equals 120 pcf, we have from Eq. 3

$$L = \log \left\{ 1 + 4 \frac{H}{D} \right\} \qquad (10)$$

A plot of L versus H/D is shown in Figure 6. For convenience, the scale of H/D was enlarged, as shown by the curve labeled $(H/D) \times 10^{-1}$, and reduced, as shown by the curve labeled $(H/D) \times 10$. To determine settlement at point 1 in Figure 4, the solution of Eq. 1 is shown in Figure 6, where the settlement ratio S/D

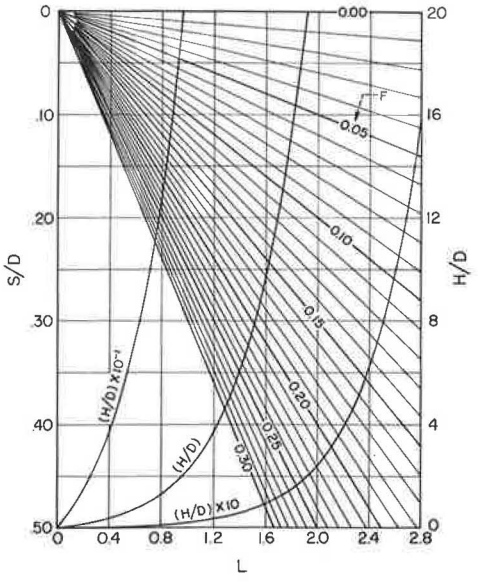

Figure 6. Nomograph for determination of consolidation settlements.

is plotted as a function of L and F for a given H/D ratio. Equation 10 applies to situations where the embankment width W is large relative to the depth of the compressible stratum. In order to use the equation for general cases of imposed loads, divide the load intensity by 120 pcf to obtain an equivalent height H. The use of this chart will be illustrated later. The settlements at points 2, 3, and 4 in Figure 4 may be determined from Figure 6 by multiplying H/D by a factor β. For points 2 and 3, β is on the order of 0.97 and 0.50 respectively. Values for β at point 4 are shown in Figure 7 as a function of the embankment height H and the side slope α.

For a case where the compressible layer of soil is covered by a relatively incompressible soil layer of thickness d, as shown in Figure 4b, the H/D values for any point under the embankment should be further adjusted by multiplying by λ, where

$$\lambda = \frac{D}{D + 2d} \qquad (11)$$

For conditions other than those discussed here, Figure 6 may still be used for settlement determinations provided that H/D is multiplied by the appropriate factor. Suggested approximations are not given in such cases, and engineering judgment will play a large role in this choice. The following examples illustrate the proposed method.

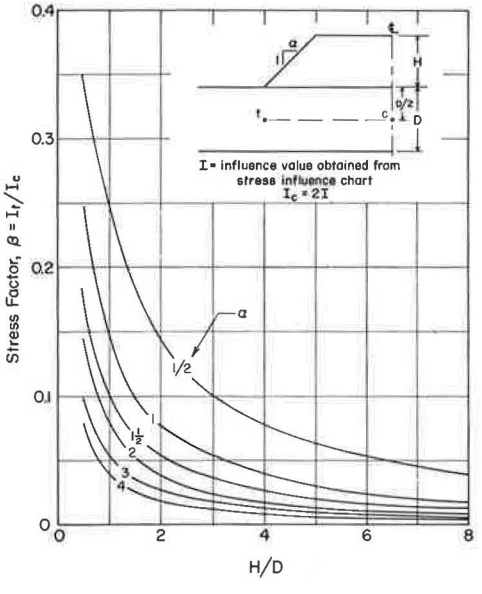

Figure 7. Dependence of stress factor on side slope and height of compacted embankment.

Example 2

Given: The embankment shown in Figure 4 has a height H of 35 ft and a width 2W of 40 ft, with side slopes of 2:1. The foundation soils below the original ground surface are silty clay to a depth of 15 ft underlain by a thick stratum of gravelly sand.

Determine: What is the settlement profile of the original ground surface for the soils described in cases (a) and (b) of Example 1?

Solution: For point 1 in Figure 4, we have

$$\frac{H}{D} = \frac{35}{15} = 2.33$$

which for case (a) yields F = 0.138. Use of Figure 6 gives

$$\frac{S}{D} = 0.140$$

or

$$S = 0.14 \times 15 \times 12$$

$$= 25.2 \text{ in.}$$

For point 2

$$\frac{H}{D} = 0.97 \times 2.33 = 2.26$$

which gives

$$\frac{S}{D} = 0.137$$

or

$$S = 0.137 \times 15 \times 12 = 24.7 \text{ in.}$$

In similar manner, for point 3

$$\frac{H}{D} = 0.5 \times 2.33 = 1.17$$

which gives

$$\frac{S}{D} = 0.104$$

or

$$S = 0.104 \times 15 \times 12 = 18.7 \text{ in.}$$

Finally, at the toe, or at point 4, for $\alpha = 2$ and $H/D = 2.33$, we have from Figure 7 that $\beta = 0.032$; hence, we get

$$\frac{H}{D} = 0.032 \times 2.33 = 0.075$$

which corresponds to

$$\frac{S}{D} = 0.015$$

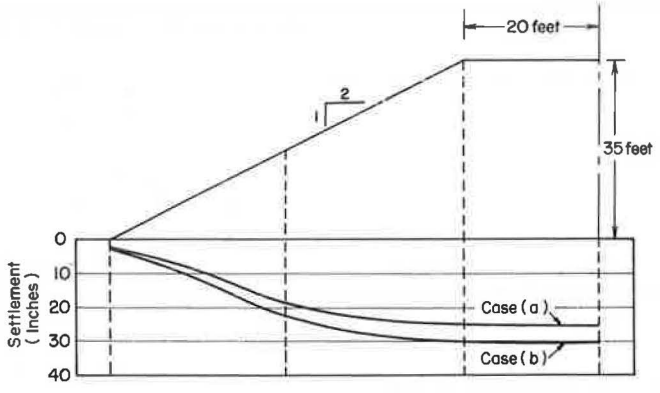

Figure 8. Example of consolidation settlements under a culvert.

or

$$S = 0.015 \times 15 \times 12 = 2.7 \text{ in.}$$

For case (b), F = 0.165, and the settlements at points 1,2, 3, and 4 are, at point 1, S = 0.168 x 15 x 12 = 30.2 in.; at point 2, S = 0.166 x 15 x 12 = 29.9 in.; at point 3, S = 0.123 x 15 x 12 = 22.1 in.; and at point 4, S = 0.018 x 15 x 12 = 3.2 in. The predicted settlement profiles for these cases are shown in Figure 8.

Example 3

What are the predicted settlements at points 1 and 4 for case (a) of Example 2 if the silty clay layer were covered by 5 ft of dense sand? From Eq. 11 we calculate

$$\lambda = \frac{15}{15 + 2 \times 5} = \frac{15}{25} = 0.6$$

At point 1, we have

$$\frac{H}{D} = 2.33 \times 0.6 = 1.40$$

which for F = 0.138 yields

$$\frac{S}{D} = 0.113$$

or

$$S = 0.113 \times 15 \times 12 = 20.3 \text{ in.}$$

At point 4, we have

$$\frac{H}{D} = (0.032 \times 2.33) \times 0.6 = 0.045$$

which gives

$$\frac{S}{D} = 0.010$$

or

$$S = 0.10 \times 15 \times 12 = 1.8 \text{ in.}$$

OVERCONSOLIDATED SOILS

If soils are highly overconsolidated, it is unlikely that settlement problems will arise for the type of situations under consideration. When the weight of embankment and other loads, plus the existing overburden stress, is less than the preconsolidation stress of the soil at a given point, no appreciable settlement may be expected. On the other hand, if the stresses resulting from the proposed loads are higher than the preconsolidation stress, the soil will consolidate essentially under the stress in excess of the preconsolidation stress. Therefore, an evaluation of the preconsolidation stress is essential for reasonably accurate settlement predictions, and laboratory consolidation tests

may be required. Although the method presented herein is not directly applicable to overconsolidated soils, it may be used with modification. If the stress in excess of the preconsolidation stress is denoted by p_c, an equivalent height of compacted fill H_e may be determined from the relationship

$$H_e = \frac{p_c}{\gamma_1} \tag{12}$$

If H_e is equal to or greater than H, the height of the embankment, settlement may be considered negligible. On the other hand, if H_e is equal to nH, where n is less than unity, the method presented herein may be used with engineering judgment to predict settlements if H/D is reduced by a factor of (1 - n). Such a procedure is particularly advantageous if p_c is known without the necessity of conducting laboratory tests.

SUMMARY AND CONCLUSIONS

Statistical procedures are used in conjunction with reported consolidation test data on various types of compressible, fine-grained soils to develop a simple graphical procedure whereby approximate consolidation settlements might be quickly and inexpensively estimated. The technique developed is illustrated for several typical example problems. It must be emphasized that this method yields only approximate settlements in the statistical sense, and it must be used in conjunction with good engineering judgment. For cases where a more accurate settlement determination is required, a comprehensive soils investigation is necessary.

REFERENCES

1. Moran, Proctor, Mueser, Rutledge, Consulting Engineers. Study of Deep Soil Stabilization by Vertical Sand Drains. Bureau of Yards and Docks, Dept. of the Navy, Contract No. NOY-88812, 1958.
2. Osterberg, J. O. Private communication, 1968.
3. Osterberg, J. O. Influence Values for Vertical Stresses in a Semi-Infinite Mass Due to an Embankment Loading. Proc. Fourth Internat. Conf. on Soil Mech. and Found. Eng., Vol. 1, 1957, pp. 393-394.
4. Peck, R. B., and Reed, W. C. Engineering Properties of Chicago Subsoils. Engineering Experimental Station, Univ. of Illinois, Bull. 423, 1954.
5. Rutledge, P. C. Compression Characteristics of Clays and Application to Settlement Analysis. Harvard Univ., doctoral dissertation, 1939.